

THE UNIVERSITY OF ASTON IN BIRMINGHAM

IN SITU ION ETCHING IN A SCANNING  
ELECTRON MICROSCOPE

Thesis submitted for the degree of

DOCTOR OF PHILOSOPHY

by

Resham Singh Dhariwal (B.Sc., M.Sc.)

THESIS  
621.385833 DHA

198142 11 NOV 1976

Department of Physics

June 1976

### ACKNOWLEDGMENTS

In this study a great deal of collaborative work was undertaken so that it is appropriate that I should acknowledge all those that have helped with the project.

First of all I would like to most sincerely thank my supervisor, Dr. R.K. Fitch, without whose interest, continued encouragement and invaluable help, the work could not have been carried out. Thanks are due to Professor T. Mulvey for his helpful discussions and interest and also to Professor S.E. Hunt for providing the facilities in his department. I express my gratitude to the Physics Workshop staff under the direction of Mr. F. Lane for constructing much of the apparatus. I am grateful to Steve Southwick and Dr. Atkins of the Biology Department of Aston University for preparing the soft biological specimens and also helping in the interpretation of the micrographs.

I am very grateful to academic and technical staff at the Oral Pathology Department of the University of Birmingham for their help with the dental study. Amongst them I would particularly like to mention the names of Professor C.L.B. Lavelle, Mr. G.A. Johnson, Professor E.A. Marsland, Dr. R.M. Browne, Dr. S.L. Rowles, Dr. J. Rippon. Also I am grateful to Mr. T.F. Stack and Mrs. M.J. Greenhill, also of the Oral Pathology Department for printing most of the photographs.

I am grateful to the Lucas Research Group, Solihull for providing some specimens and also for their help in doing the X-ray analysis on their scanning electron microscope. In particular I

would like to mention the names of Mr. Gibbs and Mrs. S. Pantaney for their valuable discussions.

Many thanks to Dr. M.S. Raven of the Woolfson Institute for Interfacial Technology, Nottingham for carrying out the ESCA analysis on the copper specimens. Thanks also to Mr. D. Malin of Ciba Geigy, Manchester for his discussion and correspondence in relation to the work on araldite. I am grateful to Dr. J. Franks of Ion Tech Limited, for donating the spherical source which was used in this investigation.

I am very grateful to the SRC for financial support for one year and last of all, but not the least my most sincere gratitude to my family for supporting and encouraging me at every stage of the work.

## ABSTRACT

A facility for in-situ ion etching in a scanning electron microscope has been developed and successfully applied to a variety of materials. Two forms of the saddle field ion source, namely the cylindrical and spherical source, have been used and a comparison between these has been made in terms of etching rates, uniformity of etching, contamination and rise in temperature of the specimen during ion bombardment.

Artefacts produced during etching, including structures not previously reported in the literature, have been studied and in particular cone formation has been followed during its growth. It has been shown that some of these artefacts can be avoided by rotation of the specimen but this often results in a loss of the desired structural features.

The ion etching technique has been shown to give valuable structural information on various metals, alloys and sinters and is in general superior to chemical etching. Insulating materials such as plastics, ceramics, glass and resins have been successfully etched but in some cases artefacts are produced due to thermal degradation. Furthermore, some of these materials do not provide much useful information as there is only a small variation in the sputtering yield of the constituent elements.

In contrast to a number of other workers, it is concluded that ion etching of soft biological tissues, such as the rat duodenum, can be of considerable value. This arises from the selective intake of the heavy fixation elements by different parts of the tissue,

thus producing a large variation in the sputtering yield.

A detailed study of hard biological materials, such as dental tissues and restorative materials, has also been shown to yield valuable structural information. A study of specific problems, such as the reprecipitation of calcium phosphate during demineralisation of teeth and the decay of amalgam restorations has proved the value of the technique in areas where structural information is not of major interest.

## CONTENTS

	<u>Page</u>
<u>CHAPTER 1</u> <u>ION BOMBARDMENT OF SOLIDS</u>	1
1.1 Introduction	1
1.2 Theory of Ion Bombardment	2
1.3 Secondary Effects of Ion Bombardment	7
1.3.1 Inelastic Effects	7
1.3.2 Elastic Effects	13
1.4 Applications of Ion Bombardment	15
1.4.1 Secondary Electron Multiplier Detectors	15
1.4.2 Ion Induced X-ray Analysis	16
1.4.3 Surface Cleaning	16
1.4.4 Secondary Ion Mass Spectrometry	16
1.4.5 Ion Implantation	17
1.4.6 Ion Etching	17
 <u>CHAPTER 2</u> <u>SPUTTERING</u>	 18
2.1 Theory of Sputtering	22
2.2 Applications of Sputtering	24
2.2.1 The Production of Thin Films	25
2.2.2 Machining and Thinning of Specimens	25
2.2.3 Sputter Ion Etching	26

	<u>Page</u>
<u>CHAPTER 3</u> <u>ION SOURCES</u>	30
3.1 Requirements of an Ion Source for Etching	30
3.1.1 Radio Frequency Sources	31
3.1.2 Hot Cathode Sources	31
3.1.3 Cold Cathode Sources	32
3.2 The Electrostatic Charged Particle Oscillator	32
3.3 Saddle Field Ion Source of Cylindrical Geometry	36
3.3.1 Water Cooled Source	38
3.3.2 Distortion Effects of the Ion Exit Aperture	42
3.4 Saddle Field Ion Source of Spherical Geometry	50
3.5 Applications of the Saddle Field Ion Sources	51
 <u>CHAPTER 4</u> <u>EXPERIMENTAL ARRANGEMENTS FOR IN SITU ION                   ETCHING IN THE SCANNING ELECTRON MICROSCOPE</u>	 53
4.1 The Cylindrical Ion Source	53
4.2 The Spherical Ion Source	55
4.3 Electrical Circuit	56
4.4 The Scanning Electron Microscope	57
4.5 Mounting of the Ion Sources in the Miniscan	59
4.6 Preparation of Samples	59

	<u>Page</u>
4.7 Experimental Procedure for Ion Etching	60
<u>CHAPTER 5</u> <u>OPERATING AND ETCHING CHARACTERISTICS OF THE</u>	
<u>ION SOURCES</u>	61
5.1 Introduction	61
5.2 Operating Characteristics	61
5.2.1 Cylindrical Source	61
5.2.2 Spherical Source	64
5.3 Etching Rates	67
5.3.1 Bulk Copper Specimens	67
5.3.2 Ion Source Cathode	68
5.3.3 Evaporated Copper Films	68
5.4 Temperature of Materials during Ion Bombardment	72
5.4.1 Introduction	72
5.4.2 Temperature Measurement of Various Materials	74
5.4.3 Discussion	82
5.5 Chemical Analysis of an Ion Bombarded Sample of Copper using Electron Spectroscopy	82
5.6 Discussion	86
<u>CHAPTER 6</u> <u>ARTEFACTUAL STRUCTURES ARISING FROM ION ETCHING</u>	88
6.1 Introduction	88
6.2 Theory of Structure Formation	91
6.3 In-Situ Observation of Cones in the Scanning Electron Microscope	95

	<u>Page</u>
6.3.1 The Growth of a Cone with Bombardment Time	95
6.3.2 Study of Cones on Different Materials	98
6.4 Discussion of Results	99
<u>CHAPTER 7</u> <u>ION ETCHING OF VARIOUS MATERIALS</u>	102
7.1 Introduction	102
7.2 Conducting Materials	103
7.2.1 Annealed-Extended Copper	103
7.2.2 Copper-Iron Sinter	105
7.2.3 Fractured Piston Steel	106
7.3 Insulating Materials	107
7.3.1 Silicon Nitride Ceramic	107
7.3.2 Soda Glass	107
7.3.3 Acrylic Plastic	109
7.3.4 D.M.C. Plastic	109
7.3.5 Acetal Plastic	110
7.3.6 Araldite Epoxy Resin	111
7.4 Soft Biological Material	112
7.5 Hard Biological Material	114
7.5.1 Form of a Restored Tooth	114
7.5.2 Structure of Dental Tissues and Restorative Materials	115
7.5.3 Cavity Margin Amalgam Interface	118
7.5.4 The Reprecipitation of Secondary Calcium Phosphate during Demineralisation	120

	<u>Page</u>
<u>CHAPTER 8</u> <u>CONCLUSIONS AND SUGGESTIONS FOR FURTHER WORK</u>	122
<u>LIST OF FIGURES</u>	128
<u>LIST OF PLATES</u>	131
<u>REFERENCES</u>	133

## CHAPTER 1

### ION BOMBARDMENT OF SOLIDS

#### 1.1 Introduction

The effects produced by ions impinging upon solids have been known for well over a hundred years but even now are not fully understood. Only in the last two decades has the importance and significance of the phenomena been realised.

It was in 1851 that Plucker while working with X-ray tubes noted that the voltage applied across the tube had to be gradually increased and that the X-rays became harder. This was attributed to the ionization of the residual gases after which the energetic ions struck exposed regions of the tube and became trapped. The following year, Grove (1852), observed that in glow discharge tubes, some surfaces were gradually eroded away due to continuous bombardment by positive ions. After these early reports, no significant advancement occurred for about a hundred years, when it was realised that ion bombardment had applications in many branches of science. The gas removal effect noted by Plucker (1851), was quickly put into use in the design of new pumping systems and the surface erosion effect observed by Grove (1852), was exploited in producing clean, highly reactive metal films. It was also realised that 'ultra' clean targets, for use in such techniques as X-ray production and accelerators, could be made by removing the adherent surface contaminants. Further applications of ion bombardment will be discussed later in section 1.4.

The theoretical aspects of ion bombardment have also been slow to develop. However, scientists quickly became aware of the fact that

predictions of the interactions of ions with different materials could only be made, if an understanding of the mechanism of energy loss and collisions with the solid lattice was acquired. The work in this branch of the subject has been rapid since about 1955 and is covered extensively in books by Kaminsky (1965), Thompson (1969) and Carter and Colligon (1968). An excellent review article has been written by Dearnley (1969) and a very recent comprehensive one by McCracken (1975), in which he covers most of the important developments in the field of ion bombardment of solids.

### 1.2 Theory of Ion Bombardment

The collisions between the *crystal* and the incident particles can be considered as isolated two body events. It is now generally accepted that under most conditions the incident ion interacts with only one target atom at a time, the time during which the interaction takes place being small compared with the time to travel between one atom and the next.

The energy  $E$  of the incident ion after scattering through a given angle  $\Theta$  is determined by the laws of conservation of energy and momentum and can be shown to be;

$$E = \frac{4m_1 m_2}{(m_1+m_2)^2} E_0 \sin^2 \left( \frac{\Theta}{2} \right) \dots\dots (1.1)$$

where  $m_1$  and  $m_2$  are the masses of the incident ion and target atom respectively. The maximum energy is transferred when  $\Theta = \pi$  and we have a head-on collision. For this case;

$$E = \frac{4m_1 m_2}{(m_1+m_2)^2} E_0 \dots\dots (1.2)$$

In addition to the total energy transfer for a given collision, it is necessary to investigate the scattering of the incident ion. To do this one must consider the fundamental question of interatomic forces.

Consider two atoms with masses  $m_1$  and  $m_2$ , nuclear charges  $Z_1e$  and  $Z_2e$  respectively, their nuclei separated by a distance  $r$ . The force between them is then described by a potential energy  $V(r)$  which arises from interactions involving the electrons and the nuclei. Even in the simplest case  $V(r)$  has never been determined exactly but some simple considerations show that it must be dominated by two distinct contributions. There are two useful reference points worth mentioning in the scale of separation that we are dealing with. Firstly the Bohr radius of the hydrogen atom,  $a_0 = 0.53 \text{ \AA}$  and secondly the spacing between neighbouring atoms in the crystal lattice denoted by  $D$  (typically  $2.5 \text{ \AA}$ ).

When  $r \gg D$ , the energy levels of the individual atoms being quantized are populated by the electrons according to the Pauli Exclusion Principle. As the atoms are brought together the outer incompletely filled shells will overlap and there will be attractive interactions of the type that form chemical bonds and the relatively weaker Van de Waals forces. Neither of these involve energies of more than a few eV and is not significant to the collision problem.

However, when  $a_0 < r \leq D$  the closed inner shells begin to overlap and some electrons will find themselves in the same region of the space occupying similar energy levels. The Exclusion Principle demands that they change their levels and since all lower levels are occupied, they can only move up. The extra energy is supplied by the work done in forcing the atoms together and hence constitutes a positive potential energy of interaction. This effect is known as

closed shell repulsion and the potential is best described by a function of the form;

$$V(r) = A \exp \left( -\frac{r}{b} \right) \quad \dots (1.3)$$

where A and b are constants, derivable from the elastic moduli of the solid. This is referred to as the Born-Mayer (1932) potential function since it was first used by them to formulate a theory of ionic crystals.

When  $r \ll a_0$  and the nuclei become the closest pair of charged particles in the system, the potential is given by the well known Coulomb function;

$$V(r) = \frac{Z_1 Z_2 e^2}{r \ 4\pi\epsilon\epsilon_0} \quad \dots (1.4)$$

At large distances where there is the possibility of electrons entering the internuclear space, there is a reduction of the Coulomb potential because of the electrostatic screening of the nuclear charges by the space charge of the innermost electron shells. One then has to think in terms of a screened Coulomb potential. It is possible to estimate the screening effect and the potential can be described for  $r < a_0$  by the equation due to Bohr (1948);

$$V(r) = \frac{Z_1 Z_2 e^2}{r \ 4\pi\epsilon\epsilon_0} \exp \left( -\frac{r}{a} \right) \quad \dots (1.5)$$

where  $a = a_0 (Z_1^{\frac{2}{3}} + Z_2^{\frac{2}{3}})^{-\frac{1}{2}}$ ,

Clearly equation (1.5) reduces to the simple Coulomb type when  $r \ll a$ .

In the consideration of equation (1.5), there are two important points to be made about the total repulsive potential. At smaller

and smaller separations the screening term will effectively vanish and the inter-nuclear term will dominate. However for  $r > a_0$ , the screening effect represented by the function  $\exp\left(-\frac{r}{a}\right)$  will dominate over the inter-nuclear term. Thus in a region  $a_0 < r < D$ , electronic interactions are the main contribution to  $V(r)$ .

Another very useful and well known potential function, obtained from the Thomas-Fermi statistical model of the atom is also sometimes used;

$$V(r) = (Z_1 Z_2 e^2) \phi_{TF} \left( \frac{r}{a} \right) / r \quad \dots\dots (1.6)$$

where  $\phi_{TF}$  is the Thomas-Fermi screening function which has been calculated numerically and has been tabulated by Gombas (1956).

There are many variations and combinations of the above equations in order to describe the potential more accurately under different interaction conditions. However, all of these will not be considered, but it is worth mentioning two other potential functions which are frequently used. These are the inverse square and the hard sphere potential function. The inverse square expression is given by Thompson (1969);

$$V(r) = \frac{2E_R}{e} (Z_1 Z_2)^{\frac{5}{2}} \left( \frac{a_0}{r} \right)^2 \quad \dots\dots (1.7)$$

where  $E_R$  is the Rydberg energy (13.6 eV).

In the hard sphere case  $V(r) = 0$  for  $r > R$  and

$$V(r) = \infty \quad \text{for } r < R,$$

where  $R$  is the radius of the sphere. Some measure of reality is introduced by allowing  $R$  to be energy dependent and it is useful to set it equal to the distance of closest approach in a head-on collision. The hard-sphere potential fails to predict accurately the

angular distribution of scattering in atomic collisions, but its simplicity in analytical calculations makes it useful in studying the general features of atomic collisions.

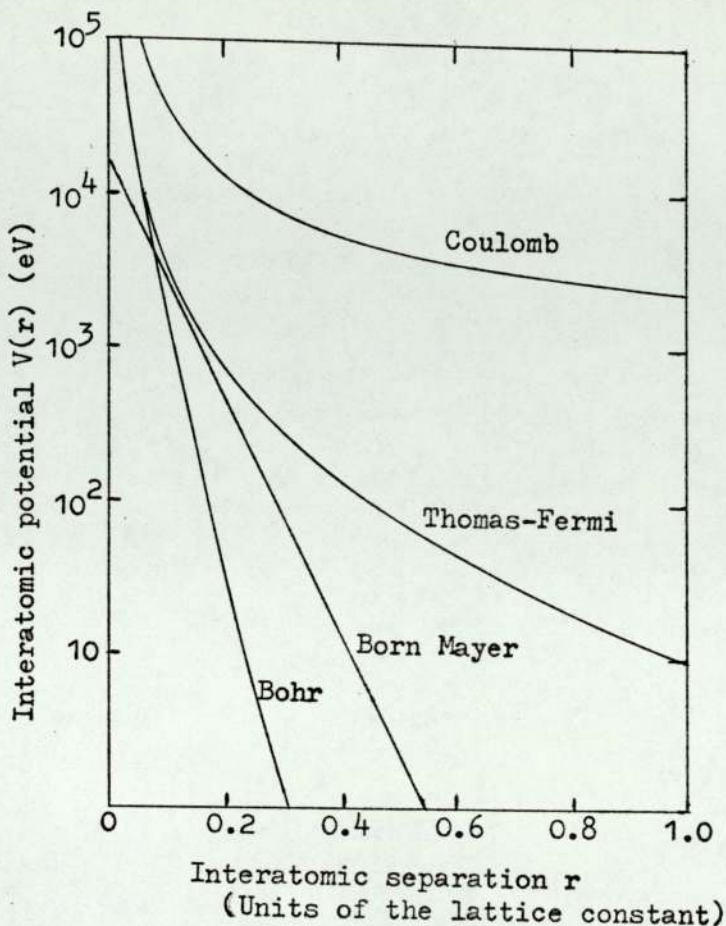


Figure 1 Interatomic potential functions evaluated for a copper crystal. (After Carter and Colligon 1968).

Figure 1 shows the various potential functions tabulated for a copper crystal. The relative weakness of the Bohr function at large r and of the Born-Mayer form at small r can be clearly seen.

Thompson (1969) derives a theoretical expression for the scattering angle  $\theta$  as;

$$\theta = \pi - 2 \int_0^{\frac{1}{r}} \left( \frac{1}{P^2} \left[ 1 - \frac{V(u)}{E_1} \frac{m_1 + m_2}{m_2} \right] - u^2 \right)^{-\frac{1}{2}} du \quad \dots (1.8)$$

where  $u = \frac{1}{r}$ ,  $\rho$  is the upper limit of u and is the minimum value of r,

i.e. the distance of closest approach,  $P$  is the impact parameter, being the vertical distance between the initial direction of the primary and the target atom. Explicit evaluation of the integral in equation (1.8) is only possible for simple potentials such as the Coulomb and Inverse Square. In all other cases numerical methods must be employed.

### 1.3 Secondary effects of Ion Bombardment

When an energetic ion impinges upon the surface of a solid it can give rise to many different types of reactions by either inelastic or elastic collisions. The inelastic collisions result in effects such as secondary electron emission, photon emission, X-ray emission and heating of the target. The elastic collisions on the other hand result in processes such as ion reflection and secondary particle emission, the latter process being known as sputtering. The various effects listed above will now be considered briefly under two subsection headings. References to papers giving more detailed information will also be included.

#### 1.3.1 Inelastic Effects

##### (a) Secondary Electron Emission

While slowing down in the solid lattice, the energy of the incident ion can be used to produce secondary electrons. A coefficient  $\gamma$  is defined as the number of electrons liberated per incident ion. It is an important factor to be considered since the emission of an electron from a collector, is the same as the arrival of a positive ion and can thus lead to spurious results when measuring ion currents.

An ion approaching a target surface has both potential energy due to its elevation to the ionized state, and kinetic energy due to its velocity relative to the target material. There have been many

theories put forward in order to explain how electron emission can occur as a result of the re-arrangement of either potential or kinetic energies in the ion-target system but none of these is completely satisfactory. From the experimental results it appears that, to a first approximation, the yields are independent of kinetic energy for ion energies below about 1 keV and potential ejection predominates. For energies greater than about 1 keV, kinetic energy considerations start to be dominant. An important point to be made is that potential ejection is not energetically possible for all ion-target combinations, whilst kinetic emission is always possible at energies above a minimum threshold value.

### Potential Ejection

This is now quite well understood and the greatest contribution to the theory has been made by Hagstrum (1954). It has been shown to be caused by Auger neutralisation of the incident ion. This is a process where an electron from the Fermi sea of the solid tunnels through the potential barrier to neutralise the ion. The energy that is released in the process is transferred to a second electron which is then ejected. The process is shown diagrammatically in figure 2. The energy of the ejected electron,  $E_k$  is given by

$$E_k = E_i - \alpha - \beta$$

where  $E_i$  is the ionization potential of the incident ion as modified by the target surface and  $\alpha$  and  $\beta$  are the energy levels of the two electrons below the vacuum level. From the above expression it can be deduced that potential emission will not be energetically possible for an ion-target system where the ionization potential of the ion is less than twice the metal work function. This has been verified by experiments such as those of Petrov (1962) who

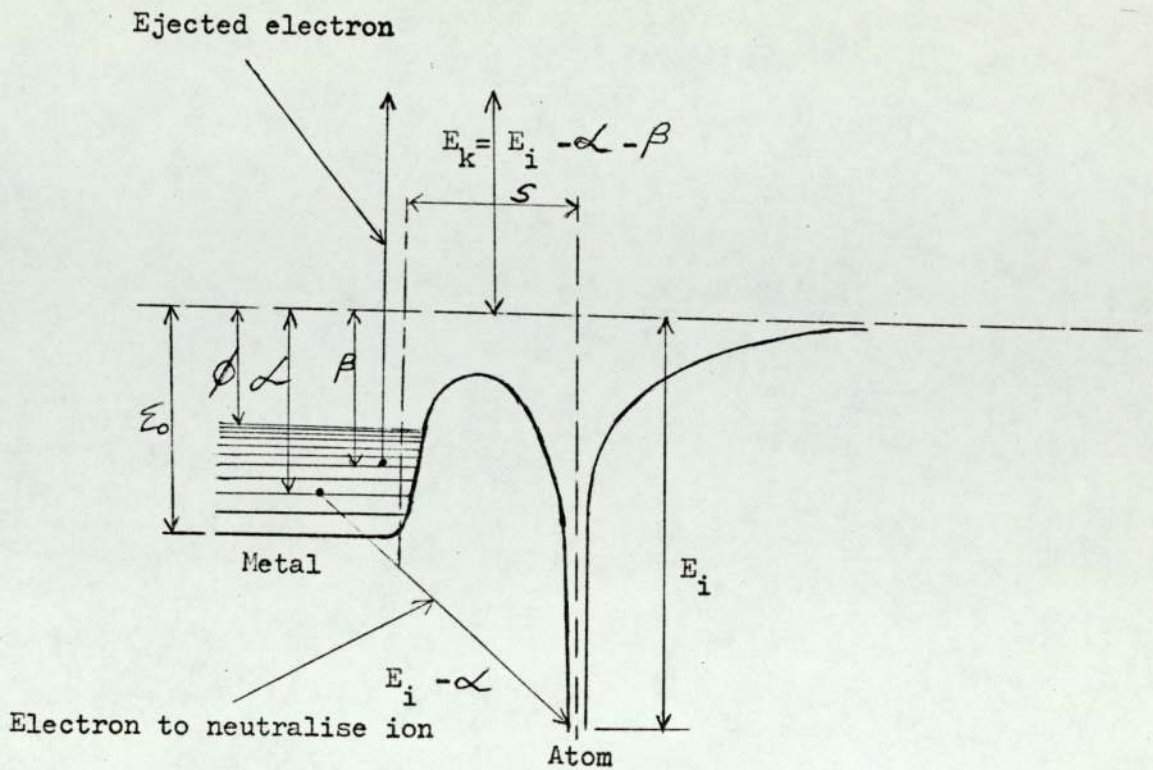


Figure 2. Illustrating the Auger neutralisation of an ion at a metal surface. (After McCracken 1975).

bombarded tungsten with potassium and argon ions. For the case of potassium ions bombarding tungsten, no potential emission was observed, (see figure 3). In the case of bombardment with argon ions, potential emission was observed and was found to be constant up to an ion energy of about 1.5 keV, which is the threshold for the onset of kinetic emission for both argon and potassium.

Subsequently,  $\chi$  was found to increase linearly with ion energy up to the maximum energy investigated, which was 6 keV.

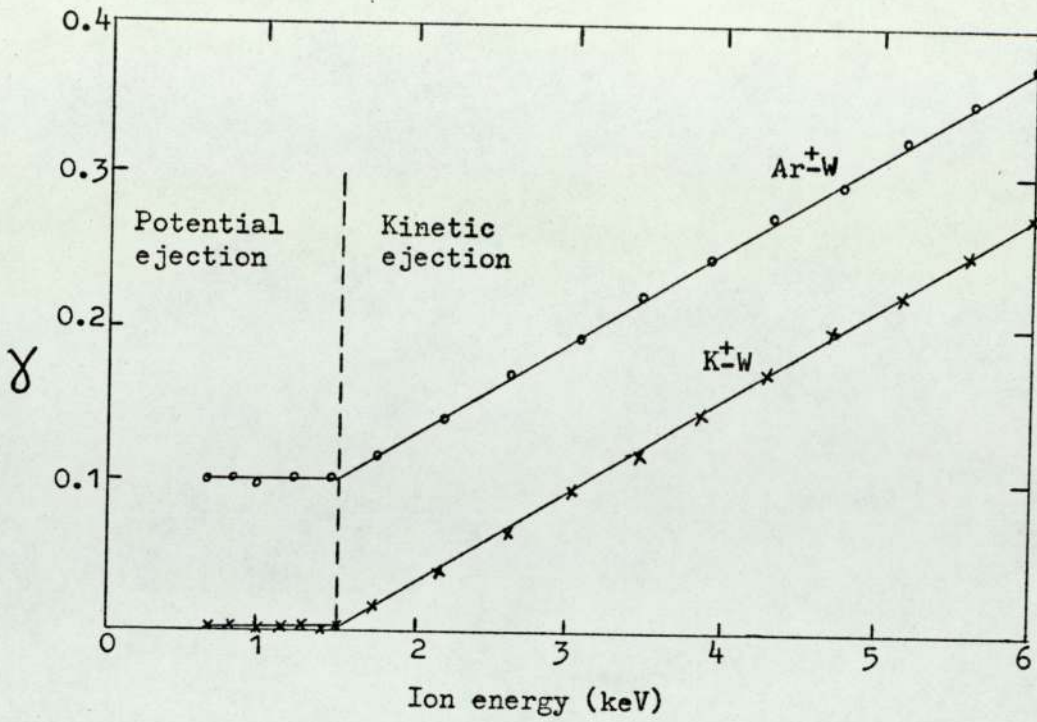


Figure 3. The variation of  $\gamma$  under conditions of kinetic and potential ejection for Ar and K ions on tungsten. (After Petrov 1962).

Kinetic Emission

Kinetic emission is not as well understood as potential emission and the theory of Parilis and Kishinevskii (1960) is the one that explains most of the observed results. This is based on an internal Auger process in which the incident particle excites a lattice atom electron from the valence to the conduction band. The re-combination energy of this electron hole pair causes the ejection of a second electron from the conduction band. The least amount of energy required is the energy interval from the vacuum level to the bottom of the conduction band, plus the energy of the forbidden gap.

Parilis et al derive a theoretical expression for the secondary electron emission coefficient given by

$$\gamma = N \sigma(U_0) \lambda W(\mathcal{E}) \dots (1.9)$$

where  $W(\mathcal{E})$  is the probability for the Auger process and is given by;

$$W(\delta) = 0.016 (\delta - 2\phi)$$

here  $\delta$  is the recombination energy of the electron-hole pair and  $\phi$  is the work function of the surface.  $\sigma(U_0)$  is the effective cross section for ionization of the ionic core. It is a function of  $U_0$ , the initial velocity of the ion and the atomic numbers of the ion and target atom. The term cross section in this context refers to the probability of formation of an electron-hole pair.  $\lambda$  is the mean free path of the electron produced and  $N$  is the atom density in the crystal.

The ion velocity is seen to be the most important parameter in determining kinetic emission and according to the theory of Parilis et al (1960), no kinetic emission can occur up to a certain threshold energy. Above this threshold the yield then proceeds to increase in a linear form with energy and then at higher energies the yield increases at a lesser rate and becomes a linear function of the ion velocity. In order to derive equation (1.9) Parilis et al found that the limitation

$$\frac{1}{4} < \frac{Z_1}{Z_2} < 4$$

must be imposed, where  $Z_1$  is the atomic number of the incident ion and  $Z_2$  is the atomic number of the target atom. It was then found that the threshold velocity for bombarding ions must be between  $0.6$  to  $0.7 \times 10^5$  m.sec<sup>-1</sup>, depending upon the ion-target combination. The results obtained by many different workers on threshold energy for kinetic emission agree quite well with the predictions of the theory. However, there is no single theory which gives a full understanding of kinetic emission for all the different ion-atom combinations which can be set up. The electron emission coefficient ( $\gamma$ ), is generally less than unity below an ion energy of about

10 keV and approaches unity at this energy. The energy of the emitted electrons is also usually less than about 10 eV and only a small proportion, depending upon the ion bombardment energy, have energy as much as 50 eV.

(b) Photon Emission

It has also been observed that surfaces under ion bombardment emit photons in the visible and ultra violet region. This process is perhaps not unexpected since it represents the group of secondaries which have either not quite reached, or reach only temporarily their ionized state during the exchanges leading to emission. Spectral analysis of the light shows it to be made up not only of sharp lines characteristic of atomic transitions in the target species, but also those of the incident species. Recently the field has been reviewed in detail in a book by Parilis (1968).

(c) X-ray Emission

X-ray emission is a result of the same initial process as described for Auger electron emission, namely the production of an inner electron shell vacancy as a result of a collision by the incident ion with a target atom. The emission of an Auger electron subsequent to K shell vacancy production is more probable for all target Z values less than about 30, and several orders of magnitude more probable for  $Z \leq 15$ , (Walters and Bhalla, 1971). For higher shells the range of Z over which Auger emission predominates becomes even larger. The probability that an X-ray will be emitted is called the fluorescence yield  $\omega$ , and it is simply the ratio of the X-ray emission cross section  $\sigma_x$  to the inner shell ionization cross section  $\sigma_i$ . Thus,

$$\omega = \frac{\sigma_x}{\sigma_i} = \frac{\sigma_x}{\sigma_x + \sigma_A} \quad \text{where}$$

$\sigma_A$  is the cross section for Auger emission. An excellent review of inner-shell vacancy production in ion-atom collisions has been written by Garcia et al (1973).

(d) Penetration of Ions and Heating Effect

It has been shown in section 1.3.1(a), that an energetic ion on collision with the solid surface has a high probability of electron capture and neutralisation. Thus in essence we are concerned with the passage of an atom into the solid surface, assuming that the neutralised state is maintained. The motion is then a series of two body collisions with the lattice atoms and the trajectory is determined principally by the collision parameters at each isolated impact. In this way the primary will proceed through the lattice losing energy and causing displacement of the target atoms. Evidently it will suffer a change of direction at each encounter and the actual motion is a complicated trajectory which will be different for each incident particle. However, the incident will come to rest when it no longer possesses sufficient kinetic energy to surmount the potential energy barriers offered by the lattice atoms and we assume this to be about 25 eV, since the binding energy as regards dynamic displacements are of this order. The positions at which the incidents come to rest will be at interstitial or lattice substitutional sites. The displaced atoms can dissipate their energy by heating up the solid or the energy can be stored in the lattice as potential energy.

1.3.2 Elastic Effects

(a) Ion Reflection

In the section on inelastic collisions, the secondary effects arising from ion bombardment have been presented. However, it must be realised that ions of the incident beam may be reflected without neutralisation or they can be reflected after neutralisation.

Unfortunately there is some confusion in the literature when referring to reflection coefficients as reference is made to ion reflection coefficients and total reflection coefficients. Since the probability of neutralisation of the incident ion is quite high, it is clear that the number of reflected ions is unlikely to bear much resemblance to the total number of incident species backscattered. Also there will be a dependence upon the angle of incidence with respect to the target normal. For the purpose of this discussion we shall consider ions incident normally to the target surface.

An ion reflection coefficient,  $R$  is defined as the number of reflected ions to the number of incident ions;

$$R = \frac{I_{2i}}{I_{1i}} \quad \text{where}$$

$I_{2i}$  is the number of reflected ions and  $I_{1i}$  is the number of incident ions. Hagstrum (1961) has studied this phenomena for noble gas ions on clean tungsten surfaces and finds that the reflection coefficient varies between  $10^{-4}$  and  $10^{-2}$ . The energy range studied was from 0 to 1 keV. As might be expected, the higher value was for the lightest ion and the smallest for the heaviest ion. For a particular ion there does not appear to be any dependence on the ion energy. Further work employing ion energies up to 14 keV has found the same sort of values for the ion reflection coefficients.

The total reflection coefficient is defined as the total number of incident species reflected, to the number of incident ions;

$$R_t = \frac{A_t}{I_{1i}} \quad \text{where}$$

$A_t$  is the total number of the incident particles reflected.

Radioactive tracer techniques were employed by Brown and Davies (1963) in order to measure the reflection coefficient of argon, krypton and

xenon on a number of metals. Their results indicate that above about 5 keV the reflection coefficient is less than a few per cent, but as the energy is reduced to below 1 keV the reflection coefficient rises to 50 - 80%. The reflection coefficient was considerably larger for xenon on tungsten than on aluminium, and a higher energy was required before it decreased to less than 5%.

#### (b) Sputtering

A very important effect that is produced by ion bombardment is that of ejection of particles from the target, or the process known as sputtering. The basic mechanism involves a reversal of the incident momentum carried by the ions so that target atoms are ejected from the surface over a wide range of angles. A sputtering coefficient  $S$  is defined as the number of atoms liberated per incident particle. Although the majority of the ejected species are neutral atoms, a small proportion are ejected as ions (about 1 in  $10^4$ ). As sputtering forms a major part of the experimental work described in this thesis, Chapter 2 has been entirely devoted to this phenomena.

### 1.4 Applications of Ion Bombardment

Ion bombardment is a technique of wide application. The ion energy, beam current and current density are the three important parameters which determine the use. In the following sections some of the more important uses will be considered.

#### 1.4.1 Secondary Electron Multiplier Detectors

As has been mentioned previously, the secondary electron emission coefficient is usually of the order of unity for most materials for an ion energy of about 10 keV. There are certain copper-beryllium compounds which are efficient in producing secondary electrons, having yields in the region of ten electrons per incident

ion at 20 keV. These type of compounds are used in the construction of secondary electron multiplier detectors.

#### 1.4.2 Ion Induced X-ray Analysis

The energy spectra of the X-rays emitted are very dependent on the atom from which they originate and hence offer the possibility of a technique to identify the constituents of surface films. As far as surface studies are concerned, a major problem which arises when electrons are used as the probing beam is the poor depth resolution resulting from the relatively large depth over which the X-rays are generated. With ion bombardment this is not the case and another important advantage is that the continuous background (bremsstrahlung) resulting from the retardation of the probing particles is much less intense. Morgan (1975) discusses ion bombardment techniques and applications.

#### 1.4.3 Surface Cleaning

Low energy ions can be used to remove surface contaminants, oxide layers and adsorbed gas molecules. The ion energy is usually only a few hundred eV and the experiments are performed in UHV systems with background pressures of the order of  $10^{-9}$  torr. For example, using the technique of Auger electron spectroscopy (AES), it is possible to carry out elemental analysis on materials on the top few atomic layers.

#### 1.4.4 Secondary Ion Mass Spectrometry

This technique is one of the many surface analytical techniques in use. The secondary ions of the target material produced by the incident beam can be mass analysed and thus identified. Werner (1974) has given a detailed review of this technique, in which he discusses the advantages and disadvantages.

#### 1.4.5 Ion Inplantation

This process employs very high energies, in the region of 100 keV and higher. It has a major use for doping semiconductor materials for use in various solid state devices. The examples of specific uses are numerous and some are given by Mayer et al (1970).

#### 1.4.6 Ion Etching

Ion bombardment can be used to etch various materials for in depth structural information. This relies on the ejection of the target species, either as neutral atoms or ions. The ion energies used are usually less than about 10 keV. The applications of the technique of ion etching is the main subject of this thesis and will be discussed in greater detail in the next chapter on sputtering.

## CHAPTER 2

### SPUTTERING

In the earlier work on sputtering (Grove 1852), the pressures used were of the order of 0.1 torr so that reproducible results on sputtering yields could not be expected. The effect of the pressure in the system was first demonstrated by Penning and Moubis (1940), who coupled a magnetic field to the ion source in order to increase the electron path lengths and thus maintain the discharge at lower pressures. Most of the early work was undertaken by Timoschenko (1941) and Fetz (1942) on sputtering yields and a great deal of work on the subject has since been carried out. Many reviews have been published, such as those of Kaminsky (1965) and Carter and Colligon (1968). Only some of the important and well known results will be discussed in this thesis.

The work of Wehner<sup>1</sup> (1955) using a mercury pool discharge apparatus for measuring sputtering coefficients must be mentioned, together with that of Keywell (1955) and Southern et al (1963). These workers provided valuable data on sputtering yields of various materials and most of their results have not required any substantial modification since.

The sputtering yield  $S$ , is defined as the number of atoms sputtered per incident ion. The variation of yield with ion energy is well established. It is found that no sputtering occurs below a threshold energy which is characteristic of the particular ion-target combination. Subsequently, the yield increases quite rapidly with ion energy up to about 5 keV and then starts to level off,

reaching a maximum at about 10 keV. Above this energy the yield stays constant until about 100 keV and then starts to fall. The falling point is where the ions are penetrating deep into the solid and are being implanted. Figure 4 shows the variation of the sputtering yield with ion energy for argon ions bombarding a copper target at normal incidence. This diagram is taken from Tsong and Barber (1973), who use the results of five different groups of workers to plot the curves.

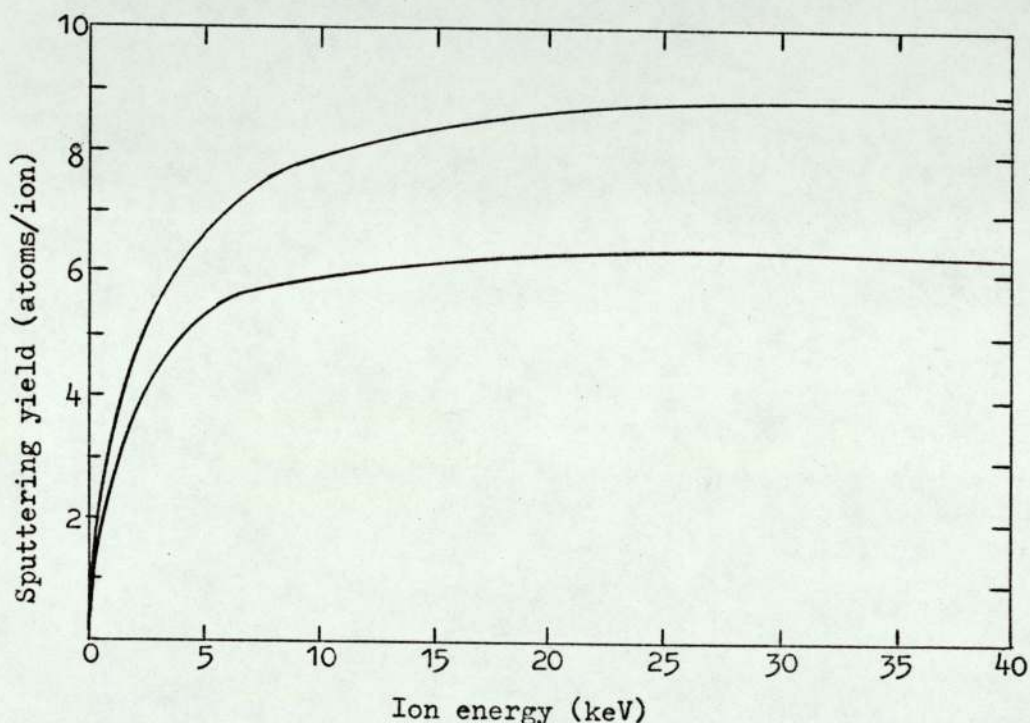


Figure 4. Variation of sputtering yield with ion energy for polycrystalline copper. (After Tsong and Barber 1973).

Rosenburg and Wehner (1962) have carried out many experiments to determine the variation of sputtering with the target material. They found that the sputtering yield follows closely the state of the electron concentrations in the 'd' shells and also bears some resemblance to the heats of sublimation. The variation of yield with ion species has also been studied and it is found that the yield

increases fairly steadily within each group of elements, reaching a maximum for the inert gas species of the group. The sputtering yield has a high dependence on the angle of incidence with respect to the target normal. It increases to a maximum between about  $55^{\circ}$  to  $75^{\circ}$ , depending upon the ion-target combination. Figure 5 shows the variation of sputtering yield with angle of incidence for silica glass. A plot of the function  $\sec \theta$  is also shown, where  $\theta$  is the angle of incidence of the ion beam.

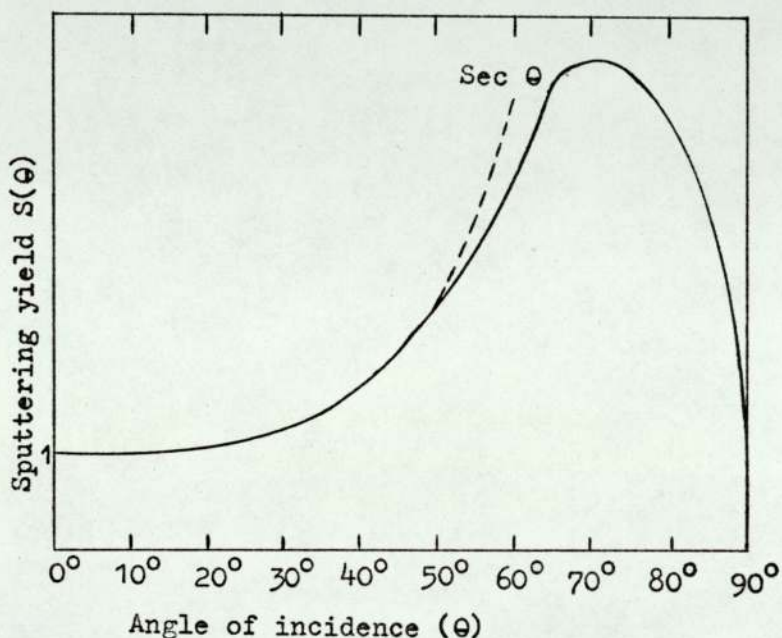


Figure 5. Variation of sputtering yield with angle of incidence for silica glass. (After Tsong and Barber 1972).

Some work has also been done on the measurement of threshold energies for sputtering. Wehner (1957) devised an ingenious method for doing this which required the measurement of the intensity of the light transmitted through the sputtered deposit. The results obtained by this particular technique were only relative but could be calibrated by comparing them with the weight-loss technique. A disadvantage of this method was that it relied on all the deposits striking the window and sticking to the surface. Also when studying materials such as tantalum and thorium which oxidised quickly to a

more transparent film, errors could not be avoided. Figure 6 shows yield energy curves near threshold for some metals for argon ion bombardment.

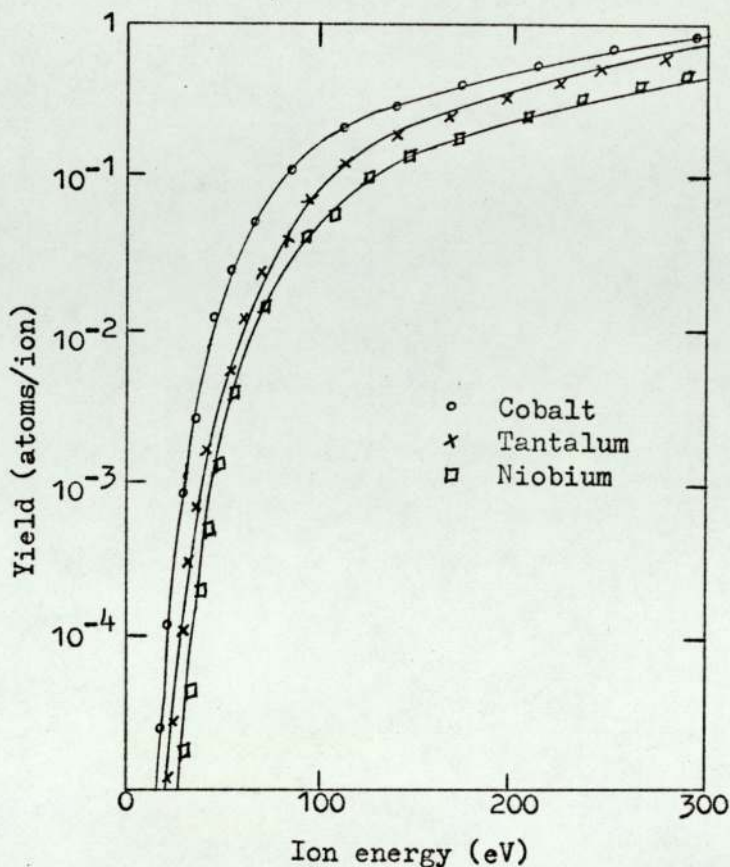


Figure 6. Yield-energy curves near threshold for some metals for argon ion bombardment. (After Carter and Colligon 1968).

The process of sputtering was for a long time regarded as being due to a thermal spike or 'hot spot' phenomenon, (Von Hippel 1926). It was believed that the energy of the incident ion heated a small volume as it slowed down in the lattice and there was then evaporation from this point until the heat diffused away. This mechanism was believed up to the mid fifties until the discovery of preferential directions of ejection from sputtered single crystals, (Wehner 1956). Subsequently, it was also shown that the average

energy of the ejected atoms was about 7-10 eV, being an order of magnitude higher than that which could be explained by evaporation.

## 2.1 Theory of Sputtering

There have been three main theories formulated about sputtering. These are due to Brandt and Laubert (1967), Thompson (1968) and Sigmund (1969). Tsong and Barber (1973) reproduce the above theories in a condensed and comprehensive form. They then compare the experimental data about sputtering with theory and show how well the results are explained by each theory. In the present work only some of the important results emerging from Sigmund's theory will be given since this seems to give better agreement with experimental results than the other two. However, in order to get an overall view of all three theories, the above mentioned review is recommended.

Sigmund's theory is applicable to both amorphous and polycrystalline targets. It is based on random collision processes, applying Boltzmann's equation and general transport theory. The target material being bombarded is considered to have a planar surface. Consider an ion starting its motion at a time  $t = 0$  in a plane  $x = 0$  with an arbitrary velocity vector  $V$ , (see figure 7). The function,

$$G(x, V_0, V, t) d^3V_0 \quad \dots (2.1)$$

describes the average number of atoms moving at time  $t$  in a layer between  $x$  and  $x + dx$  with velocities between  $V_0$  and  $d^3V_0$ . The sputtering yield for backward sputtering of a target with a plane surface at  $x = 0$  is then given by;

$$S = \int d^3V_0 |v_{0x}| \int_0^\infty dt G(0, V_0, V, t) \quad \dots (2.2)$$

where the integration over  $d^3V_0$  extends over all  $V_0$  with negative  $x$

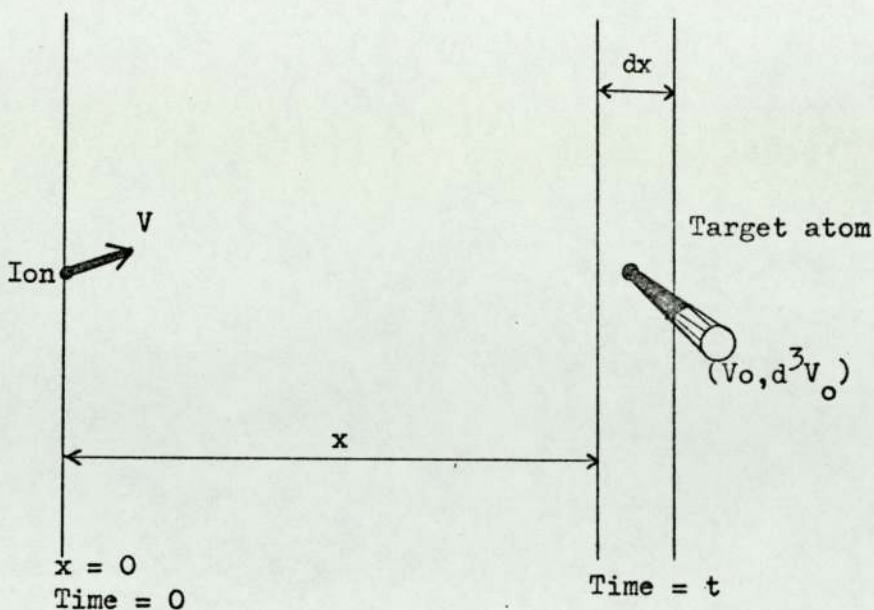


Figure 7. Geometry of sputtering calculation. (After Sigmund 1969).

components large enough to overcome surface binding forces. In a similar way, the yield of transmission sputtering through a surface at  $x = d$  is given by;

$$S = \int d^3v_0 |v_{ox}| \int_0^\infty dt G(d, v_0, V, t) \quad \dots (2.3)$$

Sigmund then introduces the function

$$H(x, V) = \int d^3v_0 |v_{ox}| F(x, v_0, V) \quad \dots (2.4)$$

which represents the sputtering yield for the case where the collision cascade starts at  $x = 0$  and the sputtered surface is in the plane  $x$ . The function  $H(x, V)$  is measurable in principle for  $x \leq 0$  which is the case of backward sputtering. The next step is to replace the velocity variables with energy variables and the sputtering yield is given by;

$$S(E, \eta) = H(x = 0, E, \eta) \quad \dots (2.5)$$

where  $E$  = energy of the incident particle and  $\eta$  = the direction

cosine relative to x - axis. The Boltzmann transport equation is then set up and Legendre polynomials are used to solve it.

$$H(x, E, \tau) = \sum_{l=0}^{\infty} (2l + 1) H_l(x, E) P_l(\tau) \quad \dots (2.6)$$

where  $P_l(\tau)$  are Legendre polynomials.

In order to solve the Boltzmann equation, other quantities have to be included. The three major ones being the electronic stopping cross-section, the differential cross section for elastic collisions and the surface binding force. The sputtering yield  $S = H(x, E, \tau)$  is then given by;

$$H(x, E, \tau) = \frac{3}{4\pi^2} \frac{F(x, E, \tau)}{N C_0 U_0} \quad \dots (2.7)$$

where  $F(x, E, \tau)$  is the amount of energy deposited in a layer  $(x, dx)$  by an ion of energy  $E$ , starting at  $x = 0$  and by all the recoil atoms.  $N$  is the atomic density of the target.  $U_0$  is the surface binding force which affects the ejection of a surface atom and is of the order of a few eV for most metals.  $C_0$  is a constant derived from the cross section and

$$C_0 = \frac{1}{2} \pi \lambda_0 a^2 \quad \text{where}$$

$$\lambda_0 = 24 \quad \text{and} \quad a = 0.219 \text{ \AA}$$

The angular dependence of the sputtering yield is given by

$$S = (\cos \theta)^{-\frac{5}{3}} \quad \dots (2.8)$$

The theory as briefly outlined shows good agreement with experimental results in most cases.

## 2.2 Applications of Sputtering

It has been previously stated in Chapter 2, that the sputtering

yield is fairly constant between an ion energy of about 10 keV and 100 keV. Thus sputtering applications usually employ ion energies below 10 keV, since there is no advantage in using higher energies. The applications can be broadly divided up into, the production of thin films, machining and thinning of materials and ion etching, and these will be discussed in this section.

### 2.2.1 The Production of Thin Films

Sputtering is being increasingly used for the production of thin films as an alternative to evaporation, (Holland and Priestland 1972). The main advantage is the versatility of the process, since any metal or compound can be sputtered. It is also found that films produced by sputtering show much better adhesion than those produced by evaporation. The reason for this is that the energy of sputtered atoms, (about 10 eV) is typically 100 times higher than by evaporation. The greater energy is thought to give sufficient surface mobility to allow the arriving atoms to reach positions of low potential energy on the surface.

Mattox (1974) discusses the ion plating of various different types of material by the sputtering of both conducting and non-conducting targets. He stresses the point that for insulators an rf substrate bias must be used. He goes on to say that the improved adhesion, contact resistance, improved surface coverage and morphology of ion plating is of extreme interest to the microelectronics industry for metallization purposes, and to industry as a whole for providing wear-resistant and corrosion-resistant coatings.

### 2.2.2 Machining and Thinning of Specimens

A great deal of work has been carried out on this technique by many different workers. The thinning technique can be used to

prepare samples for transmission electron microscopy as discussed by Barber (1970). The thickness required is usually less than about 2000 Å, although thicker foils can be used in high voltage electron microscopes. During this process the specimen is rotated and bombarded on each side using two ion guns. Goodhew and Hepburn (1972), using the above type of technique, report the thinning of individual carbon and glass fibres for transmission electron microscopy. They claim that it was not possible to do this work by any other technique.

Bayley and Townsend (1972) report the machining of a 15 μm deep groove in a 25 μm thick glass plate using nitrogen ions of 5.6 keV energy. This work again was not suited to other techniques such as mechanical or chemical machining. Pearson and Harsell (1972) reported the polishing of scratched glass specimens using ion milling and showed that it was a new and promising technique. Spencer and Schmidt (1972) used ion machining to drill holes as small as 0.375 mm in diameter into diamond, more than 1.5 mm in thickness. They used an ion gun working at a voltage of 7.5 keV and a beam current of 100 μA. The milling rate was about 130 μm/hr. Yasuda (1974) used 10 keV argon ion beams focussed to 30 μm in diameter to make a parabolic surface of a 200 x 200 μm<sup>2</sup> area on a silicon single crystal.

### 2.2.3 Sputter Ion Etching

The ion etching of materials to reveal microstructure is a very important application of the sputtering process. Ion beam etching and its applications have been discussed in a recent article by Norgate and Hammond (1974). Gloersen (1975) undertook a systematic investigation of etch rates of several materials and the dependence of etch rate on beam parameters and the angle of incidence.

The first report indicating that ion etching was superior to chemical etching was made by McCutcheon (1949). He found that ion etching of steel forgings brought out the flow-lines much more clearly and sharply than hitherto had been obtained by chemical etching. Subsequent to this, a great deal of work has been carried out and is still in progress in laboratories all over the world, which is beginning to show the versatility of ion etching as applied to very different types of materials. Some of the major advantages of ion etching as compared with other techniques such as chemical and electrolytic etching are;

- (i) It can be universally applied to all species.
- (ii) No contamination of the specimen can occur by the etchant.
- (iii) There is far greater control over the etching rate as compared with chemical etching.
- (iv) Selected areas can be etched as required by masking techniques and there is no undercutting as with chemical etching.

The surface structure resulting from ion etching, generally arises from differences in the sputtering yield for different substances or physical states. Another contributing effect when etching crystals is that the atoms are removed preferentially in the direction of closest packing, the latter are sputtered more rapidly than the low density planes. This mechanism which is the inverse of the chemical one, reveals the microstructure of the metal. This phenomenon of selective etching is in reality a very complex one and depends on a number of factors such as the energy and density of the beam and the direction of incidence. In this way it is possible

to determine the exact conditions of bombardment under which a family of planes will be observed.

### Single Crystals

Silsbee (1957) proposed that in monocrystals, energy could be transported along a line of atoms and could be focussed into the line. It was shown that this effect would occur if  $D < 2RT$  and also if  $\cos \theta_0 \geq \frac{D}{2RT}$  where  $RT$  is the combined radii of the two colliding spheres,  $D$  the interatomic spacing in the atomic row under consideration and  $\theta_0$  the angle which the primary recoil atom makes with this row. From the above expressions one can deduce that more focussing should occur in directions where  $D$  is the smallest, that is to say in close-packed directions, which for bcc. crystals are the  $\langle 111 \rangle$  directions and for fcc. crystals are the  $\langle 110 \rangle$  directions. Clearly effects such as preferred orientations and fibrous structure observed on some etched surfaces are undoubtedly tied to the focussing effect. Also this effect explains the fore-mentioned phenomenon of selective sputtering of crystals, where greater impact is produced on the denser planes which are revealed preferentially.

### Etching of Alloys

Only a small amount of work has been done in this field. Diffraction patterns carried out on alloys such as  $\text{Cu}_3\text{Au}$  after bombarding with 5 keV noble gas ions, (Gillam 1959), showed that the composition of the first few atomic layers had been changed. Initially, these became richer in gold near the surface, but with continued etching, three times as much copper as gold was eroded, whilst the gold diffused into the bulk metal. Two further observations were made. Firstly, it was noticed that the higher the ion energy, the lower the gold concentration in the altered surface layer; 68% gold at 30 eV and 45% gold at 3 keV for argon ion

bombardment. Secondly, it was found that the layer of altered composition was thicker for light ions (helium, 40 - 80 Å) than for heavy ions (xenon, 30 - 40 Å). Wehner (1958) studied yields of nickel base alloys, aluminium alloys and some steels under .1 to .5 keV mercury ion bombardment and found that in general, the yields were in accordance with yields of the component elements.

### Etching of Insulators

When etching insulators, there is the problem of charge accumulation on the surface if etching is carried out with a dc. source. In order to neutralise this charge, low energy electrons are usually injected on to the target from a suitably biased heated filament or other electron gun arrangement. Some apparatus rely on the neutralisation being caused by electrons produced by collisions of the ions with beam limiting apertures or with the target holder assembly. If an rf. source is used, then this problem does not arise since there is no time for charge to build up, because the polarity of the discharge electrodes is being rapidly reversed.

It has been shown by Navez et al (1962), that the structure obtained on glass surfaces by ion etching is in many instances a function of the angle of incidence, the time of bombardment and the energy of the incident ions. This particular result and other results such as those of Tsong and Barber (1972) on the development of surface topography on silica glass, will be discussed more fully in Chapters 6 and 7, in relation to the authors own work on etching various different types of materials.

The most important piece of apparatus of an ion beam etching system is the ion source itself. A brief discussion about ion sources will be given in the next chapter and a more detailed discussion on the types of sources used in this investigation.

## CHAPTER 3

### ION SOURCES

#### 3.1 Requirements of an Ion Source for Etching

Ion etching systems require to be operated at pressures of less than  $10^{-4}$  torr in the specimen chamber, in order to reduce contamination of the sample. This is usually achieved by differential pumping, whereby the ion source is at a higher pressure than the sample, thus as the source pressure is increased, the diffusion pump speed must be increased accordingly. It is also very desirable that the source can be used with insulating as well as conducting materials. The problem of charge build upon non conducting specimens has already been mentioned, together with the techniques by which it can be overcome. The ion beam should be well collimated and preferably without any complex focussing and extraction electrodes. The majority of sources require magnetic fields in order to increase the electron path lengths and this restricts their application in situations where strong magnetic fields cannot be tolerated. The source should be stable in operation, without the need for continuous supervision. It is not essential that the ion beam should be monoenergetic and indeed in certain applications it is desirable that the ions should have a broad energy spectrum in order to provide differential etching on the same sample. In general ion energies up to 10 keV and current densities in the range of 100 to  $300 \mu\text{A}/\text{cm}^2$  are used.

There are many different types of ion sources now available, but only three types are extensively used for ion etching, namely

rf sources, hot cathode sources and cold cathode sources. These will be only briefly dealt with, followed by a more detailed discussion on the saddle field ion sources, which were found to be most suited for this work in view of the requirements discussed above.

### 3.1.1 Radio Frequency Sources

In the radio frequency ion sources, a gas discharge tube is coupled to an rf tuned circuit and a high frequency field applied. Essentially, its operation depends on the electrons gaining energy from the rf field and ionizing gas atoms in their oscillatory path. A magnetic field is used in order to confine the discharge to a small region, which is usually at a pressure of about  $10^{-2}$  to  $10^{-3}$  torr. To carry out etching at pressures of less than  $10^{-4}$  torr, differential pumping has to be employed. However, an advantage of this source is for etching insulating materials, since charge build up on the specimen does not occur due to sequential bombardment by electrons.

### 3.1.2 Hot Cathode Sources

The simplest type of thermionic ion source that is also widely used in mass spectrometry is the Nier source. Basically, this operates on the principle that electrons emitted by a hot tungsten filament are accelerated out of this volume by a suitably biased electrode to direct the ions at the target. This type of source operates at about  $10^{-4}$  torr but the ion current is of the order of nano amps. Currents approaching  $1 \mu\text{A}$  can be obtained, but then the operating pressure has to be increased to more than  $10^{-3}$  torr. The energy spread of the ions is very small, being 2 to 3 eV.

A very popular type of source, including several different versions, is the duoplasmatron ion source. This again employs a heated filament to produce the electrons for ionization, which are accelerated towards the anode through the gas to be ionized, which is

present at a pressure of  $5 \times 10^{-2}$  torr. An arc strikes between the filament and anode and is confined to a very small region by the use of a magnetic field and a biased electrode. The energy spread of the ions is between 6 to 10 eV. A disadvantage of all thermionic sources is that the filament may burn out if there is a sudden change in pressure, unless elaborate protection systems are incorporated.

### 3.1.3 Cold Cathode Sources

These sources are basically modified forms of the Penning Gauge and consist of a hollow cylindrical anode and two plane circular cathodes, placed at each end of the anode. A magnetic field is applied parallel to the cylinder axis, constraining the electrons to move in a tight helix as they pass from cathode to anode, thus increasing the electron path lengths. The electrons oscillate through the anode causing ionization and the ions can be extracted through a small hole in one of the cathodes. A cold cathode discharge can be maintained at pressures of the order of  $10^{-5}$  torr.

A relatively new type of ion source which does not require a filament as a source of electrons or a magnetic field to extend the path of the electrons, but still operates at low pressures - about  $10^{-6}$  torr - is the Saddle Field Ion Source. Another important advantage of this source is for etching insulators, It has been shown, (Ghander and Fitch 1974), that the ion beam produced by this source contains electrons and energetic neutrals and thus it can be used with non-conducting specimens. Two versions of the source have been used in the present investigation and both will be considered in detail in the rest of this Chapter.

### 3.2 The Electrostatic Charged Particle Oscillator

In 1966 McIlraith suggested that two positively charged parallel electrodes should constrain negatively charged particles in

oscillatory paths between the electrodes. This idea came about from his work on rubber analogue models which he was using to simulate electron paths in X-ray tubes. He also suggested that in a similar way, the gravitational field due to a double star should be able to hold particles ranging in size from dust particles to small planets in a state of permanent oscillation. McIlraith constructed an oscillator in the form of a cylinder closed by plane end caps to prevent particles from drifting out of the system. For the anodes he used thin tungsten wires which were pulled tight and clamped by means of screws. A disadvantage of this system was that the wires, which were heated by the electron bombardment, bowed and became slack, causing the performance to deteriorate drastically. This problem was overcome by using springs to keep the wires under tension.

Most of the further development of the oscillator was undertaken by the Physics Department of the University of Aston in Birmingham. Thatcher (1970) describes an ion pump based upon the oscillator principle and Fitch et al (1971) describe a new type of oscillator gauge with a sensitivity of  $2000 \text{ torr}^{-1}$  and a low pressure limit of  $2 \times 10^{-10} \text{ torr}$ .

The theoretical work on the oscillator was carried out by McIlraith (1967) and only some of the more important results will be quoted. He used digital computer techniques in order to investigate the trajectories followed by charged particles within the oscillator. In figure 8, consider an infinitely long oscillator of radius  $R$  metres, with two infinitely long anodes situated at a distance  $b$  metres from the origin on either side. If the charge on the anodes is  $+q$  coulombs per unit length and a charged particle starts from rest at some arbitrary point  $P(x, y)$ , the potential at  $P$  relative to that at  $O$  can be shown to be given by:-

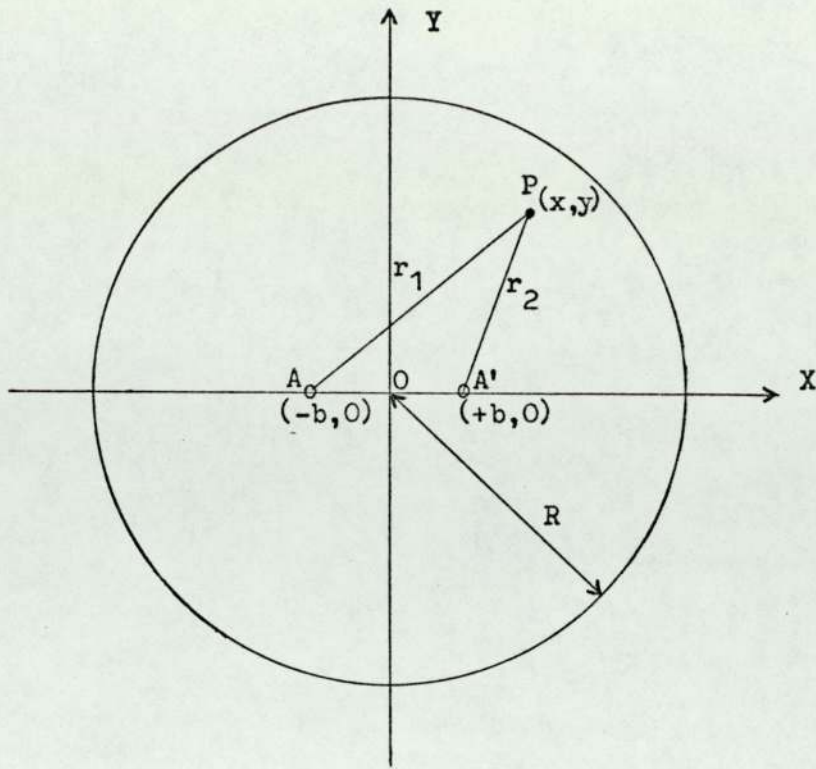


Figure 8. Diagram for calculating the potential distribution within the oscillator.

$$V_{xy} = \frac{q}{4\pi\epsilon\epsilon_0} \ln \frac{b^4}{r_1^2 r_2^2}$$

$$V_{xy} = \frac{q}{4\pi\epsilon\epsilon_0} \ln \left[ \frac{b^4}{(y^2 + (x-b)^2) (y^2 + (x+b)^2)} \right]$$

where  $\epsilon$  is the dielectric constant which is unity for vacuum and  $\epsilon_0$  is the permittivity of free space.

Differentiating with respect to  $x$  and  $y$  gives the field in the  $x$  and  $y$  directions respectively;

$$E_x = -\frac{q}{4\pi\epsilon\epsilon_0} \cdot \frac{4_x (x^2 + y^2 - b^2)}{(y^2 + (x+b)^2) (y^2 + (x-b)^2)} \dots\dots\dots (3.1)$$

$$E_y = -\frac{q}{4\pi\epsilon\epsilon_0} \cdot \frac{4_y (x^2 + y^2 + b^2)}{(y^2 + (x+b)^2) (y^2 + (x-b)^2)} \dots\dots\dots (3.2)$$

From equation (3.1) we see that  $E_x = 0$  for  $x = 0$  and also when  $x^2 + y^2 = b^2$ . This means that  $E_x$  is zero on the Y-axis and also on a circle with AA' as diameter. Inside this circle, the force  $F_x$  on an electron is away from the Y-axis, while outside this circle, it is towards the Y-axis. The force  $F_y$  on an electron is always towards the X-axis. From equations (3.1) and (3.2);

$$\frac{E_y}{E_x} = \frac{y}{x} \cdot \frac{(x^2 + y^2 + b^2)}{(x^2 + y^2 - b^2)}, \text{ and this approaches}$$

$$\frac{y}{x} \text{ when } x^2 + y^2 \gg b^2$$

The saddle point is a point of unstable equilibrium, but electrons can oscillate through it in stable trajectories in the general direction of the Y-axis.

In parallel with the work on the development of the oscillator as an ion pump and an ultra high vacuum ion gauge, some work was also done in using the oscillator as an ion source. The latter development has, in fact, proved to be the most significant and two types of ion source have now been produced, namely the cylindrical source and the spherical source. A great deal of the work on the former type has again been carried out at Aston University, while the latter type has been developed more recently by Ion Tech Associates.

### 3.3 Saddle Field Ion Source of Cylindrical Geometry

Fitch et al (1970) described the first version of this source in which an aperture was milled into the cathode cylinder, directly above the anodes in the centre as shown in figure 9. The ions produced in the discharge are then allowed to escape through the aperture. The ions gain their energy from the field inside the oscillator and emerge as a reasonably well collimated beam. Further

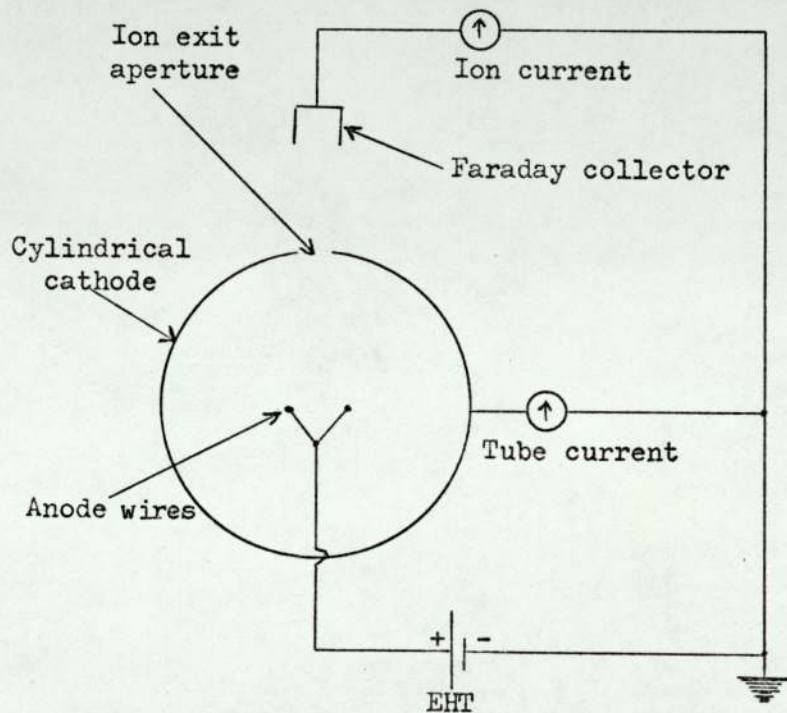


Figure 9. Schematic diagram of cylindrical ion source. (After Fitch et al 1970).

development work was undertaken by Fitch and Rushton (1972) to produce an improved form of the source. A major problem with the earlier version was that the very thin tungsten wire anodes frequently burnt out. Fitch and Rushton (1972) investigated the effect of varying the spacing and diameter of the anodes and came to the conclusion that the spacing was the critical factor. A source employing 2mm diameter tungsten rod anodes was found to give nearly as good a performance as one having 0.25 mm diameter tungsten wire

anodes, providing the surface to surface spacing was the same.

Rushton et al (1973) described the modes of operation of the ion source and also employed direct gas injection into the inside of the source for the first time, as first described by Franks (1972). This was found to have the advantages that the specimen stage in the vacuum chamber could be maintained at a much lower pressure for a given ion beam density, thus reducing the total gas throughput, contamination of the specimen and scattering of the ion beam. Essentially, three modes of operation of the ion source were found, the 'oscillating mode', the transition mode' and a general 'glow discharge mode'. In the oscillating mode, the ion gun was found to exhibit a narrow intense central region which was attributed to the high stability associated with electrons oscillating on the Y axis.

During some experiments on focussing the ion beam, Ghander and Fitch (1974), incorporated a small chimney on to the ion exit aperture and showed that this improved the performance of the source. They suggested that this may be due to the partial correction of the field disturbance arising for a simple circular aperture. This effect has been studied at some length by the author and will be discussed in this Chapter. Although higher beam current densities could be obtained using a focussing system, it was found that the etching rates were very low for insulating materials, presumably on account of the removal of the low energy electrons by the negatively charged focussing electrode. Khorassany (1976), has shown that the energy spectrum of the source is broad, but contains two distinct peaks, one at an energy equivalent to the saddle point potential and the other at about 38% of the anode potential.

Although this source has been developed significantly for it to be useful in a number of applications, it was not entirely suitable

Discussion

for the present investigation and experiments will now be described, which were undertaken to optimise the design of the source for in-situ ion etching in the scanning electron microscope.

### 3.3.1 Water Cooled Source

Some preliminary investigations in this laboratory showed that it would be feasible to incorporate large diameter water cooled tubular anodes for stable operation at high power. There were three main reasons for designing and testing an ion source using water cooled electrodes. Firstly, the anodes get extremely hot under electron bombardment, reaching temperatures as high as 1000°C with 2mm diameter tungsten rod anodes. The specimen being etched is thus heated due to both ion bombardment and thermal radiation from the anodes. Water cooling of the anodes can completely remove the latter effect. The second reason is that under normal operating conditions using tubular anodes, the performance of the ion source is found to decrease by up to 40% within about the first one hour of operation. Thus many adjustments in pressure and voltage are required initially in order to maintain the desired etching conditions. Thirdly, when operating at a tube current of more than 6 mA, fluctuations and instability occurs. The ceramic insulators, made from a soft porous material known as Ceramtec, were seen to glow at the start of each experiment for up to 30 minutes. This glowing is predominant at the start and then gradually gets less and less as the ceramics are degassed. If the anodes were examined after approximately 1 hours operation, then a build up of black contamination was found on the surface. This effect was found to be worse on the thicker tungsten anodes, (more than 1.5 mm diameter), but was found to be very bad indeed on the stainless steel tubular anodes. The author constructed an ion source suitable for the study of these contamination and

deterioration effects.

The source is shown in figure 10 and consisted of a cylinder of

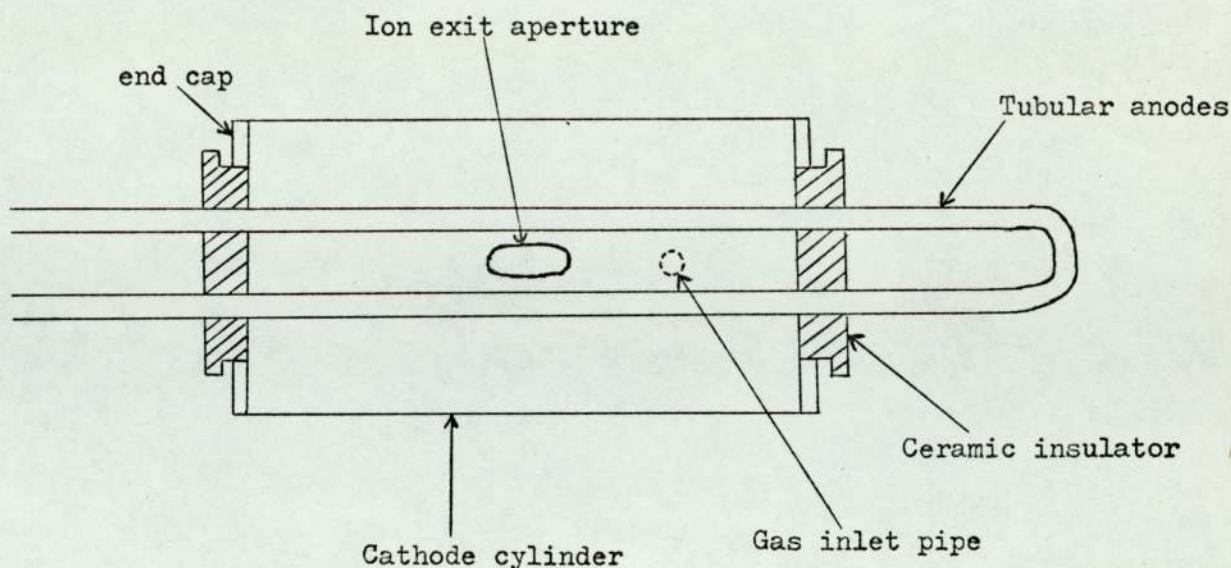


Figure 10. Diagram of water cooled source.

length 76 mm and diameter 38mm. The anodes were stainless steel tubes of diameter 3mm at a separation of 8mm. They were held rigidly in position and isolated from the cathode by ceramic insulators 25mm in diameter, which were located into the end caps by means of screws. The ion exit aperture was rectangular of size 12.5 x 3mm. A tightly spiralled tube of stainless steel, 3mm in diameter wrapped around the cathode cylinder, (not shown in the diagram), was used when it was required to cool the latter. The cooling water was fed into the vacuum system by P.T.F.E. tubes which fitted to the ends of the anode tube by screw connectors. The length of tubing used from the end of the anode to the flange on the inside of the chamber, was about 1.75 metres for the water inlet and outlet. This length was necessary to reduce the leakage current to less than 0.2 mA when the anodes were at 10 kV.

The results showed that if water-cooling of the cathode only was carried out, deterioration in performance with time was still

obtained, although this was not as serious as with no cooling at all. The anodes were covered with the black contamination but again this effect was also reduced. If the anodes were cooled, then the deterioration in performance was only a few per cent and there was no black contamination on the anodes but a blue coloured film. With the anodes and cathode both cooled, there was no deterioration and stable operation, even at very high tube currents, could be maintained for long periods. The anodes were not covered by any black contamination but by a light blue film deposited smoothly on the surface. In order to find the reason for this deterioration in performance under normal operating conditions (i.e. without cooling), it was decided to employ scanning electron microscopy to examine the surface of the anodes under various conditions. A set of anodes which had been used under normal operation for 3 hours at about 4 to 5 mA tube current were cut to the size required for mounting in the scanning electron microscope. A 'Varian' crimping tool was used for this purpose in order not to disturb the surface structure in any way. Similar specimens were prepared from a set of anodes which had been used with anode and cathode cooling and also a set of new clean anodes.

Electron micrographs of the specimens were taken with a Cambridge 'Stereoscan' and these are shown in plate 1. This shows 4 micrographs of the anodes, where the first 3 have been taken at a magnification of 13,000X and the angle between specimen and beam being  $45^{\circ}$ . The last micrograph, (d), is taken at a magnification of 5,200X with the electron beam travelling almost along the surface of the specimen at glancing incidence. Micrograph (a) shows the surface of a clean anode and this is seen to be scratched and uneven. Micrograph (b) shows the surface of an anode after it has been used with anode and

The surface of a clean new anode.

(a)

2  $\mu\text{m}$

The surface of an anode after it has been used with anode and cathode kept cool.

(b)

2  $\mu\text{m}$

The surface of an anode after using under normal operation, showing the uneven black deposit.

(c)

2  $\mu\text{m}$

The surface of an anode after using under normal operation, taken with the electron beam at glancing incidence.

(d)

5  $\mu\text{m}$



cathode kept cool and the surface can be seen to be fairly smooth. Micrographs (c) and (d) show the surface of the anode under normal operation and the very uneven structure of the black deposit is clearly seen. The deposit was seen to be cracked in many places and was in the form of quite large lumps. The lump that is seen in micrograph (d), which is taken at an angle of  $2^{\circ}$  between the specimen surface and the beam, has an approximate size of  $8 \mu\text{m} \times 65 \mu\text{m}$ . Electron probe microanalysis of the 3 samples, showed that they all contained the same elements present in the same proportions, these being mainly ferrous and chromium.

The contamination is thought to be caused by the breakdown of the pump oil molecules in the vicinity of the hot anodes, due to electron bombardment. It was concluded that the blue coloured film and the black deposit is mainly composed of carbon. It is not surprising then that the probe analysis did not show this since the minimum X-ray wavelength detectable by the instrument was that of sodium, which is atomic number 11. The diffusion pump oil used was Santovac 5, a polyphenyl ether. When the breakdown of this oil occurs near a cool surface due to electron bombardment, then smooth conducting polymer films are produced, (Cleaver and Fiveash 1970). If however, the breakdown occurs at sustained high temperatures, such as the temperatures reached by the anodes under normal operation, then complete cracking can occur to form a black deposit of carbon, (Holland and Laurenson 1964). The deterioration in performance of the ion source in normal operation can be explained as due to perturbations of the electric field between the anodes caused by the uneven carbon deposit on a microscopic level. This causes the oscillating electrons to be deviated from their normal equilibrium paths and to be captured by one or other of the anodes within a much

shorter path length than normal.

The conclusions to be drawn from this work are as follows. The general instability of the source at high tube currents in normal operation is caused by the outgassing of the ceramic insulators. The black contamination was more serious on stainless steel tubular anodes than on tungsten rods of the same diameter and this is undoubtedly due to the different nature of the two materials. On tungsten anodes less than 2mm in diameter, the black contamination is rarely seen. This is because of the much higher temperature reached by the thinner anodes, results in the black carbon deposit being burnt off the surface as it forms. Water cooling of the source gives stability by keeping the ceramic insulators at low temperature and also allows the formation of conducting polymer films on the cool anode surfaces which are not detrimental to the performance. The water cooled source employing both cooling of the anodes and cathode is thus most suitable for stable operation at very high tube currents. These favourable factors give an obvious choice for this source to be employed for experiments such as the field distortion effects of the ion exit aperture, which are discussed in the next section.

### 3.3.2 Distortion Effects of the Ion Exit Aperture

It has already been suggested that the distortion of the field in the vicinity of the ion exit aperture is a probable cause for the poor performance of the ion source and this effect has been investigated in detail. The existing cathode cylinder of the water cooled tube was modified so that the rectangular aperture (12.5 x 3)mm was enlarged to a circular aperture 12.5mm in diameter. Another aperture of the same size was milled into the side of the tube at 90° to the first aperture, along the same centres. Stainless steel sheet of thickness 0.3mm and width 22mm was wrapped around the central

portion of the tube so as to cover these two larger holes. Four holes of diameters 2.5, 5, 7.5 and 10mm were positioned around this sheet so that when one of these smaller holes was in position over one of the 2 underlying larger holes, the second hole was completely covered.

At a fixed voltage of 10 kV, readings of tube current were taken at various pressures with a particular aperture in one of three positions, firstly at the normal central position, secondly displaced to one side from the centre to the edge of the larger hole and then thirdly when the aperture had been turned through  $90^\circ$  to the side of the tube. These positions are schematically illustrated in figure 11 for a 2.5mm aperture being in position. For simplicity, the other 3

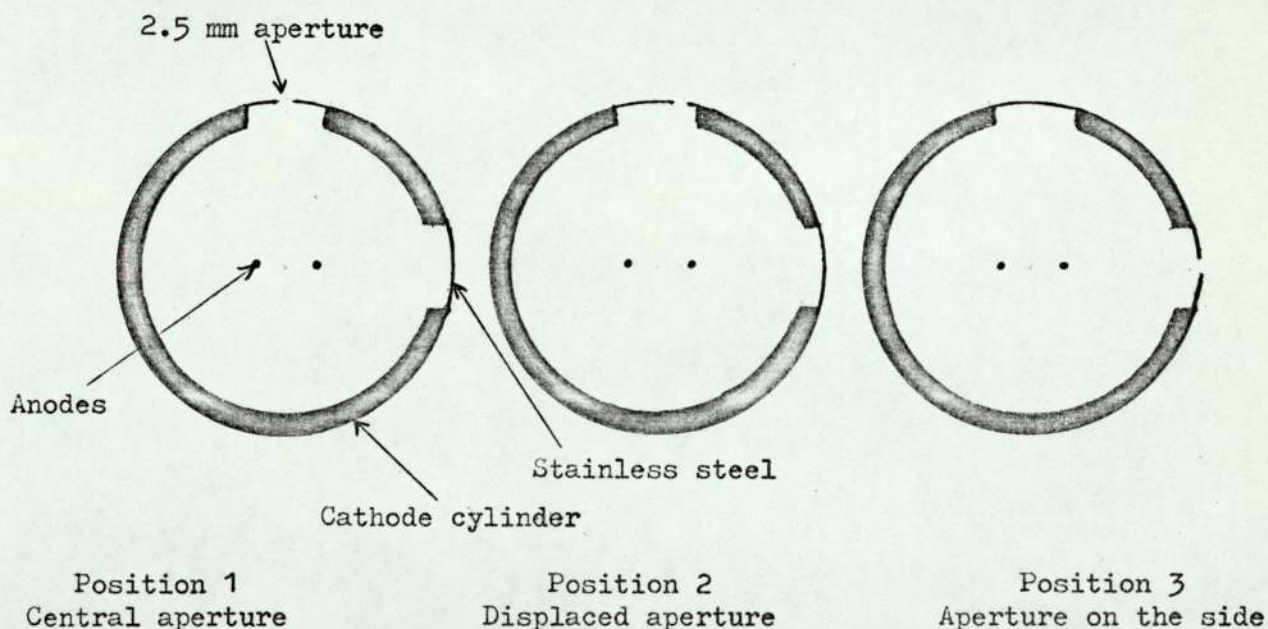


Figure 11. Illustrating the 3 different positions for the aperture.

apertures in the stainless steel sheet are not shown. In order to make the interpretation of the results easier, two quantities were defined as below. A ratio  $R_n$ , was defined as;

$$R_n = \frac{I_t}{I_s} \quad \text{where}$$

$I_t$  is the tube current when the aperture is in the normal central position and  $I_s$  is the tube current when the aperture has been turned through  $90^\circ$  and is on the side. A second ratio was defined as;

$$R_d = \frac{I_d}{I_s} \quad \text{where}$$

$I_d$  is the tube current when the aperture is in the displaced position. From the graph in figure 12 of  $R$  as a function of pressure, it is seen that  $R_d$  is unity over a large region for the 2.5mm and 5mm diameter apertures. In the case of the 7.5mm diameter aperture,  $R_d$  is greater than  $R_n$  but is less than unity. For the 10mm diameter aperture,  $R_d$  and  $R_n$  were found to be the same. In all cases the maximum value of  $R_n$  can be seen to be between about 0.85 and 0.9.

These results indicate that the field disturbance produced by the various apertures is most important when the aperture is in position centrally on the Y-axis, so as to affect the trajectories of the most stable electrons. If it is displaced to one side from the centre to the edge of the large hole, then the disturbance was found to be unimportant for the 2.5mm and 5mm apertures. However, when we are considering the 7.5mm diameter aperture,  $R_d$  is seen to be less than 1, presumably because even in the displaced position, this aperture is still affecting the trajectories of the very stable electrons oscillating on the Y-axis. This was confirmed using the large 10mm aperture.

The cathode tube was further modified so that distortion experiments employing two apertures could be carried out. Another two 12.5mm diameter holes were drilled into the cylinder directly

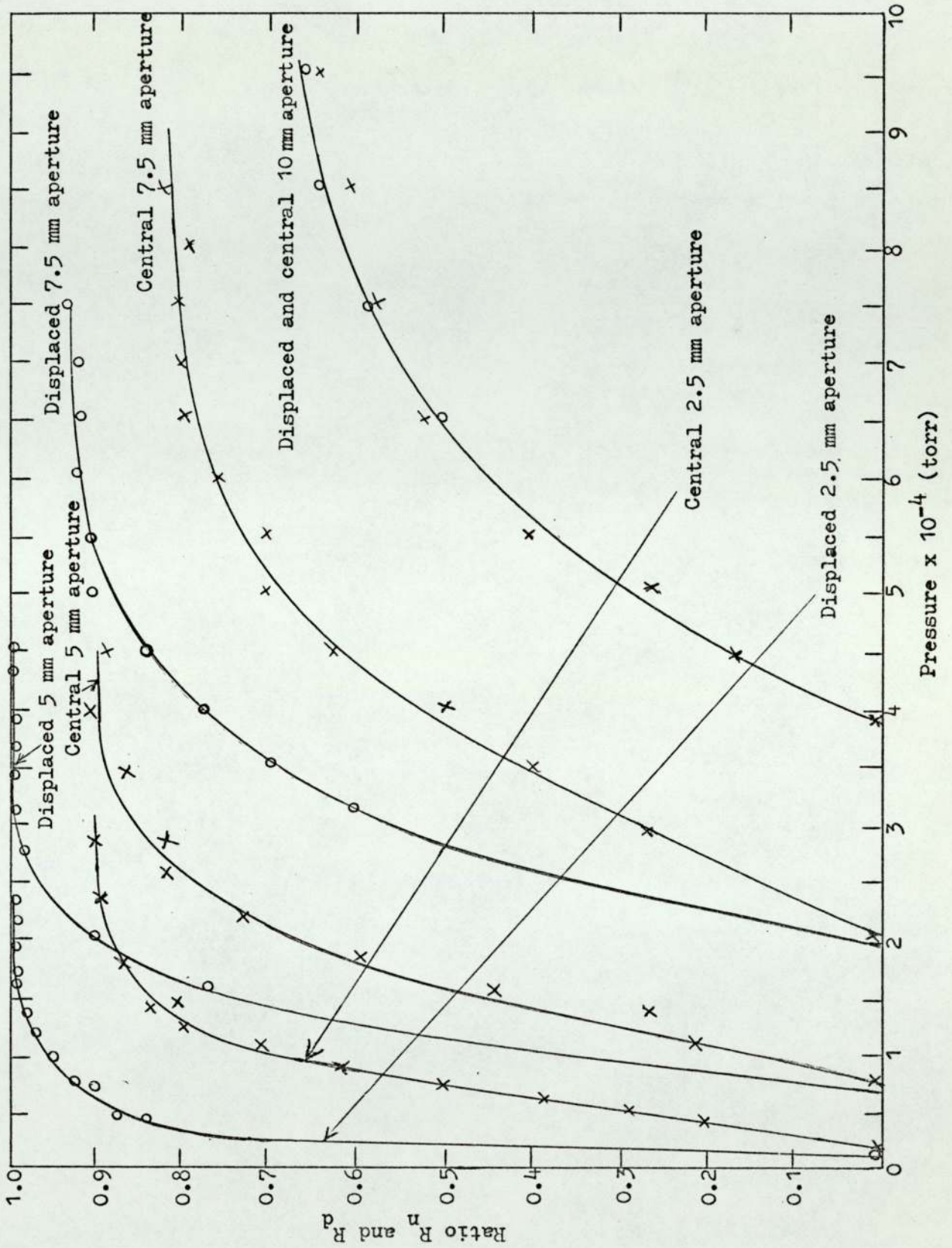


Figure 12. Graph of  $R_n$  and  $R_d$  as a function of pressure.

opposite the existing large holes. Two apertures were made from 0.3mm thick stainless steel with 5mm holes in them together with three blanks. Experiments were carried out with the two apertures diametrically opposite each other in the normal central position, while the holes on the sides were covered by the blanks and then vice versa. The performance of the tube was found to be very bad indeed and contrary to expectation no difference in the tube currents for the two different positions was obtained. It was then decided to try to repeat the distortion experiments with just one 5mm diameter aperture and to compare with the results previously given in figure 12. However, these results could not be reproduced either. The reason for these problems was attributed as being due to the ever present disturbance produced by the larger holes. Even when three of these holes were covered with stainless steel foil and a 5mm aperture positioned over the 4th hole in the normal central position, the field disturbance arising from the "step" caused by the thickness of the cathode (1.6mm), was sufficient to completely mask the true disturbance effect of the smaller aperture. This 'step' effect is illustrated in figure 13. This effect was also present for the previous results but with the further modification it has been considerably increased and is completely masking the field disturbance arising from the smaller apertures.

In order to show that this reasoning was valid, 5 stainless steel plugs were made so as to fit into the larger 12.5 mm diameter holes. The plugs were a flush fit against the inside of the cylinder and were made to follow the curvature of the cathode body. A 5mm

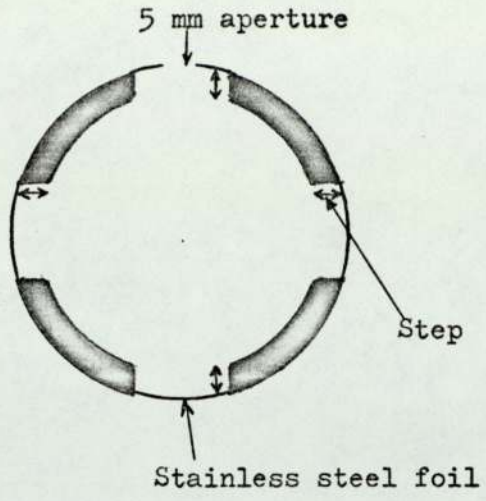


Figure 13. Illustrating the step due to the thickness of the cathode.

diameter hole was drilled in the centre of 2 of these plugs and these were used for the distortion experiments. One of these plugs is shown in figure 14. Five positions were investigated having one

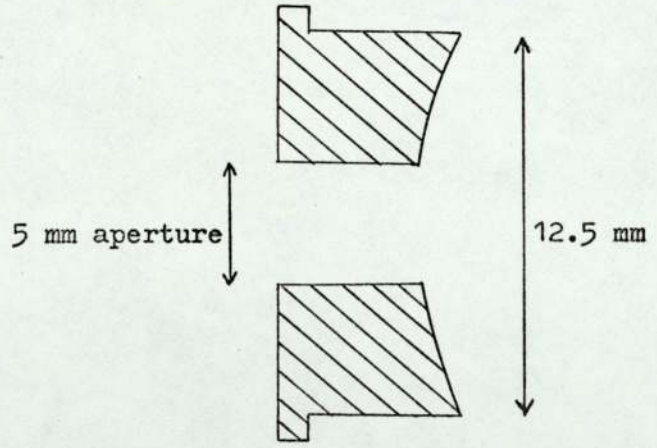


Figure 14. Stainless steel plug with a 5mm aperture.

and two apertures and these are shown in figure 15. The results are plotted in figure 16 as the ratio  $R_n$  against pressure and for positions 1 and 2 this was found to be close to unity for a large range of pressure. Positions 3 and 5 gave the same results as each

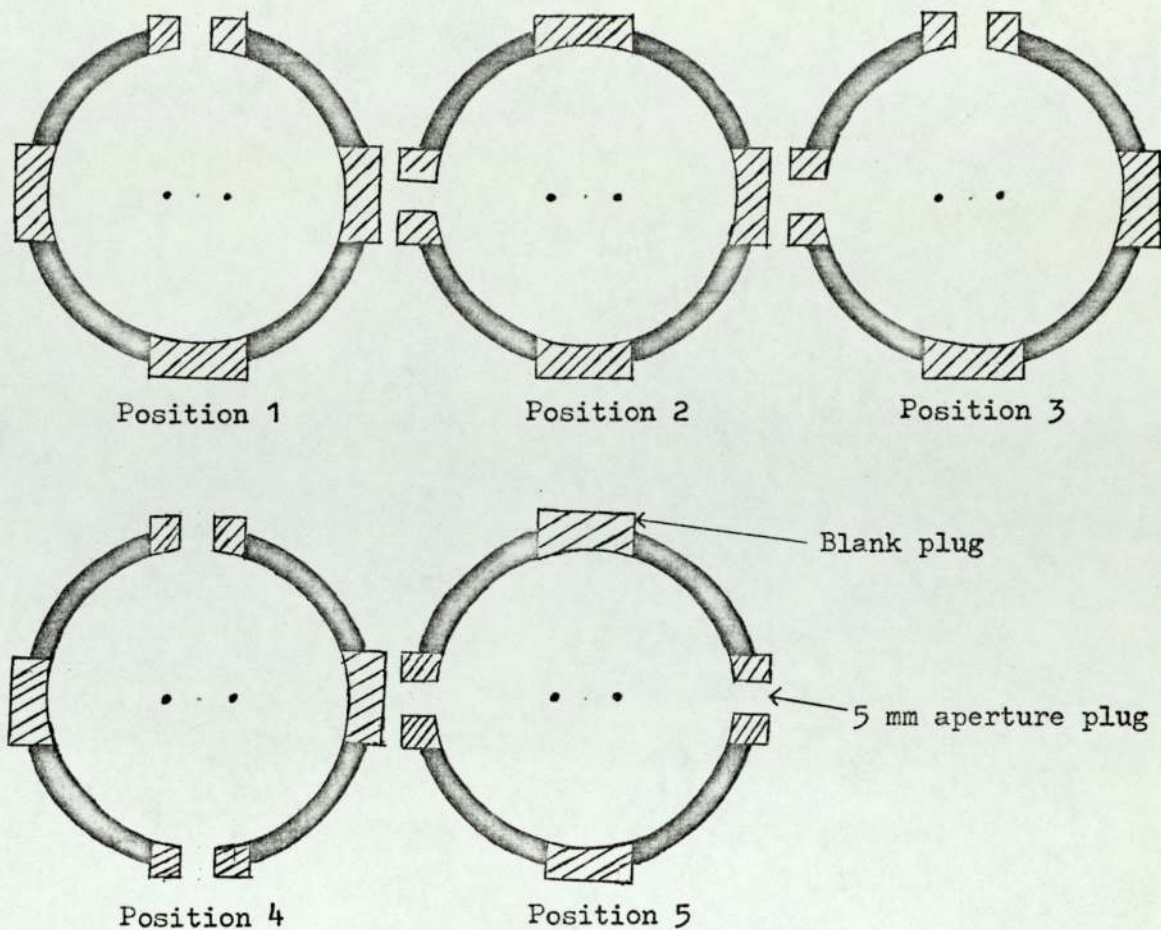


Figure 15. Illustrating the five different positions of the apertures.

other, while position 4 was considerably less. In the case of the two apertures,  $R_n$  is the ratio of the tube current in positions 3 or 4 to that of position 5.

These results indicate that for one aperture the field disturbance is negligible even in the exact central position, while for two apertures diametrically opposite each other in the central position, the disturbance is important. This is contrary to the results in figure 12 and the improvement in performance is thought to be made by the plug acting as a chimney aperture of height 4mm, which is sufficiently long compared to its diameter to give nearly complete correction of the field disturbance. For the two apertures there is

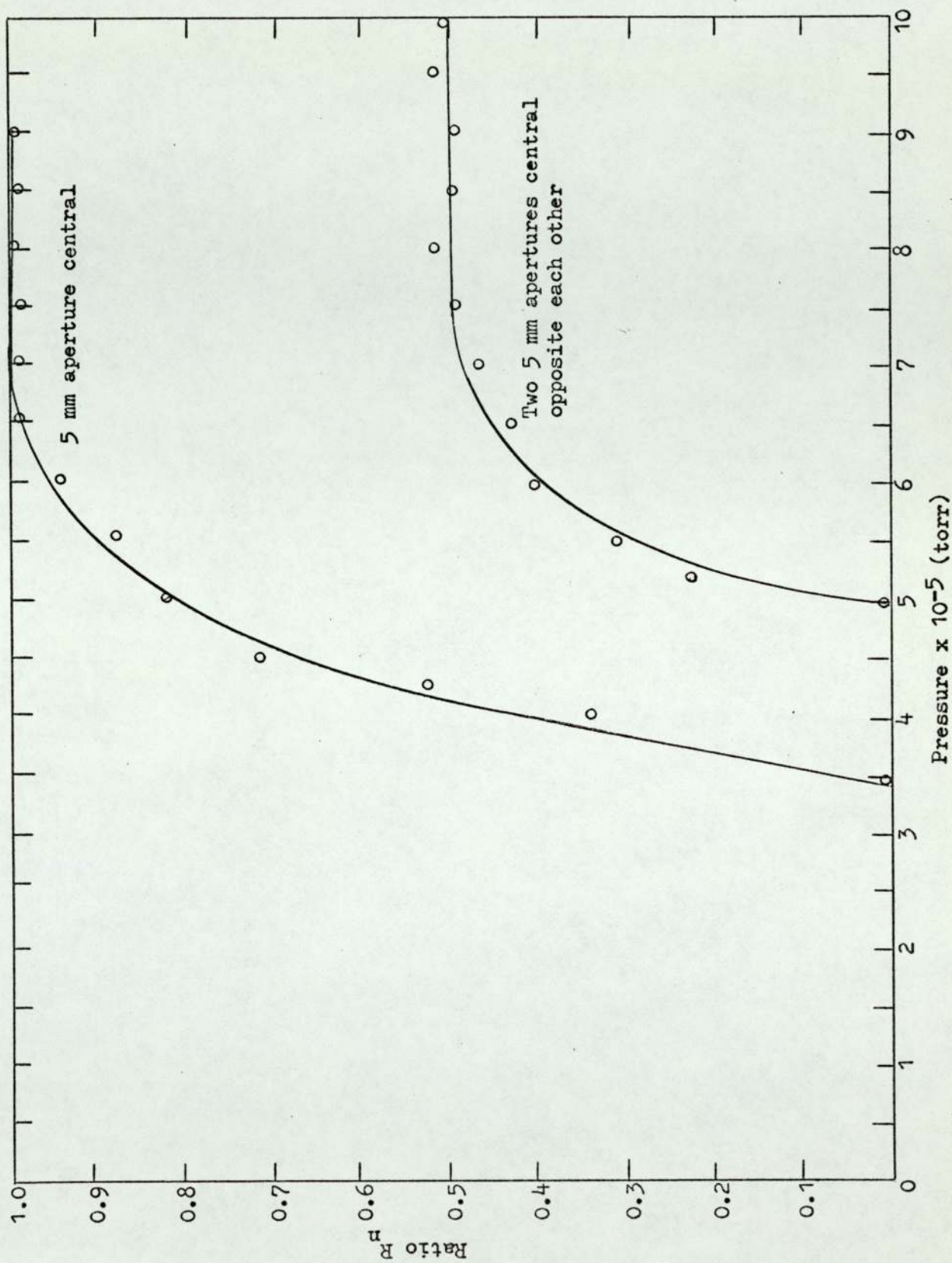


Figure 16. Graph of  $R_n$  against pressure.

some loss of performance since residual disturbances of the field at opposite ends of the electron trajectory will be much more serious than when it only occurs at one end.

These results have thus shown that a chimney of appropriate dimensions corrects the field disturbance giving a much improved performance, which is comparable to the performance when there is no disturbance, that is when the aperture is on the side and has been turned through  $90^\circ$ .

### 3.4 Saddle Field Ion Source of Spherical Geometry

This type of source is of recent origin and has been developed by Franks (1973) at Ion Tech Limited. It is a modification of the cylindrical ion source and produces a more intense and less divergent beam than the former. It has already been shown by Rushton et al (1973), that the beam profile from the cylindrical source contains an intense central region along the Y-axis, the extent of which is limited along the Z-axis due to the end effects arising from the cylindrical configuration. The idea has always been conceived that it may be possible to eliminate the end effects by having a spherical cathode concentric to a ring anode, thus producing a saddle point rather than a saddle line. A problem to be overcome is how to support the ring within the sphere, without disturbing the field. Such an arrangement would be expected to give a source of axial symmetry, capable of producing an energetic beam of ions.

Franks (1973) overcame these difficulties by using an anode disc and two guard rings either side of the disc, contained within the spherical cathode. A diagram showing the cathode and anode geometry is given in figure 17(a), together with a second diagram 17(b), showing the configuration now used, the modification having been made in 1975. The modified source allows for much easier alignment and

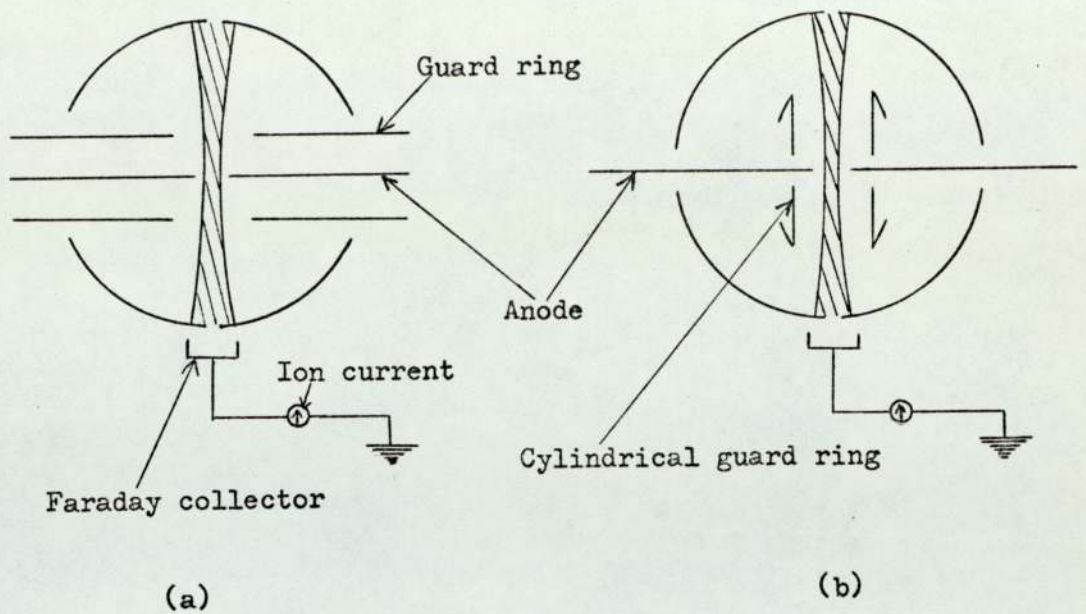


Figure 17. Showing the geometry of the earlier, and more recent, spherical source.

cleaning. The axis of symmetry is coincident with the centre of the ion beam. Two apertures are employed on diametrically opposite sides and the ion beam current from one aperture is continuously monitored by a Faraday cup. The paper by Franks and Ghander (1974) gives current-voltage characteristics for different gases at various pressures, together with some measurements of the energy distribution. This was found to be intense with a single peak at 0.85 of the anode potential, with a half width of 200 volts. Khorassany (1976) has confirmed the dominant nature of this high energy peak.

### 3.5 Applications of the Saddle Field Ion Sources

From the previous discussion in section 3.1, it is clear that the saddle field ion sources are particularly suitable for etching, machining and thinning of materials. Also they have already been used for a number of specific applications. Peggs and McIlraith (1973) used the thermionic version of the cylindrical source as a

sensitive time-of-flight molecular beam detector. Swaminathan and Venkatasubramanian (1974) described the use of the thermionic cylindrical ion source, as the source of a double focussing mass spectrometer. Burger and Maier (1975) described the use of a cylindrical source as the source for characteristic radiation in the ultraviolet region, suitable for photoelectron spectroscopy. They studied helium and neon and came to the conclusion that for helium suitable intense lines were obtained at  $304 \text{ \AA}$  and  $256 \text{ \AA}$ , while for neon the suitable wavelengths were  $461 \text{ \AA}$  and  $462 \text{ \AA}$ . A number of reports of the use of the spherical source for cleaning of surfaces on U.H.V. have been made, for example, the removal of oxide layers in ellipsometry, (Rehal 1976). At the moment an important advantage of the spherical source is that its compactness and very small size makes it ideal in situations where space is limited. However, work in progress in this laboratory, suggests that it should be possible to design a much smaller cylindrical source.

- 55 -

## CHAPTER 4

### EXPERIMENTAL ARRANGEMENTS FOR IN SITU ION ETCHING IN

#### THE SCANNING ELECTRON MICROSCOPE

#### 4.1 The Cylindrical Ion Source

Bearing in mind the problems discussed in section 3.3, a cylindrical source was designed and constructed for incorporation in the scanning electron microscope (SEM). The ceramtec insulators have been identified as the probable cause of the instability when operating at tube currents of more than about 6 mA. Curing these materials by baking at 1300°C gave some improvement, but complete solution to this problem was eventually found by changing to a glazed ceramic. Another limitation of the conventional source was due to breakdown occurring across the insulators after operation for between 10 to 15 hours, due to a build up of sputtered metal on the inside surface of the insulators. The end plates were re-designed to reduce this effect, thus allowing much longer operating times before the source required to be cleaned. Another feature considered to be essential in the design was the addition of a chimney to the ion-exit aperture, in order to reduce the field disturbance and thus improve the source efficiency. Since the deterioration in performance has been shown to be due to the black contamination on the stainless steel tubular anodes and this is not too serious for the thinner tungsten rods, water cooling of the source was not considered essential at this stage. Furthermore, the design of the specimen chamber is such that the specimen is at a relatively large distance from the source, so that radiation from the anodes is unlikely to be a serious problem.

The new source is shown diagrammatically in figure 18 and a photograph in plate 2 shows the source mounted on a flange ready for

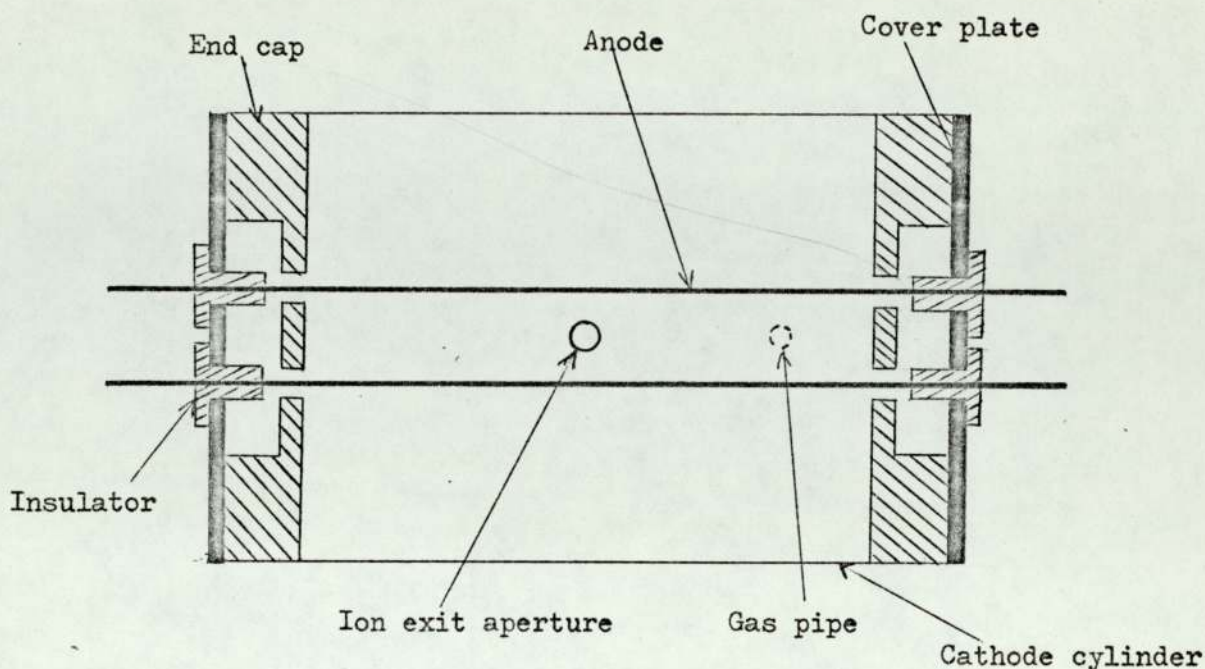
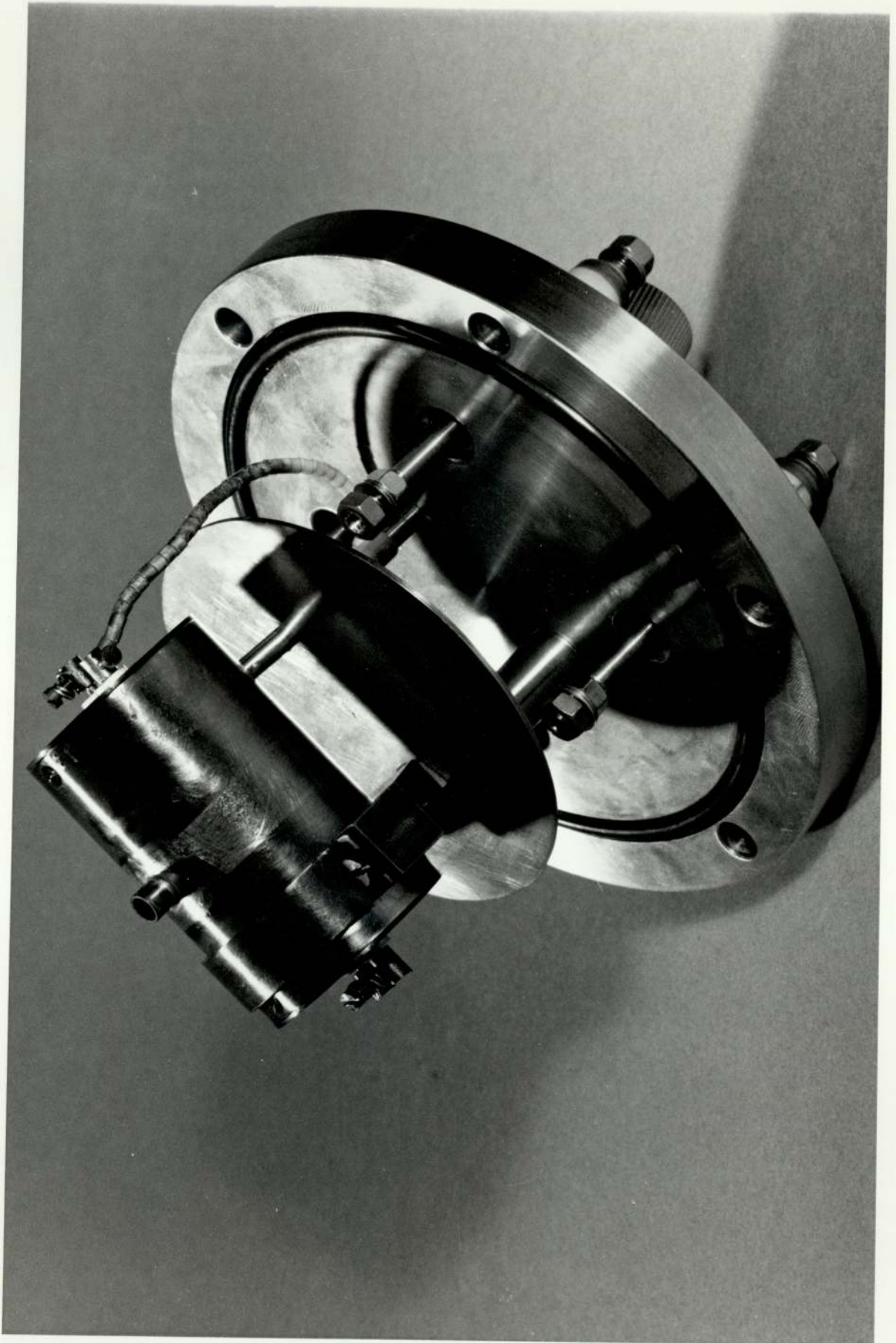


Figure 18. Diagram of the new cylindrical source.

insertion into the port on the specimen chamber. Essentially the source consisted of a stainless steel cylindrical cathode of length 64 mm and diameter 38 mm. The ion exit aperture was a chimney of diameter 5 mm and the height was also 5 mm. The anodes were made from tungsten, diameter 1.5 mm, with a surface to surface separation of 6 mm, which was found to be the optimum spacing (Fitch and Rushton 1972). The insulators were of a hard glazed material, manufactured by Smiths Industries, Rugby, under the trade name of Sintox. A bush with all the relevant dimensions is shown in figure 19. As can be seen, the internal diameter was slightly larger than the anode diameter and in order to make a tight fit, some sleeves were made from stainless steel sheet to fit over the ends of the anodes. The gas was led directly into the source by means of a 4.8 mm diameter stainless steel tube, diametrically opposite the aperture, but displaced to one side by 19 mm. The characteristics of this source

This plate shows the cylindrical source, ready for incorporation on to the port of the scanning electron microscope. The chimney ion exit aperture and the H.T. lead can be clearly seen.

Plate 2. Cylindrical source mounted on a flange.



are given in Chapter 5.

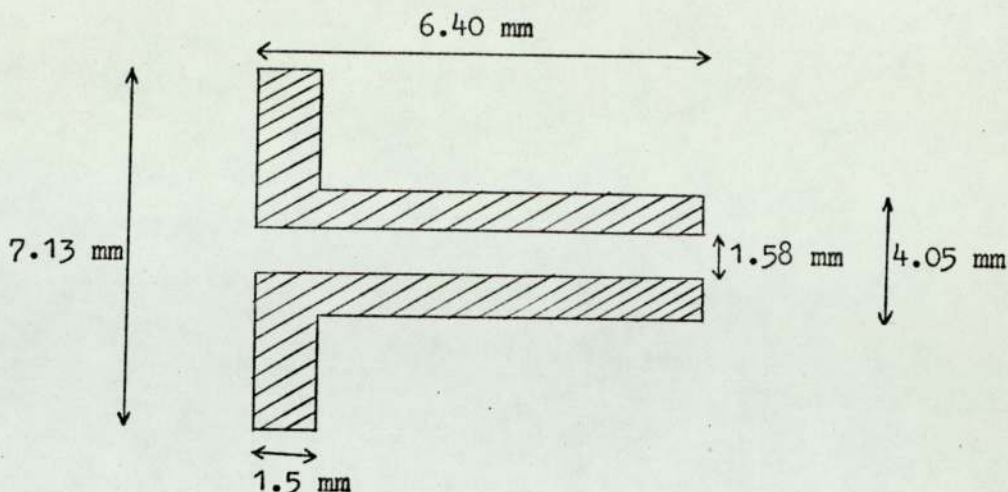


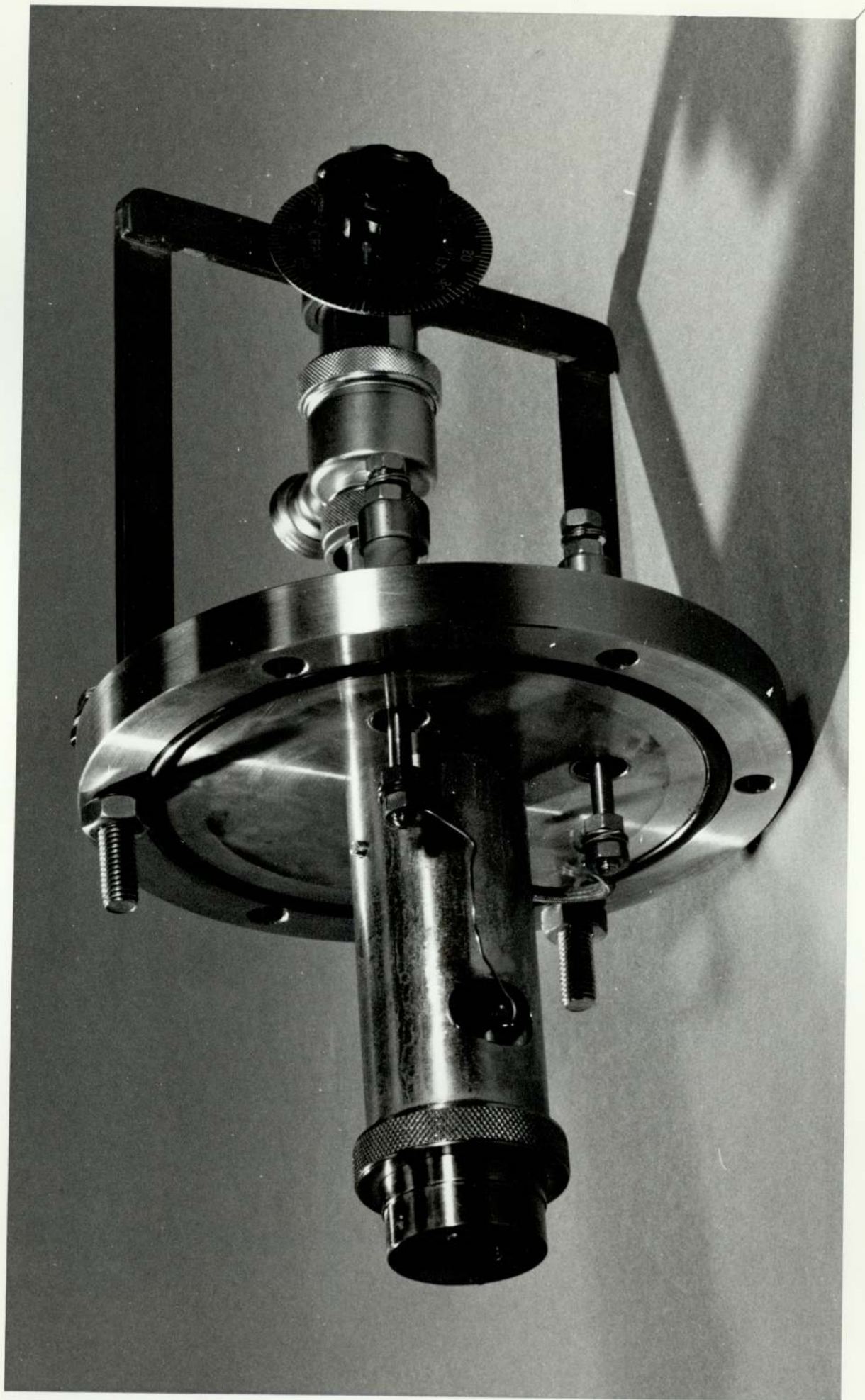
Figure 19. Sintox insulator.

#### 4.2 The Spherical Ion Source

The spherical source was acquired nearly a year after the programme of work commenced, so that some of the earlier work was carried out entirely with the cylindrical source. The source used was one of the first version produced by Ion Tech Limited. A diagram of this source is shown in figure 20 and a photograph of it mounted on a flange is given in plate 3.

The anode is of stainless steel of thickness 2 mm and contains a central hole of 5 mm diameter. The cathode is made from two hemispherical aluminium electrodes of radius 11 mm. Each cathode contains an aluminium insert of thickness 1.5 mm, so that ion exit apertures of different sizes can be used. This allows the inserts to be changed after they were damaged by continuous ion bombardment. The anode is situated between the stainless steel guard electrodes, diameter 10 mm which are at earth potential and is isolated from them by four ceramic insulators. The standard size of aperture used in the spherical source is 1.5 mm and this was found to be suitable to give the correct operating pressure in the microscope. The apertures were found to widen after only 50 hours of operation and in order to

This plate shows the spherical source mounted on a flange, ready for incorporation on to the port of the scanning electron microscope. Here again the small ion exit aperture can just be seen and the H.T. lead to the anode is also visible. For easy alignment, the source is mounted on top of the cylindrical pipe. A leak valve, which was quickly interchangeable from one source to the other is shown in position on the back of the flange.



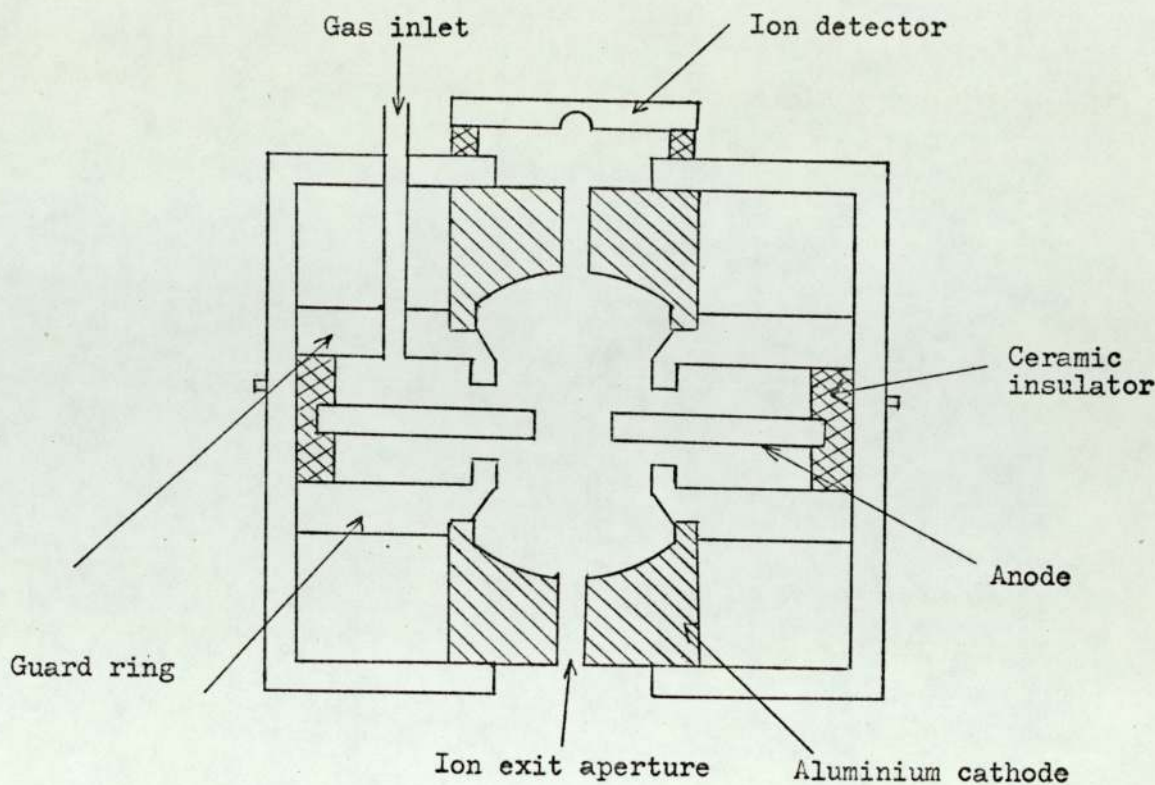


Figure 20. Diagram of the Spherical source.

reduce this problem, it was found desirable to make complete cathodes of thickness 3 mm which were found to operate for up to 100 hours. The characteristics of this source are also given in Chapter 5.

#### 4.3 Electrical Circuit

Figure 21 shows the electrical circuit used for the ion sources. The H.T. supply was a 10 kV, 10 mA, current stabilised unit.  $I_t$  is the tube current and  $I_b$  is the beam current impinging upon the samples. The H.T. lead of the cylindrical source can be seen in plate 2 and the lead of the spherical source is also visible in plate 3. This plate also shows the needle valve in position on the back of the flange and this was quickly interchangeable from one source to the other.

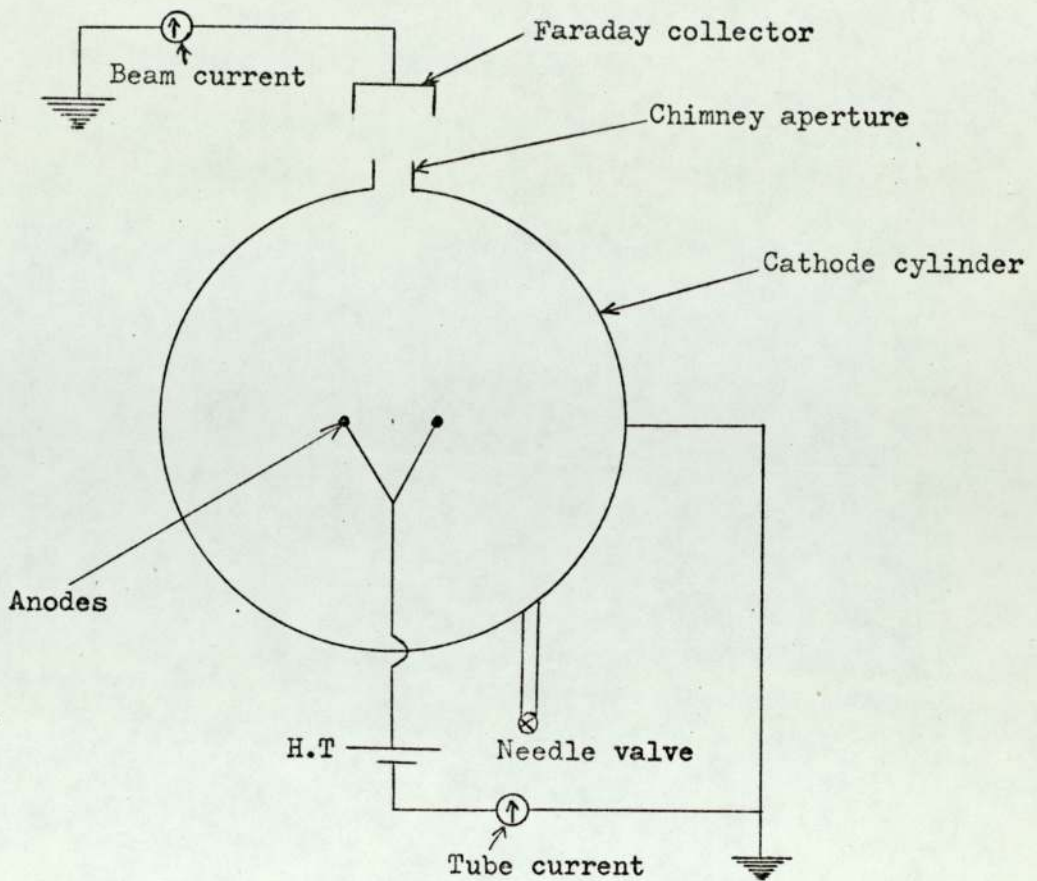


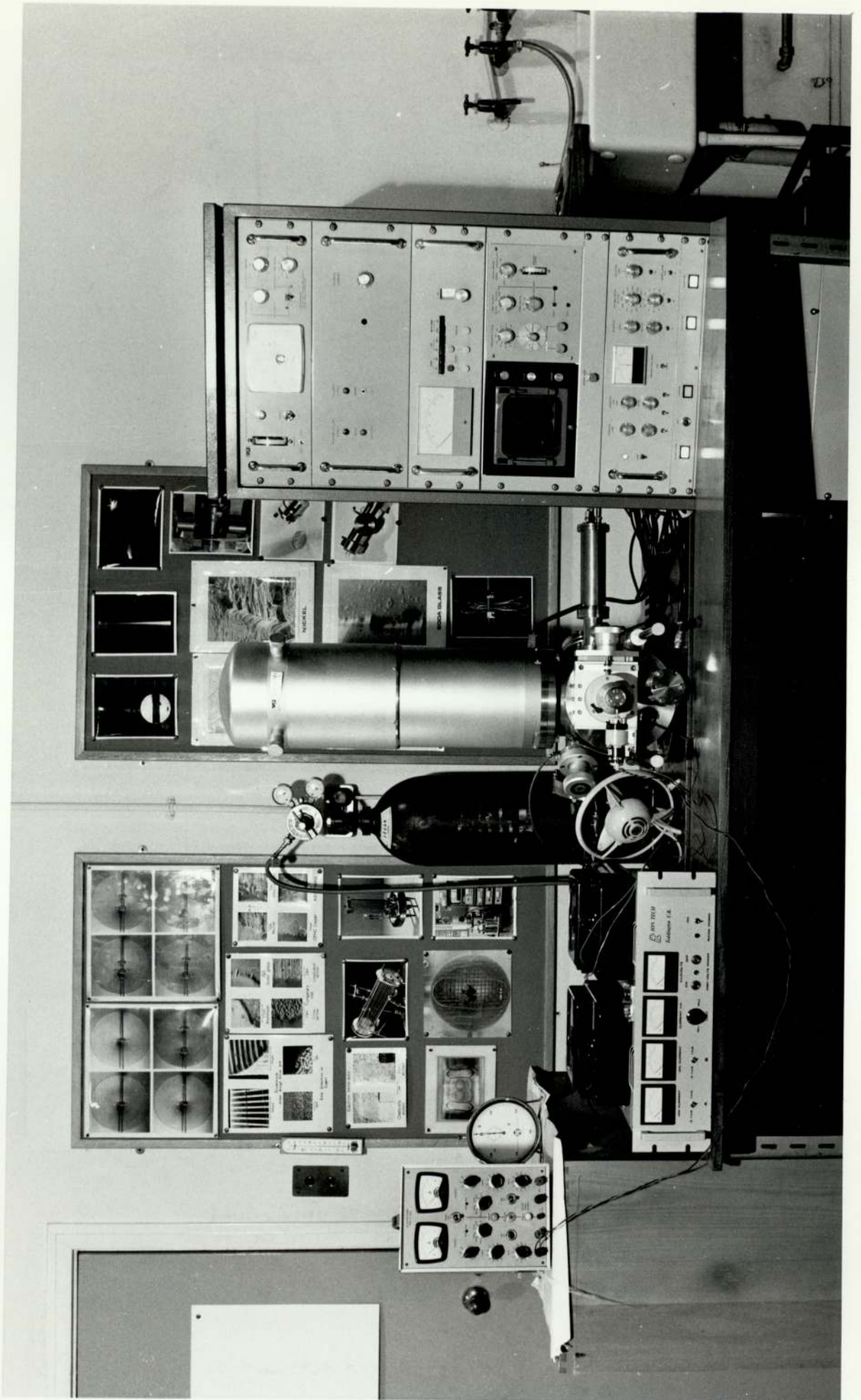
Figure 21. Electrical circuit for the ion sources.

#### 4.4 The Scanning Electron Microscope

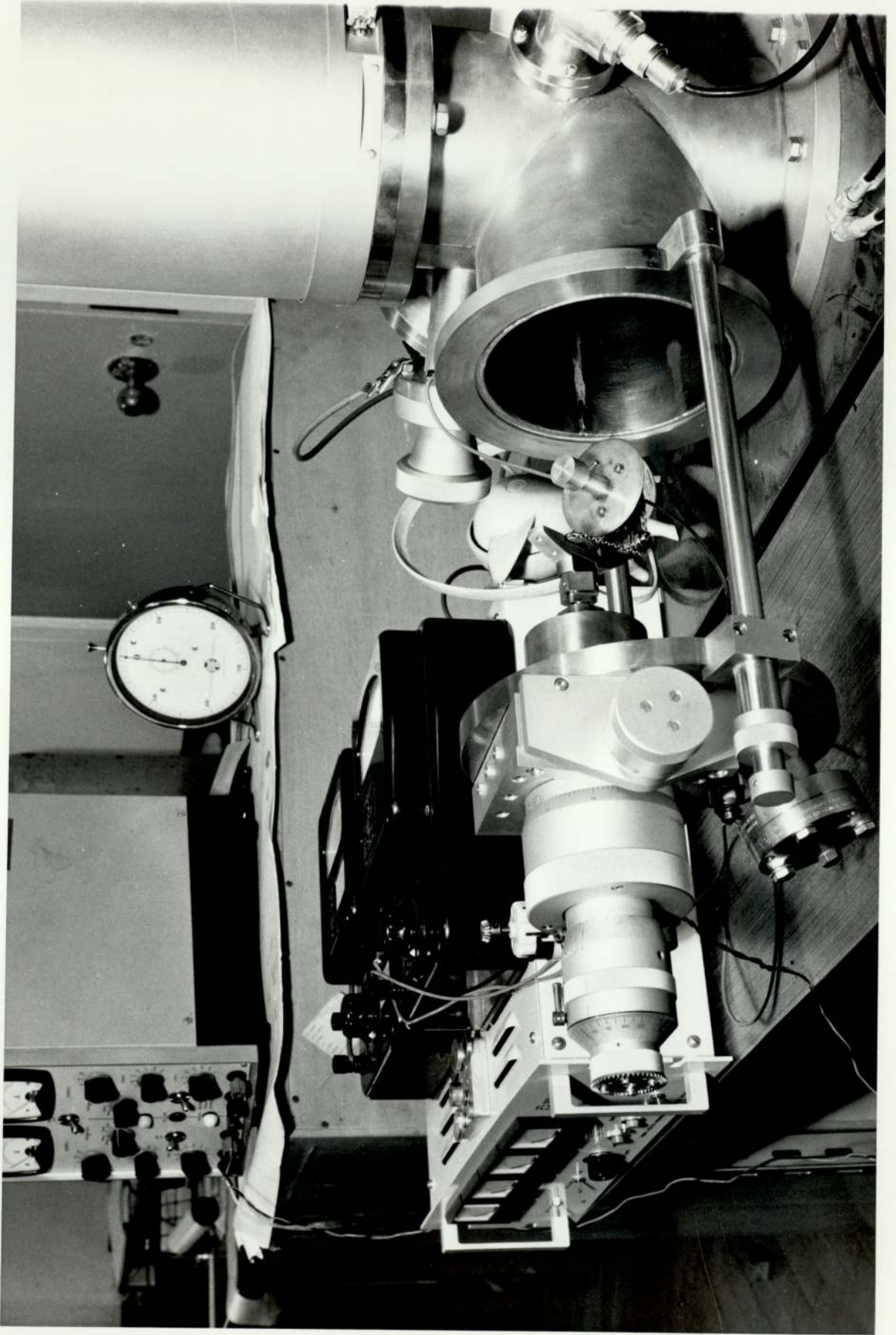
The 'Miniscan' SEM is an instrument manufactured by Vacuum Generators. The resolution is about  $500 \text{ \AA}$  and the main advantage as compared to some other microscopes is the large specimen chamber which is easily accessible. This also enables large specimens to be examined. Plate 4 shows a view of the whole instrument. The scintillator-photomultiplier system is situated on the right hand side of the goniometer stage, a closer view of which is given in plate 5. The display cathode ray tube is housed in the main console, which also contains all the various power supplies for the instrument. The flange for the ion source can just be seen on the left hand side of the goniometer stage, directly opposite the photomultiplier system.

This plate gives a complete view of the scanning electron microscope used in the investigation. The electronics rack can be seen on the right hand side of the photograph and the display screen is seen in the middle of this. The scintillator-photomultiplier assembly is seen on the right hand side of the main optical column, while the column isolation valve is situated to the left of the goniometer stage.

Plate 4. A view of the V.G. scanning electron microscope.



This plate shows the goniometer stage moved back on its rails from the specimen chamber. The various manipulating controls on the stage can be seen and also it is observed that the rotation of the specimen can be carried out by means of the outermost control. The chamber is observed to be relatively large and provides for easy access.



The main column isolation valve can be seen, just in front of the fan.

The operation of the instrument will be briefly explained. A tungsten 'V' shaped filament, heated by an ac current, is held at a negative potential of - 25 kV. Electrons emitted by the filament are accelerated towards and pass through a small hole in the anode. They are then focussed by three magnetic lenses to form a probe of diameter about  $500 \text{ \AA}$ , which is incident on the specimen. Placed above the last lens are a pair of magnetic coils which can be used to deflect the beam in 2 different directions. The specimen surface is scanned in a square raster and the size of the scan determines the magnification. The resolution is determined by the smallest diameter of the electron beam on the specimen and under these conditions the least possible area is being scanned.

The incident electron beam produces secondary electrons from the specimen surface and these are attracted by a grid at a positive potential of 200 V on to the surface of a scintillator. The surface of the scintillator is coated with a layer of about  $300 \text{ \AA}$  of aluminium which is held at 12 kV. The incoming electrons are accelerated towards the scintillator surface and produce photons of light which are incident on the photomultiplier tube. The photons produce secondary electrons at the photocathode and this current is further amplified by the remainder of the dynode chain of the photomultiplier. This current is then used to modulate the intensity of the display cathode ray tube, which is scanned in synchronism with the pair of scanning coils.

Due to the fact that there was no movement of the specimen in the Z direction provided by the goniometer stage, necessarily meant that the top of the larger specimens could not be seen. This problem

was overcome by making another pillar unit, into and on top of which the specimen stud is located, 10 mm shorter than the standard size of 31 mm. This allowed specimens up to 20 mm in height to be examined. It was possible to mount specimens up to 40 mm in diameter, although the limited traverse of  $\pm 5$  mm did not allow overall examination. The goniometer stage also allowed the sample to be inclined up to  $90^\circ$  towards the scintillator-photomultiplier and also to be rotated through  $360^\circ$ .

#### 4.5 Mounting of the Ion Sources in the Miniscan

The cylindrical and spherical sources were mounted on identical flanges, 152 mm in diameter, with the ion exit aperture at a distance of 65 mm from the specimen. This was the minimum distance away at which they could be mounted to avoid the back of the specimen stage touching the source when the specimen was inclined towards the scintillator-photomultiplier assembly. Furthermore, it was not possible to tilt the specimen such that the ion beam was incident normally on the sample, because under these conditions the back of the stage touched the scintillator-photomultiplier assembly. This restricted the minimum angle of incidence of the ion beam on to the specimen surface to  $27^\circ$ , where  $0^\circ$  refers to normal incidence. However, for large angles of incidence, there was increased sputtering of the scintillator, so that the angle of  $27^\circ$  was used throughout this investigation.

#### 4.6 Preparation of Samples

The specimens could be mounted on the smaller 13 mm diameter studs or on the larger 25 mm diameter studs. They were mounted with 'Durofix' adhesive and a dab of silver dag was usually put at one edge of the specimen to ensure that they were in good electrical contact with the earthed stud. On insulating materials, a conducting

thin film (about 500 Å thickness) of gold-palladium alloy or copper was evaporated on to the surface of the specimens.

#### 4.7 Experimental Procedure for Ion Etching

The microscope had a very fast pump-down time because the main part of the optical column could be isolated by means of the column isolation valve. Air was only let into the specimen chamber when changing samples and it was possible to evacuate this down to a pressure of  $10^{-5}$  torr in less than 2 minutes. During the etching procedure the column isolation valve was closed in order to avoid sputtered metal contaminating the optical column. With the present arrangement, simultaneous etching and viewing was not possible, however it was possible to obtain a picture within about 30 seconds of terminating the etching. Simultaneous etching and viewing was tried towards the latter part of the programme by fitting a spherical source on to the small window flange, which can just be seen in plate 4, above the scintillator-photomultiplier system.

Before commencing etching, argon gas was flushed through the specimen chamber to increase the pressure from about  $10^{-6}$  to  $10^{-4}$  torr. After some minutes the pressure was adjusted to  $2 \times 10^{-5}$  torr. The voltage was slowly increased until a discharge was obtained and then the voltage and pressure were both adjusted to give the desired operating conditions.

## CHAPTER 5

### OPERATING AND ETCHING CHARACTERISTICS OF THE ION SOURCES

#### 5.1 Introduction

This chapter is mainly concerned with the operating characteristics of the saddle field ion sources and etching rates and temperatures produced on conducting and insulating materials during ion bombardment. Comparisons between the cylindrical and spherical source have been made using both bulk specimens and thin films. Results are also presented concerning the possible contamination of specimens by material ejected from the inside of the source.

#### 5.2 Operating Characteristics

##### 5.2.1 Cylindrical Source

The characteristics of the new cylindrical source, incorporating the chimney aperture were taken with the source in the specimen chamber of the microscope. The ion beam current was measured with a copper Faraday cup of length 40 mm and diameter 25 mm, which was mounted on the normal specimen support. Figure 22 shows the variation of tube current,  $I_t$ , with tube voltage,  $V_t$ , and figure 23 shows the variation of ion beam current,  $I_b$ , with  $I_t$  for different pressures of argon. The characteristics are similar to those observed by previous workers (e.g. Ghander 1974). It can be seen from figure 23, that as the pressure increases, the ion current for a given tube current decreases. For example, for a tube current of 6 mA, the ion beam current is  $160 \mu\text{A}$  at  $2 \times 10^{-5}$  torr and only  $10 \mu\text{A}$  at  $8 \times 10^{-5}$  torr. This can be explained if we look at the

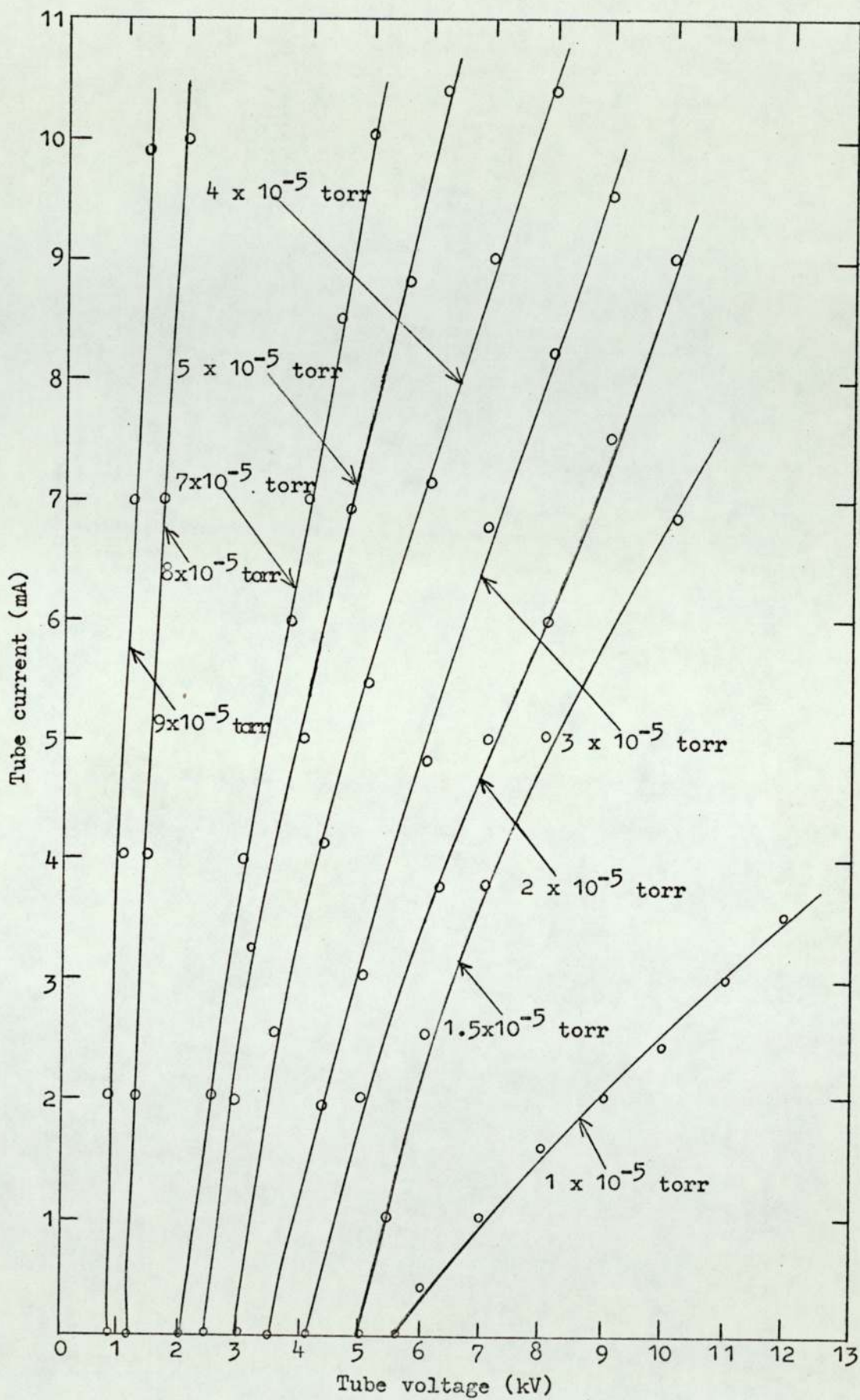


Figure 22. Variation of tube current with tube voltage for the cylindrical ion source.

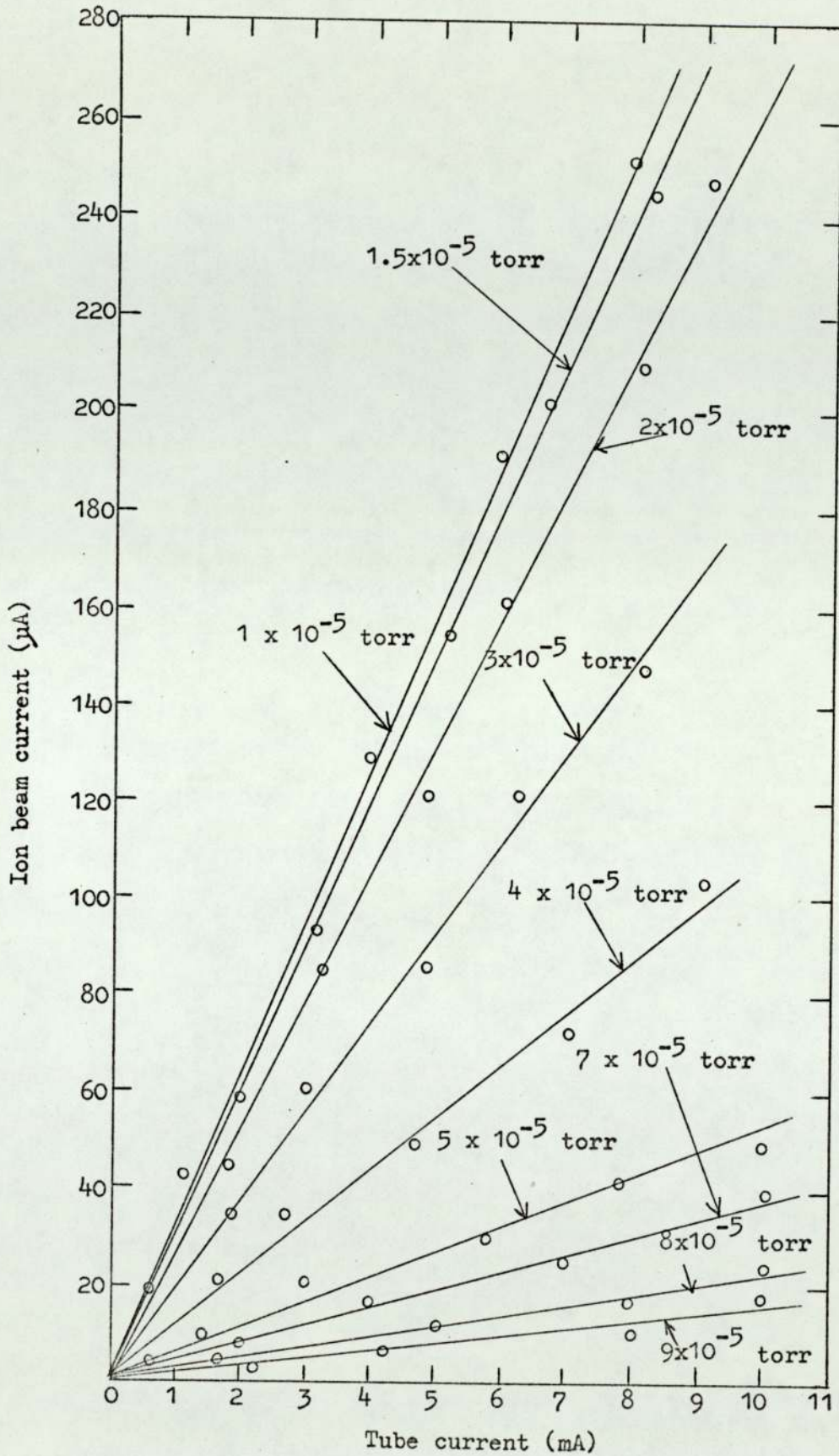


Figure 23. Variation of ion beam current with tube current for the cylindrical ion source.

variation of  $V_t$  with pressure, taken from figure 23, at a constant tube current of 6 mA. This is shown in figure 24 and the three modes

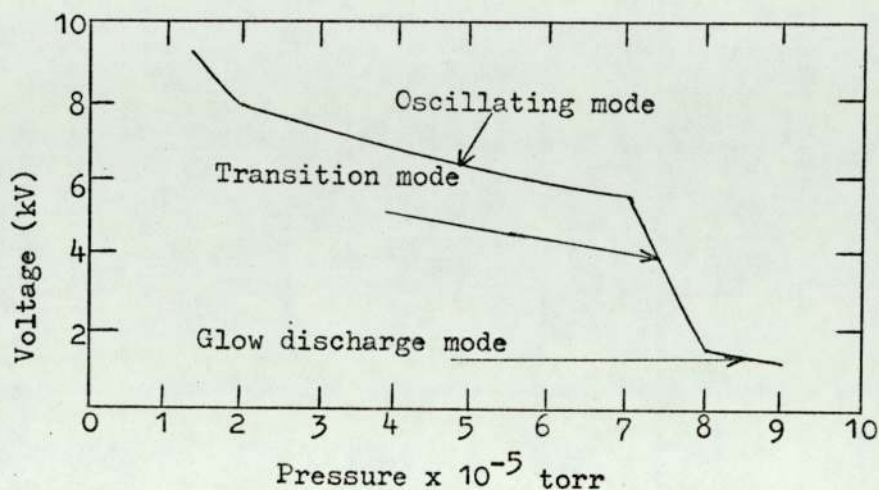


Figure 24. Showing the three modes of operation for the Cylindrical Source.

of operation, as described in section 3.3 can be seen. It is clear that the higher beam current of  $160 \mu\text{A}$  at  $2 \times 10^{-5}$  torr occurs in the very efficient oscillating mode. Thus, throughout the etching experiments the normal operating conditions were,  $V_t = 8$  kV,  $I_t = 6$  mA and  $I_b = 160 \mu\text{A}$ , at a pressure of  $2 \times 10^{-5}$  torr.

### 5.2.2 Spherical Source

The characteristics of the spherical source, taken under the same conditions as those of the cylindrical source are shown in figures 25 and 26. Figure 27 again shows the three characteristic modes of operation, taken at a tube current of 2 mA. Therefore, throughout the etching experiments, the normal operating conditions

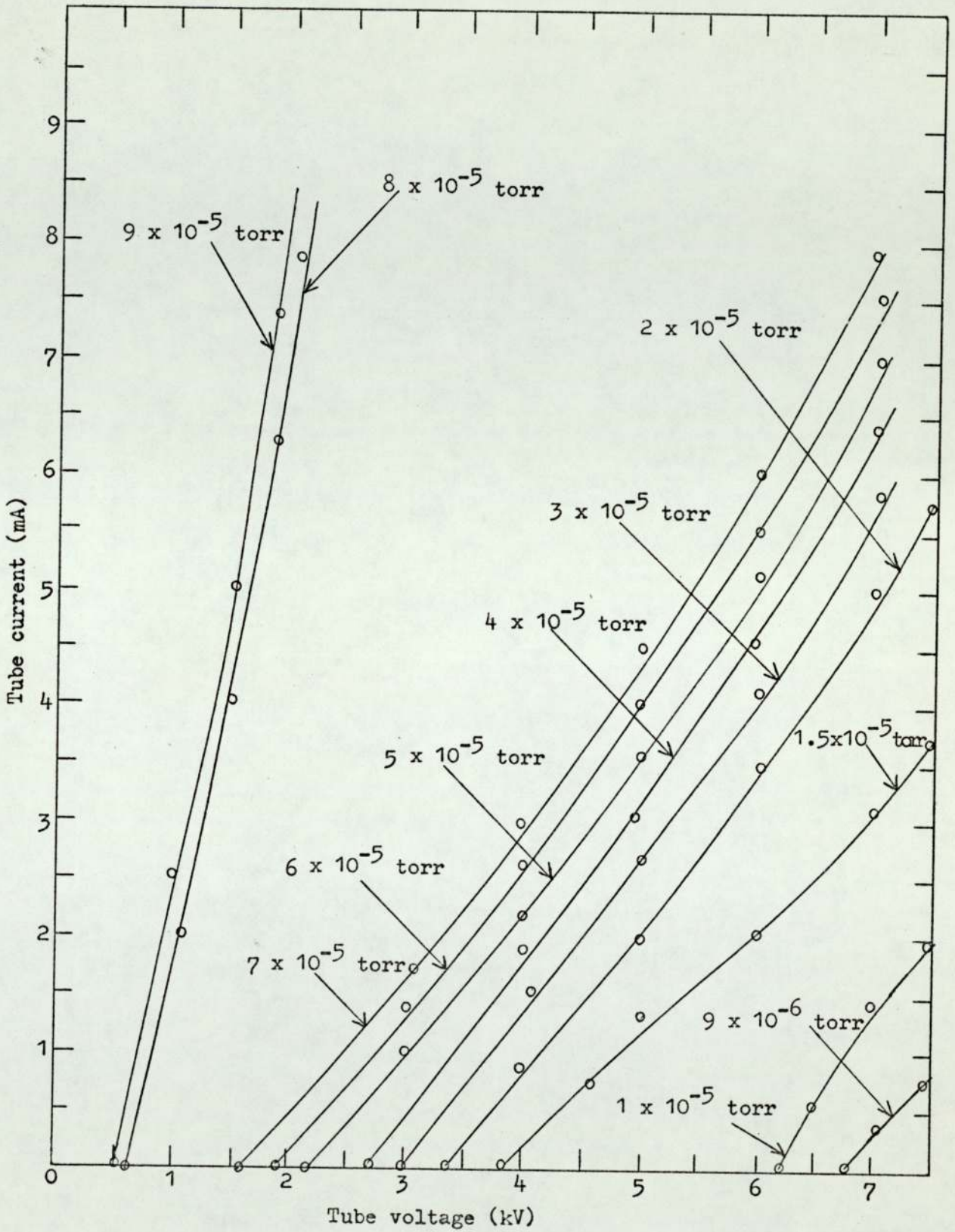


Figure 25. Variation of tube current with tube voltage for the spherical ion source.

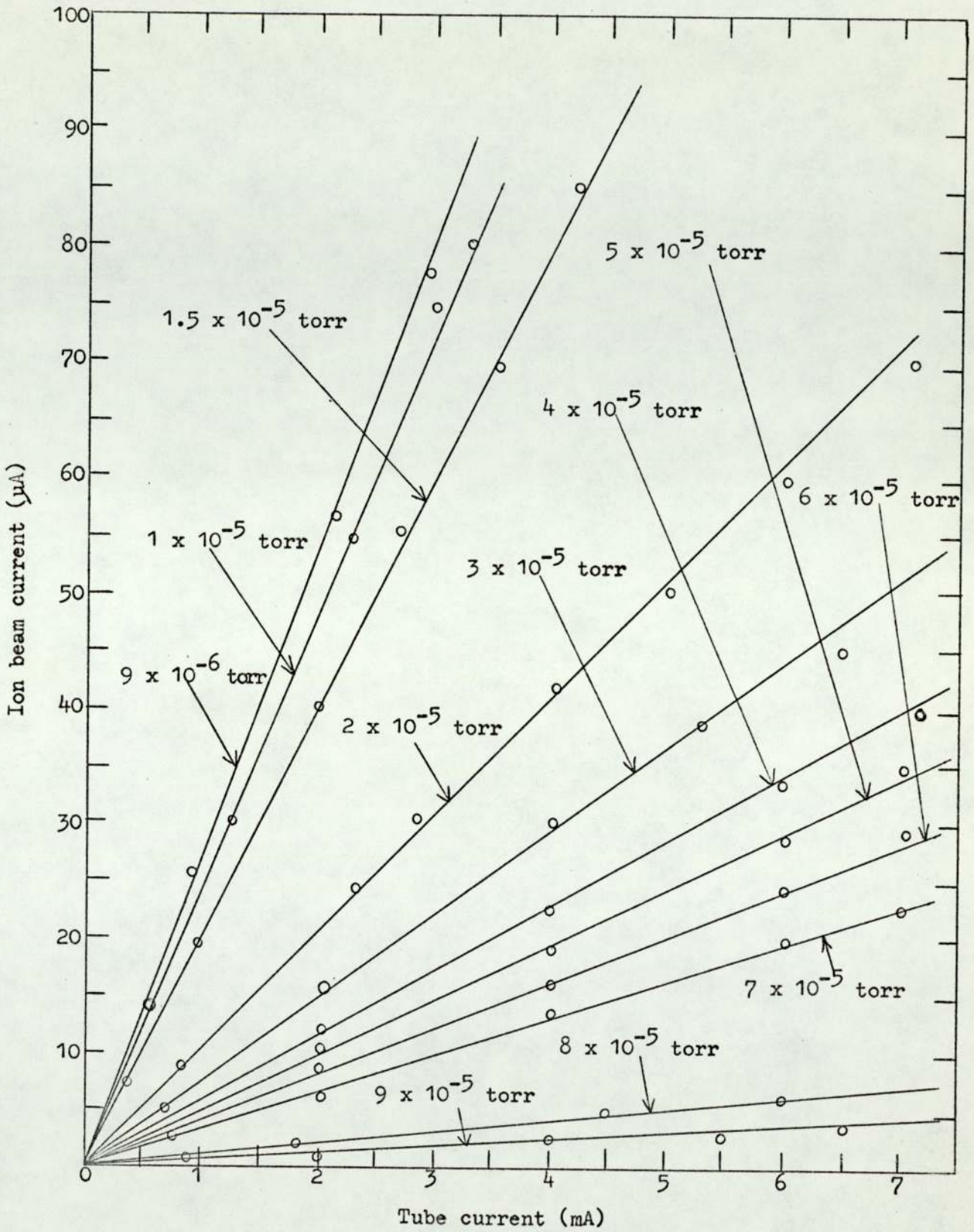


Figure 26. Variation of ion beam current with tube current for the spherical ion source.

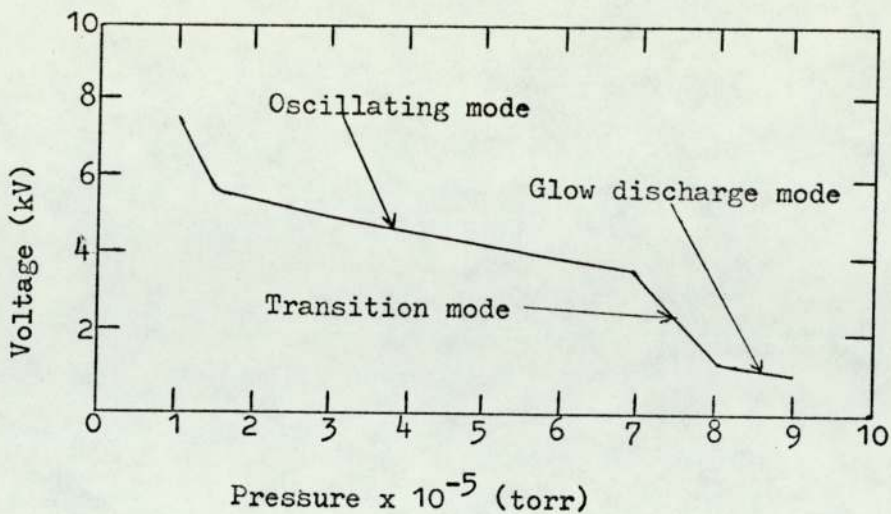


Figure 27. Showing the three modes of operation for the spherical source.

were,  $V_t = 6$  kV,  $I_t = 2$  mA and  $I_b = 40 \mu\text{A}$  at a pressure of  $1.5 \times 10^{-5}$  torr, unless otherwise stated.

### 5.3 Etching Rates

#### 5.3.1 Bulk Copper Specimens

Two specimens of OFHC copper (10 mm x 10 mm x 1 mm) were polished using various grades of abrasive, finally with  $1 \mu\text{m}$  diamond paste. Half of each specimen was then covered with aluminium foil and one was etched in the microscope for 3 hours with the cylindrical source, operating at the normal settings. The second specimen was similarly etched with the spherical source for the same time, again operating at the normal settings. The shielding foil was then removed and micrographs of the specimens were taken. Plate 6(a) and 6(b) shows micrographs taken after etching with the cylindrical and

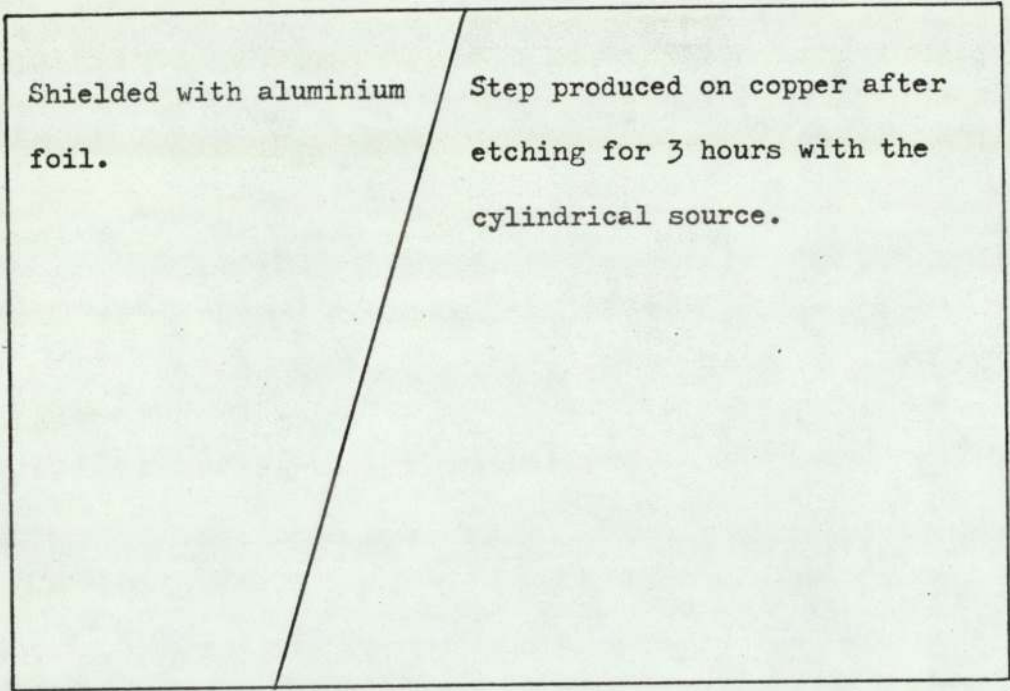
spherical source respectively, with an angle of  $30^\circ$  between the specimen surface and the electron beam. The magnification in plate 6(a) is 2000X, whereas in 6(b) it is 1000X. Both micrographs show the step produced between the intensely etched region and the shielded region. The etching rates were estimated from the step as  $5 \mu\text{m/hr}$  and  $10 \mu\text{m/hr}$  with the cylindrical and spherical sources respectively.

### 5.3.2 Ion Source Cathode

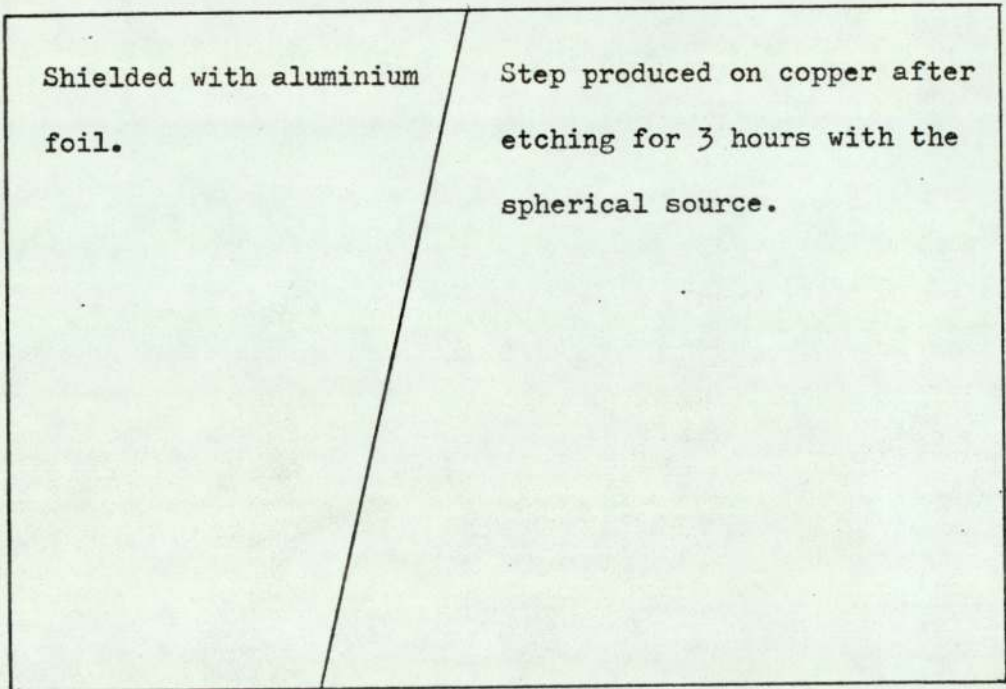
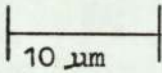
The cylindrical source described in section 4.1 was used for a total of about 160 hours at the normal settings, which have been used on all the experiments. It was found that on dismantling the source, that a very small diamond shaped hole had been produced on the lower surface of the cylinder, opposite the chimney ion exit aperture, corresponding to the intense central region referred to in section 3.3. Since the thickness of the stainless steel cylinder was 1.6 mm and the source had been dismantled after 130 hours use when the hole was not observed, it was estimated that the hole started to be formed after a total use of about 140 hours. From this data it was estimated that in the intense region, the cathode surface was etched at a rate of about  $11 \mu\text{m/hr}$ . This figure is very unlikely to be in error by more than  $\pm 2 \mu\text{m}$ .

### 5.3.3 Evaporated Copper Films

A new cylindrical ion source was made which was exactly the same as the one described in section 4.1, except that two apertures 1.5 mm in diameter were employed without chimneys, diametrically opposite one another, as in the spherical source. An aluminium Faraday cup mounted 10 mm away from the lower aperture could be used to continuously monitor the beam current. The object of the experiments in this section was to make a much better comparison



(a)



(b)

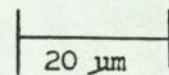
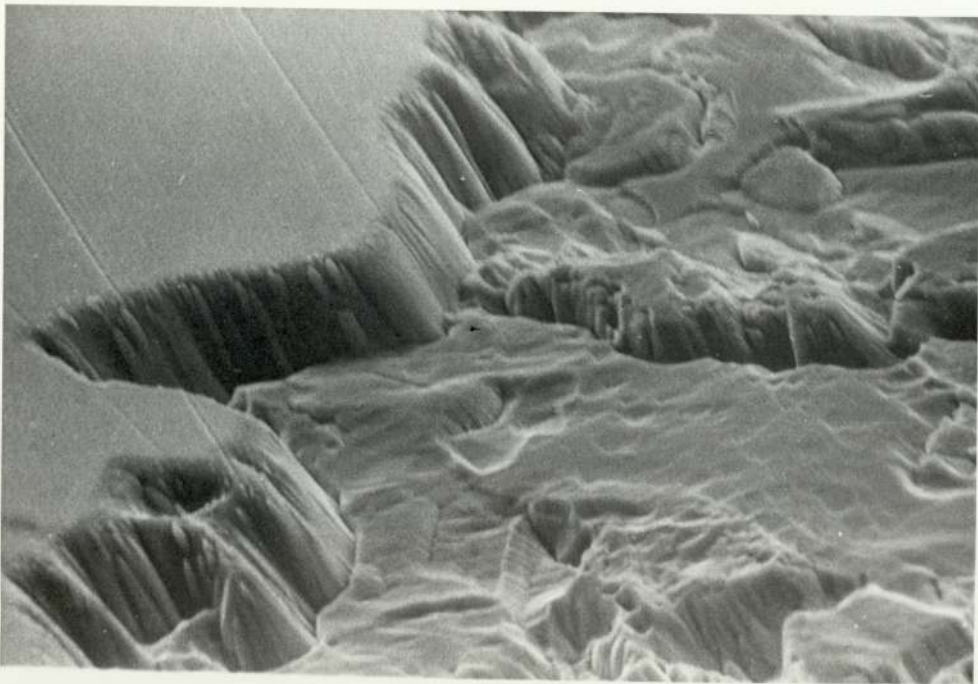
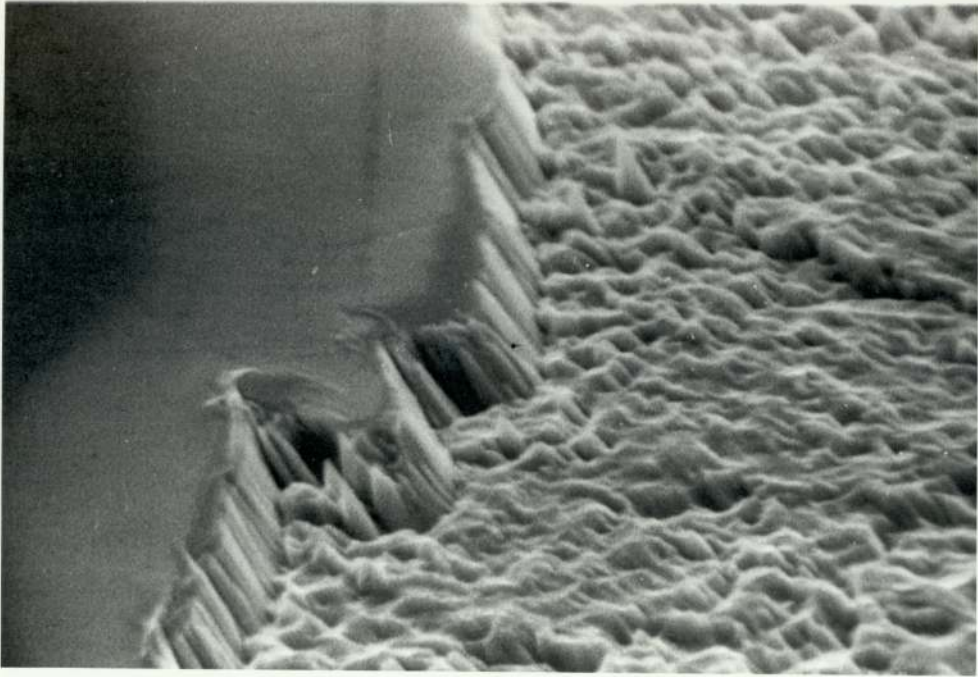


Plate 6. Micrographs of the steps produced after etching with the cylindrical and spherical sources.



between the cylindrical source and the spherical source about etching rates and beam divergence. It was decided to fix the beam current, the tube voltage and also to operate the two sources at about the same pressure. The only parameter that would be different would be the tube current. The beam current was fixed at  $15 \mu\text{A}$  and the tube voltage at  $7 \text{ kV}$ . For the newly constructed cylindrical source, it was found that to give these settings a tube current of  $4.2 \text{ mA}$  at a pressure of  $8.5 \times 10^{-6} \text{ torr}$  had to be used. On the other hand, the spherical source required to be operated with a tube current of  $0.5 \text{ mA}$  at a pressure of  $9 \times 10^{-6} \text{ torr}$ .

A problem was encountered when changing from one source to the other. The alignment was found to be occasionally affected and the centre of the etched region did not always coincide with the centre of the specimen stud. This problem was overcome by changing the position of the source fractionally in its mounting on the flange until centralisation was obtained, the latter being checked by bombarding for 10 to 15 minutes, the larger polished specimen studs coated with a copper film of about  $1000 \text{ \AA}$  thickness. The profile of the beam was then clearly defined, since the copper coating is quickly removed in the bombarded region. To carry out etching rate experiments, it was thus found convenient to do these on the copper coated aluminium specimen studs. Two sets of 6 studs were coated in the evaporation unit under identical conditions in order to give the same film thickness, which can be calculated from a knowledge of the distance of the specimen from the filament and the diameter and length of the copper wire. If evaporation from the filament is considered into a spherical region, with filament at the centre, then, assuming all the material is evaporated, the mass  $m$  is given by;

$$m = 4\pi R^2 t \rho \quad \dots (5.1)$$

where R is the distance of the specimen from the filament (5 cm), t is the thickness of the film and  $\rho$  is the density of copper. The volume of the copper was obtained from its diameter, 0.25 mm, and length, 45 cm. Thus,

$$m = \pi r^2 l \rho \quad \dots (5.2)$$

where r is the diameter of the copper wire and l is the length.

Substituting for m into equation (5.1), gives,

$$t = \frac{r^2 l}{4R^2}$$

$$t = \frac{(0.0125)^2 \times 45}{4 \times (5)^2} \text{ cm}$$

$$t = 7,030 \text{ \AA}$$

An estimation of the error in r, R and l indicates an uncertainty of about  $\pm 500 \text{ \AA}$ . The studs were etched at the settings given above for varying times.

A small colour photograph showing eight etched specimen studs is given in figure 28. The top four have been etched with the cylindrical source for varying times, this being 15, 30, 60 and 120 minutes. The bottom four have been etched with the spherical source, the times in this case being 15, 30, 90 and 120 minutes. The reason for the etched region being elliptical in the cylindrical source etched studs is that the beam is well collimated in the direction parallel to the cylinder axis, whereas in a direction normal to this, it is divergent, (Fitch et al 1970). However, the reason for the spherical source etched regions being slightly elliptical is because the ion beam is not normal to the specimen. This effect, which is quite small, is also present for the studs etched by the cylindrical

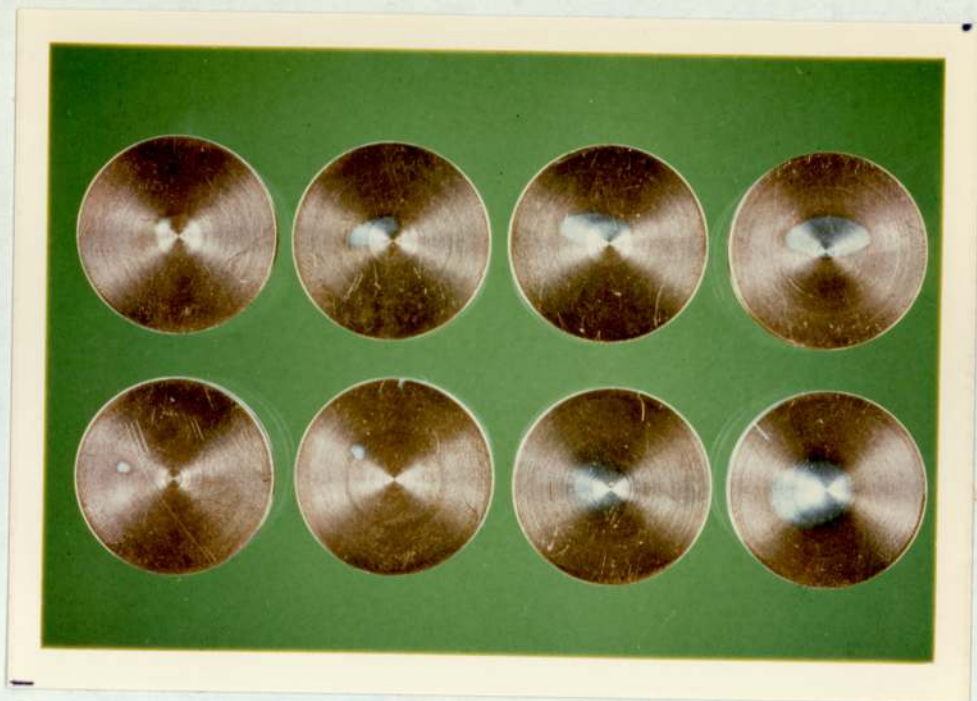


Figure 28. Showing the copper coated specimen studs etched with the cylindrical and spherical source.

source and is at right angles to the direction of the natural divergence of the beam. Figure 29 shows a plot of the minimum etching rate against distance from the centre of the etched region, where the distance used for the cylindrical source is in each case, half of the minor axis of the ellipse. To correlate with this, the distance in each case for the spherical source is half of the major axis of the ellipse. Clearly, the higher etching rate of the beam at the centre of the spherical source is demonstrated. It can be deduced from figures 28 and 29 that the intensity distribution from the cylindrical source is much more broad than that from the spherical source and also that the latter is axially symmetric, with a small intense central region. Thus, if the experiment requires uniform etching over a reasonably large area, then the cylindrical

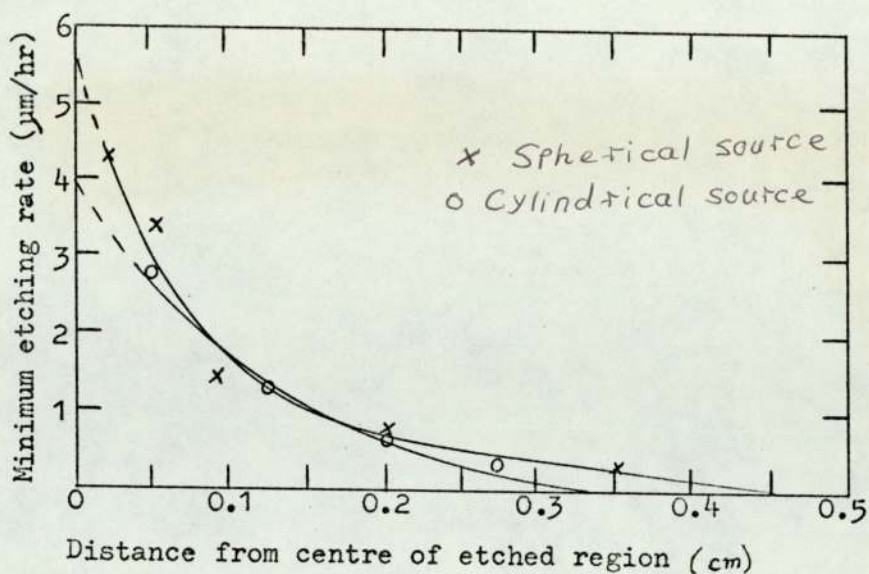


Figure 29. A plot of the minimum etching rate against distance from the centre of the etched region.

source is advantageous, whereas, if differential etching rates are required over a relatively *small* area, the spherical source is more suitable.

#### 5.4 Temperature of Materials during Ion Bombardment

##### 5.4.1 Introduction

When a material is being ion etched, its temperature increases as the energy of the ions is dissipated in the material. This is a very important point which must be considered since structural features observed in some instances may be entirely due to this effect. The rise in temperature is particularly important on, for example, low melting point plastics and soft biological specimens. Hansel et al (1972) carried out ion etching on polymeric materials, including rayon fibres, and have questioned the ability of the method for revealing true structural characteristics of the material. They

surmise that the observed structures are; (1) a product of heating by the ion beam; (2) primary bond rupture; and (3) loss of chain structure. The observed structures would then be expected to change with exposure time and severity of ion bombardment. They also thermally treated rayon fibres at  $400^{\circ}\text{C}$  and observed structural changes which were similar to those resulting from ion bombardment.

Warner et al (1975) used ion etching to reveal the structural features of organic fibres. They employed cryogenic techniques in order to keep the temperature below  $0^{\circ}\text{C}$  during etching and then compared features observed on the specimens with those observed without cooling, when the surface temperature was estimated as being about  $150^{\circ}\text{C}$ . They concluded that the ion etching technique can be usefully applied to organic fibres, provided that the thermal effects are reduced by cooling.

Werner (1974) shows by calculation that the temperature rise of specimens during ion bombardment is not significantly high. He considers a primary ion of mass 30 and energy 4 keV incident upon the target. The mean range - approximately  $100 \text{ \AA}$  - of such an ion will be traversed in about  $10^{-12}$  sec, with a corresponding average velocity in the target of  $10^4$  m/sec. If a cylindrical shaped zone of diameter and depth  $100 \text{ \AA}$  is assumed to be affected, then using calculations given by Sigmund (1974), it follows that the heat dissipated by the primary ion is carried away from this volume in about  $10^{-14}$  sec. Sigmund calculated a cascade lifetime of  $10^{-14}$  sec when initiated by 4 keV  $\text{O}_2^+$  or  $\text{Ar}^+$  ions, bombarding a Si or Fe target. If this is compared with the average rate of arrival of primary ions at a current density of  $1 \text{ mA/cm}^2$  - corresponding to the arrival of about one ion in  $10^{-4}$  sec - on the zone with  $100 \text{ \AA}$  diameter, then the following conclusions are reached. The effect of a single ion

penetrating into the target could only produce a local thermal spike in a zone of  $100 \text{ \AA}$ , within a time of about  $10^{-14}$  sec, as the following ion, on average, arrives only after a time which is large compared to the mean lifetime of one cascade. This means that effectively the cascades which are generated by the individual ions are independent of each other and no macroscopic temperature rise occurs.

This thermal spike phenomenon has been shown to occur by Thompson and Nelson (1962) in their studies on single crystals of gold, bombarded by 43 keV  $\text{Ar}^+$  and  $\text{Xe}^+$  ions. They found that the results could only be explained if a spike temperature of  $1000^\circ\text{C}$  higher than the target, lasting for about  $10^{-12}$  sec was assumed. Further confirmation of this effect has been provided by the work of Nelson (1965), who observed the variation of sputtering yields with temperature in polycrystalline targets bombarded with 45 keV noble gas ions. He found that his very high yield measurements could only be explained if evaporation from a small hot zone created by the primary, in the target material was considered. The results indicated spike radii of about  $100 \text{ \AA}$  and temperature rises within these spikes of up to  $1000^\circ\text{C}$  for periods between  $10^{-11}$  and  $10^{-12}$  sec.

#### 5.4.2 Temperature Measurement of Various Materials

For the present work, copper constantan thermocouples were employed in order to measure the temperature of insulating and conducting specimens while they were being ion etched in the microscope. The thermocouple leads were taken in to the specimen chamber via the flange which is seen on the lower part of the goniometer stage in plate 4. The reference junction of the thermocouple was kept in ice-water at  $0^\circ\text{C}$ . In order to substantiate that the temperature as measured with the thermocouples was the actual surface temperature,

known low melting point alloys were used as specimens. The melting point of these alloys was also checked by suspending the alloy in a temperature controlled bath of water.

(a) Low Melting Point Alloys

A thermocouple was embedded between a large specimen stud and a glass sheet, 30 mm square by 2.75 mm thick, in order to simulate the bombardment conditions experienced by some of the insulating specimens, examined in the latter part of the work. The glass sheet was mounted on the stud using Durofix and silver dag. A second thermocouple was embedded into a sample of 'Cerrobend alloy', (10 mm x 10 mm x 2 mm), by melting the latter in hot water. The specimen was then mounted on to the glass sheet and the stud was set in position in the stage of the microscope. A nickel sheet was suspended from the specimen mount in such a position that when the specimen melted due to ion bombardment, it was collected on this sheet.

The sample was then bombarded using the spherical source, operating at the normal settings of an anode voltage of 6 kV, a discharge current of 2 mA, at a pressure of  $1.5 \times 10^{-5}$  torr. Under these conditions the ion beam current is  $40 \mu\text{A}$ . The ion beam was found not to affect the thermocouple in any way so that it could be continuously monitored on the potentiometer unit which had provision for two thermocouples. The temperature was inferred from standard tables for a copper-constantan thermocouple. The Cerrobend sample was bombarded for a total of 8 hours and on examining it was found not to have melted. The graph of figure 30 shows the rate of rise of temperature of this sample and it can be seen that the maximum temperature reached was  $60^{\circ}\text{C}$ .

A specimen of the 'Cerro 117' alloy, melting point  $47.5^{\circ}\text{C}$ , was mounted in the same way as the previous sample. This was again

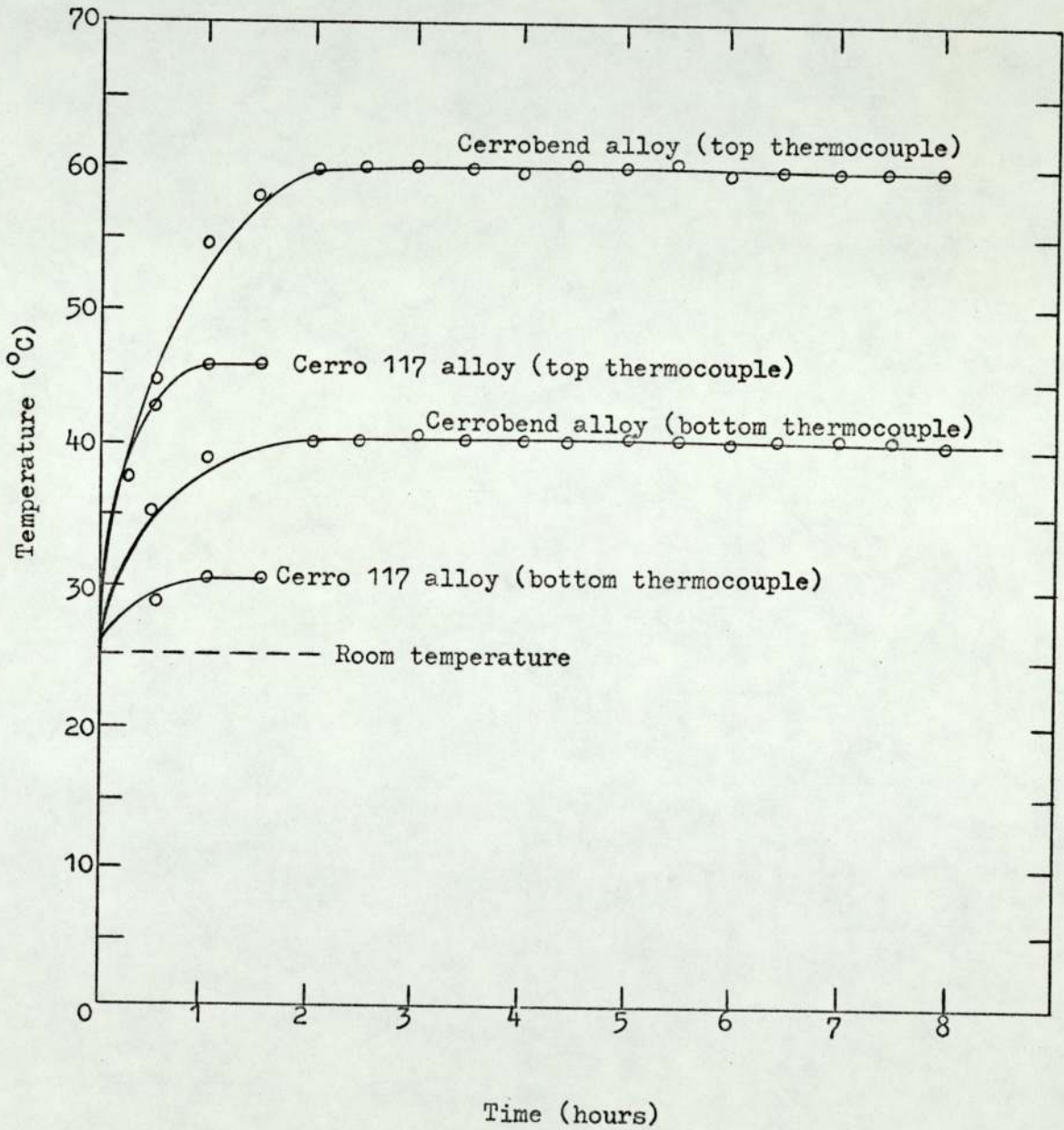


Figure 30. Rate of rise of temperature of Cerrobend and Cerro 117 alloys using the spherical ion source.

bombarded with the spherical source for 1.5 hours using the same operating settings. From the graph in figure 30 it can be seen that the maximum temperature as recorded by the thermocouple embedded into the sample was  $46^{\circ}\text{C}$ . This sample was found to have melted, more than half having dripped on to the nickel collecting sheet. The observed melting point obtained with the thermocouple is in reasonable agreement with that of  $47.5^{\circ}\text{C}$ , given by the manufacturers.

Further experiments were carried out in which the 'Cerrobend alloy' was mounted directly on to the specimen stud. The second thermocouple was glued on to the bottom of the specimen stud. This sample was bombarded with the cylindrical source using the normal settings of 8 kV, 6 mA at a pressure of  $2 \times 10^{-5}$  torr. The ion beam current given by these settings being  $160 \mu\text{A}$ . The graph is shown in figure 31 and it can be seen that the maximum temperature reached was  $68^{\circ}\text{C}$ . This specimen upon examination was also seen to have melted and most of it had dripped on to the collecting sheet. As expected, no significant difference was observed between the thermocouple in the sample and the other underneath the stud. A sample of the 'Cerro 117' was then mounted in a similar manner to the previous sample and this was bombarded with the spherical source for 6.5 hours. The maximum temperature can be seen to be  $43^{\circ}\text{C}$  from the graph in figure 31 and this specimen was found not to have melted.

The above experiments indicate that the temperature, as measured by the thermocouples, is a true surface temperature so that further measurements on conducting specimens could be carried out with some confidence. It must however be mentioned that results were also obtained on insulating specimens, but no experiments were undertaken to substantiate beyond doubt that these measurements were giving the true *sample* temperatures of these materials.

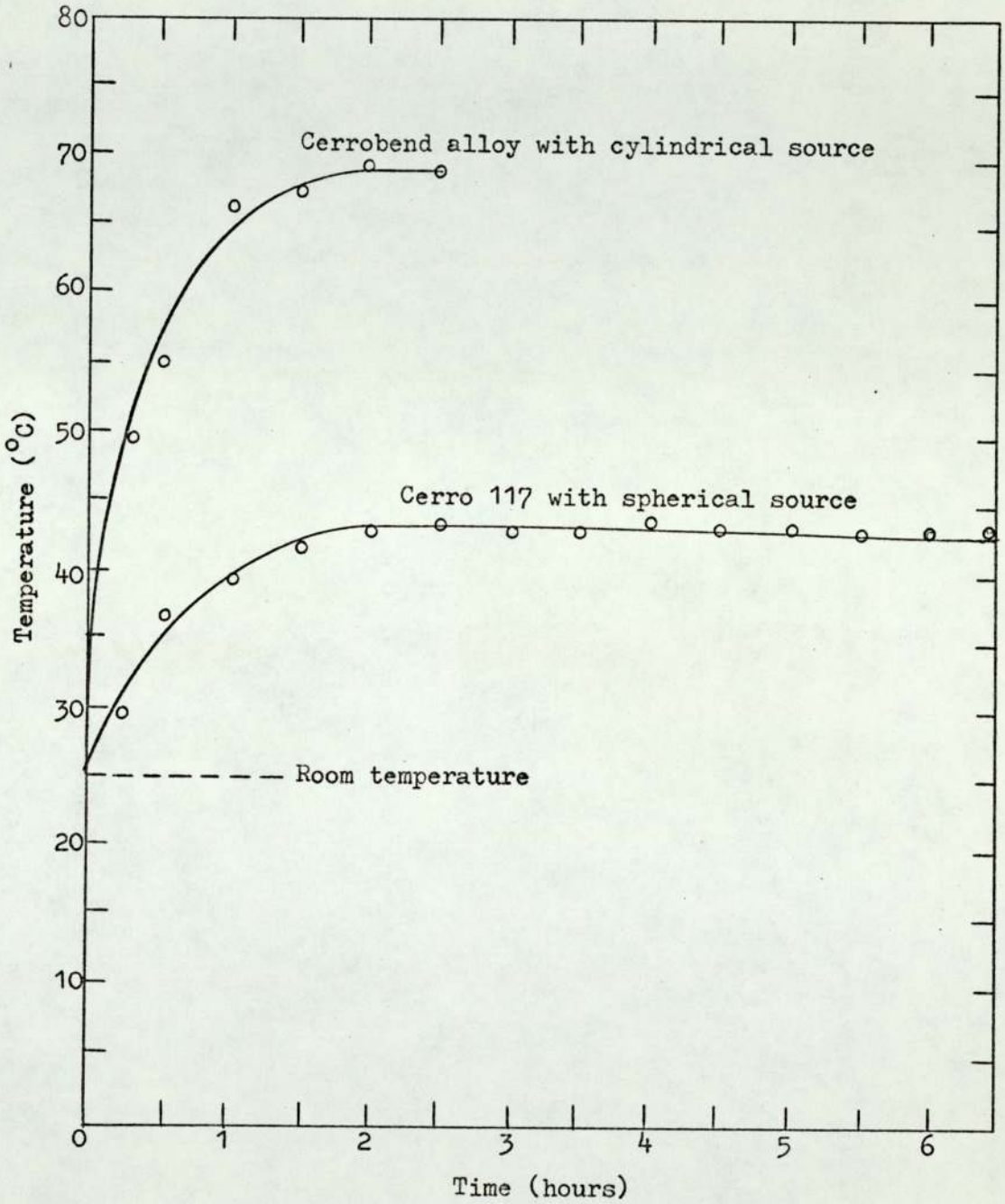


Figure 31. Rate of rise of temperature for Cerrobend and Cerro 117 alloys with the cylindrical and spherical ion sources respectively.

(b) O.F.H.C. Copper

A sample of polished O.F.H.C. copper, (10 mm x 10 mm x 1 mm), with a thermocouple fixed on the centre of each face, was mounted on to a specimen stud and bombarded with the cylindrical source for 12.5 hours using the normal conditions. After cooling to room temperature, the same sample was then bombarded with the spherical source. The graphs of temperature against time are given in figure 32 and it can be seen that with the cylindrical source, the maximum temperature reached was  $73^{\circ}\text{C}$ , while with the spherical source it was  $41^{\circ}\text{C}$ . The two thermocouples, the one on the bottom face of the copper and the other on the top face which was being bombarded, showed that there was no significant difference in the temperature of these two faces.

(c) Dental Tissues

It has been mentioned in the abstract that a great deal of work was carried out on dental tissues, so that a tooth was chosen as an insulating specimen. A small hole was drilled into the side of a 10 mm high crown tooth, 1 mm from the top. A thermocouple was stuck on to the top with Durofix and a second one was planted into the hole. The tooth was mounted on a specimen stud with durofix and silver dag and then it was bombarded with the cylindrical source using the normal conditions for 14 hours. After allowing the specimen to cool to room temperature, it was then bombarded with the spherical source for the same time. The graphs of temperature against time are shown in figure 33 for both experiments and it can be seen that the maximum temperature as recorded by the thermocouple on the top surface of the tooth was  $137^{\circ}\text{C}$  and  $80^{\circ}\text{C}$  for the cylindrical and spherical source respectively.

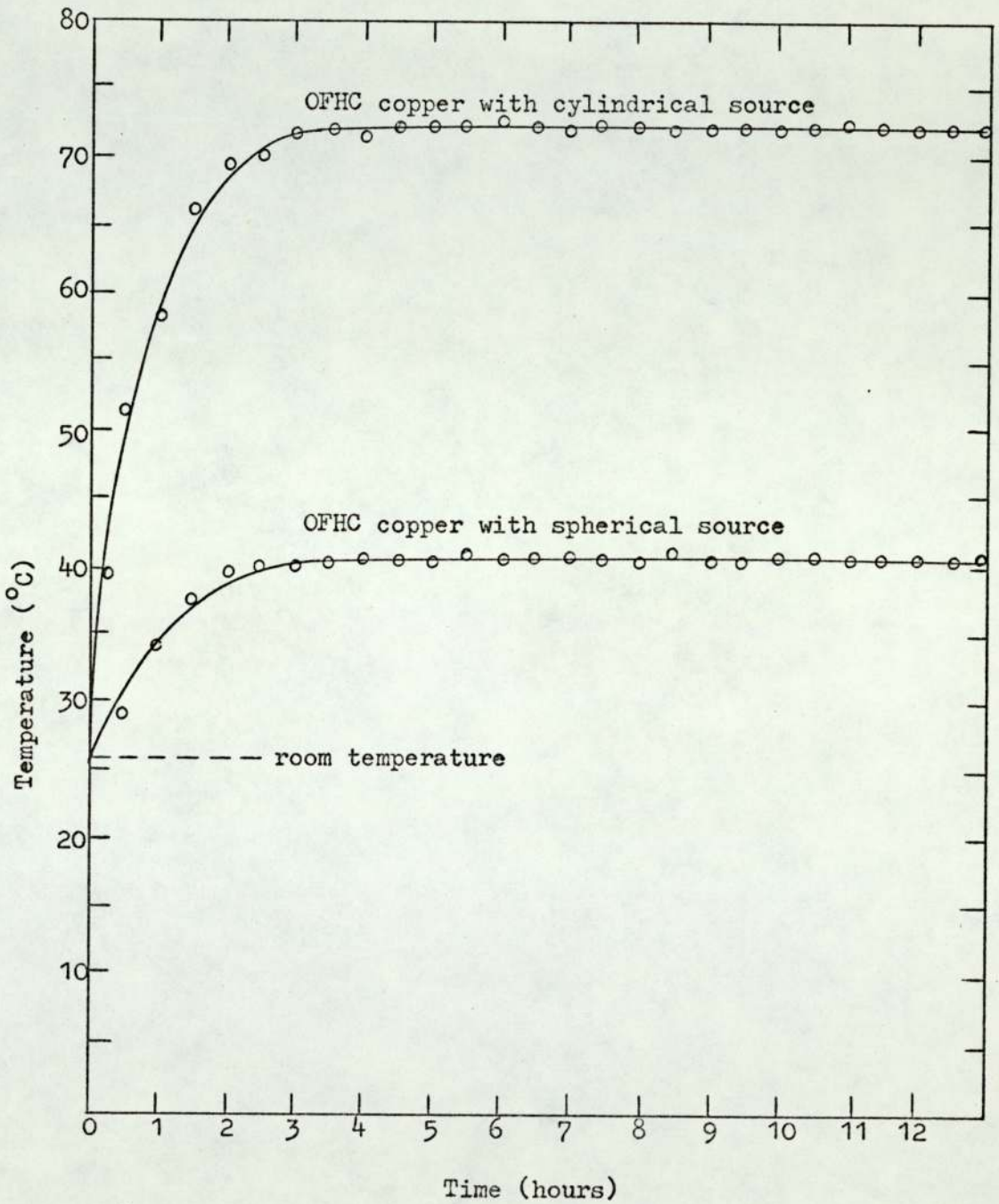


Figure 32. Rate of rise of temperature of OFHC copper with both the cylindrical and spherical ion sources.

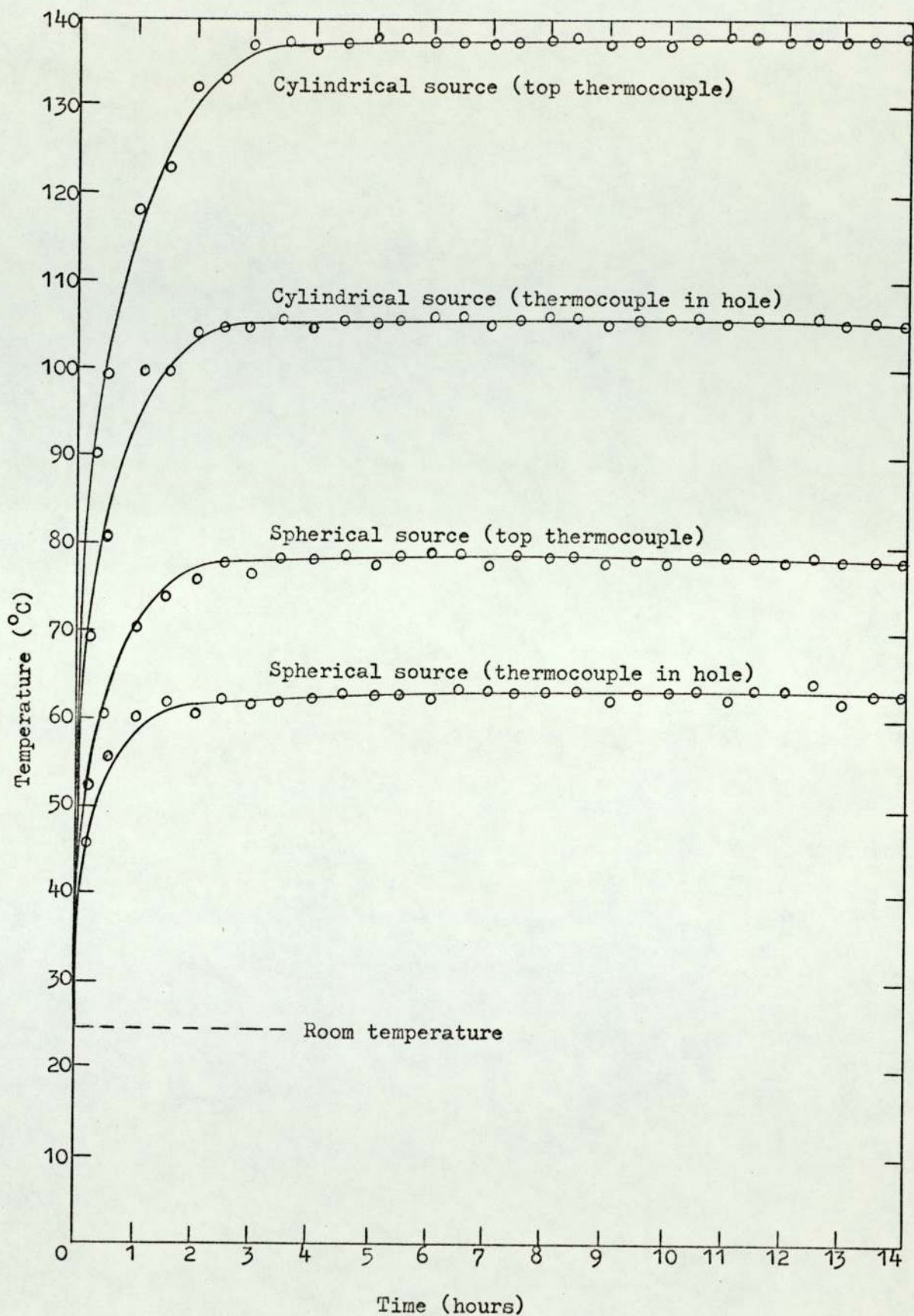


Figure 33. Temperature measurements of a tooth using the cylindrical and spherical ion sources.

### 5.4.3 Discussion

The measurements clearly indicate that any temperature rise is unlikely to be a problem on most conducting specimens with either of the sources. On the other hand for non-conducting specimens, problems may occur on materials which are affected at temperatures above about 140°C and 80°C with the cylindrical and spherical sources respectively and this should be borne in mind when interpreting the results. However, the measurements have shown that the spherical source is somewhat more suitable for these materials. It is appreciated that the temperatures would be considerably less if the sources were operated at lower voltage and beam current, but then the pressure would have to be increased appreciably. Alternatively, the size of the aperture could be reduced to maintain the same chamber pressure, in order to increase the source pressure and thus operate at a lower beam power. This was not attempted in the present work but is feasible if the nature of the material demands that it is maintained at a constantly lower temperature during etching. Some results presented in Chapter 7 suggest that the observed surface topography may be a result of thermal effects and that extreme care must be taken in their interpretation.

### 5.5 Chemical Analysis of an Ion Bombarded Sample of Copper using Electron Spectroscopy

There has been considerable reference, (Sixth International Vacuum Congress, 1974), concerning the possibility of contamination of specimen during etching by material from the inside of the source. This would be in the form of ferrous, chromium, nickel and other additives of the stainless steel in the case of the cylindrical source. For the spherical source, this would be expected to be mainly aluminium or impurities contained in the aluminium. If any

material is ejected from the inside of the sources, as neutral atoms or ions, then it would be expected to lie fairly superficially on the specimen undergoing bombardment, probably within the first 100 Å or so. In order to detect whether any impurities are being implanted into the etched specimens, an analysis of several specimens was made using an instrument known as ESCA, (electron spectroscopy for chemical analysis), manufactured by Vacuum Generators. Basically the operation of this instrument depends upon the detection of photoelectrons of characteristic energies from the sample under investigation. The element giving rise to the electrons can thus be identified.

For the analysis, 3 samples of high purity copper foil, 130  $\mu\text{m}$  thick were prepared. Two of these were etched, one with the cylindrical source with the 2 apertures and the second one with the spherical source, using the settings mentioned in 5.3.3, where the tube voltage and ion beam current were kept constant at 7 kV and 15  $\mu\text{A}$  for both sources. The samples were etched for the same time, this being 6 hours. The third copper specimen was kept as a control and was not etched. All three samples in turn were then examined in the ESCA instrument which operated at a pressure of about  $10^{-10}$  torr. Two spectrums for each sample were taken, the second one being taken after 30 seconds in situ bombardment with 6 keV argon ions at a low pressure. The object of this procedure was to remove any adsorbed surface impurities.

The spectrums of the two etched specimens and the control were found to be identical and one is shown in figure 34. The peaks show the presence of copper, oxygen, carbon and nitrogen. After the 30 second etch, the peaks due to carbon, oxygen and nitrogen are reduced while the copper peaks were enhanced and this is shown in figure 35. The reduction of peaks other than copper suggests that these elements exist as an adsorbed impurity. The removal of surface impurities

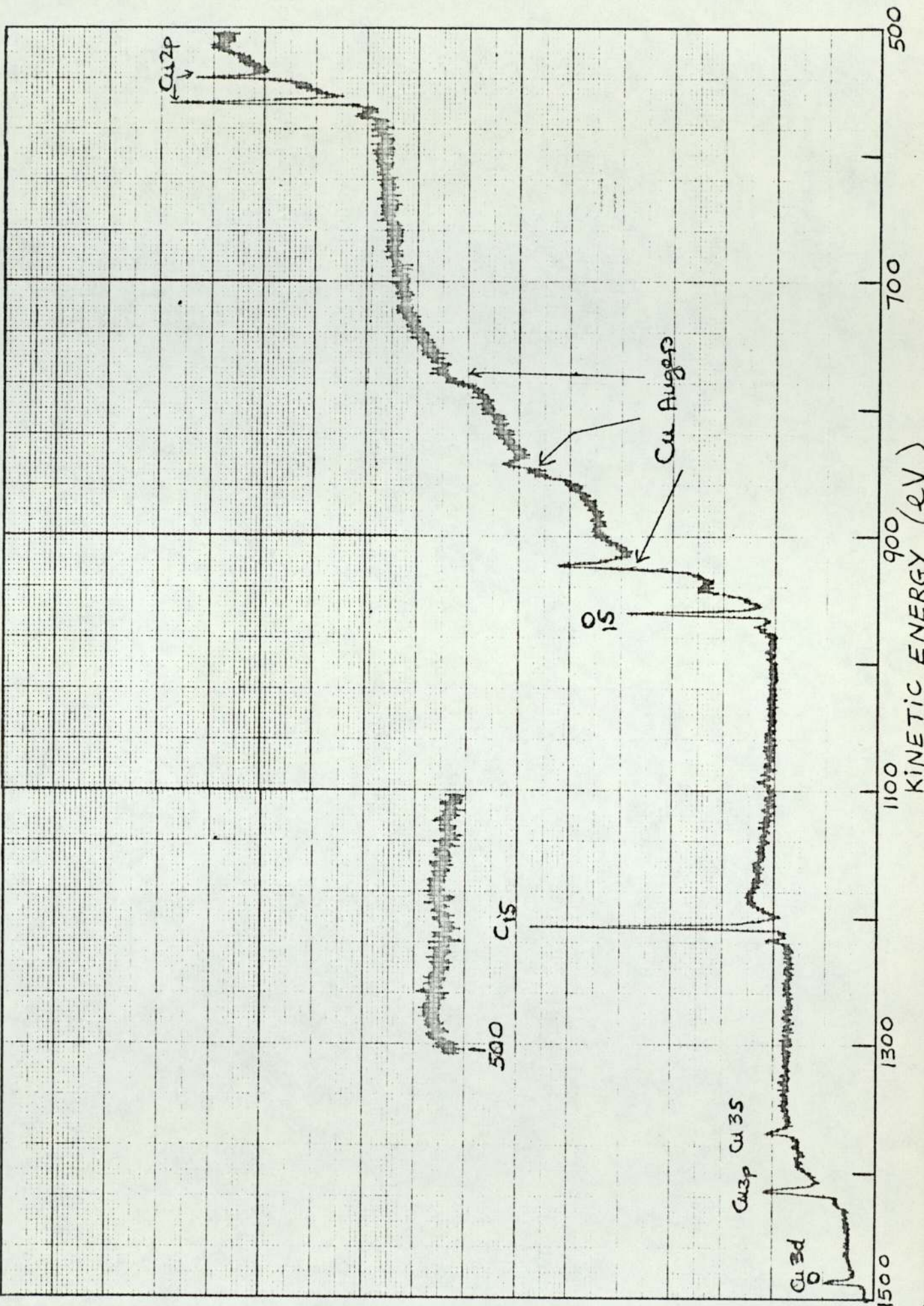


Figure 34. ESCA analysis spectrum of an ion bombarded specimen using the spherical ion source.

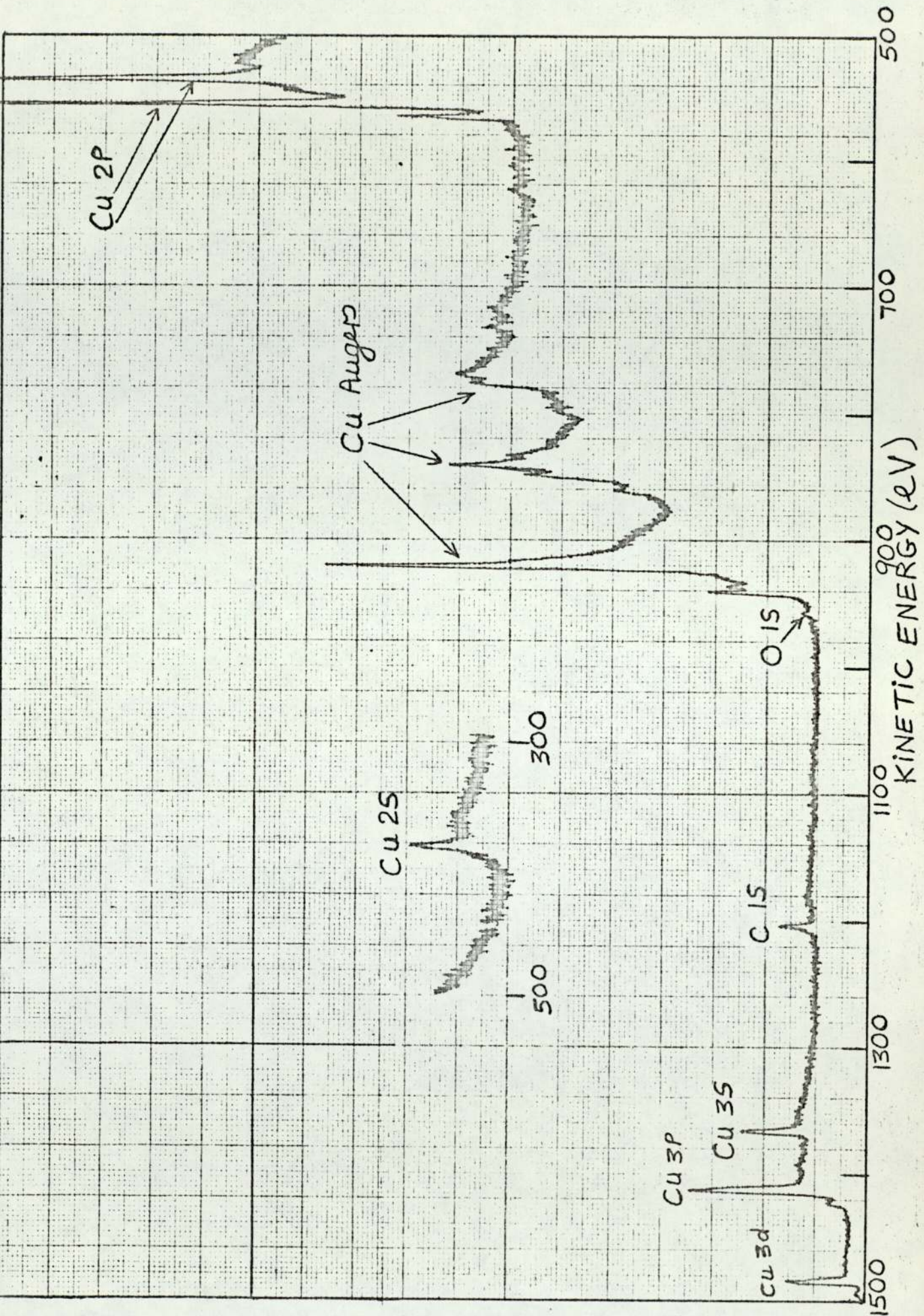


Figure 35. ESCA analysis spectrum after removing adsorbed layers.

by etching is clearly shown, due to the appearance of the copper 2S photoelectron peak in figure 35, which has an escape depth of only a few Å. It would appear from this preliminary analysis that the surfaces of the bombarded specimens are generally free of implanted impurities to within the limit of detection by ESCA, (about 1%). A more detailed analysis could be performed by high resolution scans in the region of Ni, Fe, Cr and Al photoelectron energies. However, because of the identical spectrums obtained for bombarded and reference specimens it was considered that high resolution scans would not improve much on the present analysis.

## 5.6 Discussion

The temperature measurements have indicated that under operating conditions, which for the purpose of this work, have been defined as normal, the cylindrical and spherical source can be used to ion etch most materials, which are not thermally affected at temperatures below about 140°C and 80°C respectively. Clearly, if necessary, the temperature rise of the specimens could be considerably reduced using cryogenic techniques. The etching rate on bulk copper specimens, in the intensely etched region, has been shown to be about 5 μm/hr with the cylindrical source and about 10 μm/hr with the spherical source. Also specimens etched by either of the sources have been shown to be free from implanted impurity.

The point has been reached in this thesis where all preliminary work necessary for ion etching has been completed and the next stage is the in situ observation of surface structure of different types of materials. However, before this study can commence and be critically appreciated, it is important to consider the artefacts which can be produced. A study of the surface structures resulting from ion etching is given in Chapter 6 and this is followed in the next

chapter on the work that was carried out to investigate the value of ion etching as a technique for revealing structure of a variety of different materials.

CHAPTER 6

ARTEFACTUAL STRUCTURES ARISING FROM ION ETCHING

6.1 Introduction

In some instances, the structural features observed on ion bombarded surfaces may not be characteristic of the material but are due to artefacts. It is important to be able to recognise these so that a true interpretation of the results can be made. Generally, the materials being examined produce a definite repeating pattern after etching, whereas the artefactual structures are quite irregular and this helps the interpretation considerably. However, in rare instances, especially on insulating materials, the surface topography, although artefactual, has such an appearance that it is very difficult to tell that it is not characteristic of the material being etched. Under these circumstances, it is advisable to change such parameters as the angle of incidence of the beam, rotate the specimen during etching and if thermal effects are suspected, to use cryogenic techniques. One of the easily recognisable features and the most studied, is the appearance of cone like structures on ion bombarded materials. The author has also made a study of these cones on different materials and has observed some new types of structures which, to his knowledge, are not reported elsewhere in the literature.

The formation of sub-microscopic cones on ion bombarded surfaces was first reported by Guntherschulze and Tollmein (1942), using an optical microscope. They observed the phenomenon on a number of different metals and noted that the cone apex angle was different for each metal. Wehner (1955) observed the formation of similar

structures on silver and attributed the growth to the migration of condensed metal atoms on the cathode surface. Stewart (1962) employing an in-situ ion etching technique, as in this investigation, but with an rf source and a highly complex pumping system, observed cones on tungsten. The formation of these was postulated as being either due to inclusions with a lower sputtering coefficient than the matrix, or by particles resting on the surface. These low yield particles shielded the matrix producing a protrusion, which with continued etching was fashioned into a cone and when the shielding particle was completely eroded away, a cone of matrix material remained.

Stewart and Thompson (1969) observed the formation of cone type structures on tin and silicon crystals and these workers also gave the first theoretical model about their formation. Some of the well established theoretical considerations will be discussed in the next section. Wehner and Hajicek (1971) reported the formation of cones on sputter etched copper when a flux of very low energy molybdenum atoms were allowed to condense on the surface. They concluded that the molybdenum atoms prefer to surface migrate under ion bombardment or thermal agitation until they find other molybdenum atoms to attach to and thus form a group or nucleus which protects the underlying copper surface from being sputtered. Since the etching rate of copper is about three times higher than that of molybdenum, a protrusion is produced, which is then fashioned into a cone, due to the variation of the sputtering rate with the angle of incidence of the beam, as given in Chapter 2.

Tsong and Barber (1972) ion bombarded rotating specimens of silica glass and observed hummocks on the surface. These were found not to be produced if the specimens were stationary and so could not have been formed by the shielding principle, which is now generally

accepted to explain the formation of cones. The formation of the hummocks was shown by the authors to be due to the initial surface unevenness of the bombarded specimens on a microscopic scale. More recent work has been done by Wilson (1973) on the sputtering of semiconductors using 40 keV argon ions and here again the formation of cones and hillocks was observed. Witcomb<sup>1</sup> (1974) studied the formation of surface structures on '18-8' stainless steel and showed conclusively by using the techniques of transmission electron microscopy, scanning electron microscopy, electron probe microanalysis and electron diffraction that the cones resulted from manganese silicate inclusions, while the pillar type structures which were also studied, resulted from fibrous manganese sulphide inclusions.

In recent years, many theoretical approaches have been made by different workers to explain the formation of surface structure on ion bombarded specimens. Following the work of Stewart and Thompson (1969), Nobes et al (1969), developed a theory for the sputtering of amorphous solids by an ion beam and showed that surfaces which have irregularities such as vertical steps and included impurities, reach an equilibrium in which cones are developed on the surface. Further work by Carter et al (1971) showed that a steady state condition on the bombarded surface was only reached if the surface topography consisted of planes aligned, either parallel or perpendicular to the direction of sputtering ion incidence. Catana et al (1972) devised a computer programme to follow the development of surface structure on amorphous solids but this has been shown to be incorrect to deal with features such as cones.

A novel approach has been made by Barber et al (1973) to predict ion-bombarded surface topographies making use of Frank's kinematic theory of crystal dissolution. The authors find that the

predictions show remarkably good agreement with experimental observations and features such as cones, hummocks, hillocks and faceted structures are readily explained. It is concluded by Barber et al (1973), in agreement with Catana et al (1972), that hillocks, hummocks and cones are only transient, unless the half-angle of the apex is equal to  $(\frac{\pi}{2} - \theta)$ , where  $\theta$  is the angle at which the sputtering yield (atoms/ion) is again equal to that at normal incidence.

Carter et al (1973), came to the conclusion that the theories of topographic surface development proposed by Stewart and Thompson (1969) and themselves, can be fitted within the general technique using erosion slowness curves developed by Barber et al (1973), from Frank's treatment of crystal dissolution. Since from the above brief review of the theoretical work on the development of surface structure, it has been indicated that the treatment by Barber et al (1973) explains simply and more satisfactorily the observed results, this will be considered in the next section, along with some other important results.

## 6.2 Theory of Structure Formation

Barber et al (1973), first of all give the two theorems of Frank on crystal dissolution, as applied in chemical etching;

- (1) If the rate of dissolution of a crystal surface at any given time is a function only of orientation, then during dissolution, the locus of an elemental area of crystal surface with a particular orientation is a straight line. Any such locus is known as a dissolution trajectory.
- (2) If the dissolution rate is defined as measured normal to the actual crystal surface, and the polar diagram of the reciprocal of this dissolution rate as a function of orientation is constructed, then the trajectory of an elemental area of crystal

surface of given orientation is parallel to the normal to the polar diagram at the point of corresponding orientation.

The similarities between sputtering and chemical etching can then be seen, since the erosion rate of a given element of specimen surface due to sputtering also depends on the orientation of that element and this is usually given as the variation of the sputtering yield with the angle of incidence of the ion beam. Barber et al then consider the depth,  $d$ , sputtered from a plane surface and this is given as;

$$d = \frac{\phi t}{n} S(\theta) \cos \theta$$

where  $\theta$  is the angle which the ion beam makes with the normal to the target surface,  $S$  is the sputtering yield,  $\phi$  is the number of ions per second striking unit area of the surface, normal to their direction,  $n$  is the number of atoms per unit volume of target material and  $t$  is the time of bombardment. It is convenient to plot the function  $S(\theta) \cos \theta / S(0)$ , which gives the thickness of material removed by sputtering, against  $\theta$ . The resulting curve has the same shape as that of the sputtering yield  $S(\theta)$  against  $\theta$ , shown in Chapter 2, figure 5, page 20. From this data, the reciprocals of the sputtering ratio,  $S(\theta) \cos (\theta) / S(0)$  are then plotted on polar graph paper, in accordance with the second theorem of Frank.

The erosion of any surface, such as that of a glass sphere, by ion bombardment can then be considered and this is shown diagrammatically in figure 36 for a normally incident ion beam. The glass sphere is represented in two dimensions on polar graph paper by a circle. The erosion slowness curve is also shown in figure 36, superimposed upon the starting circular shape. The next step is to draw the orientation trajectories which obey the dissolution

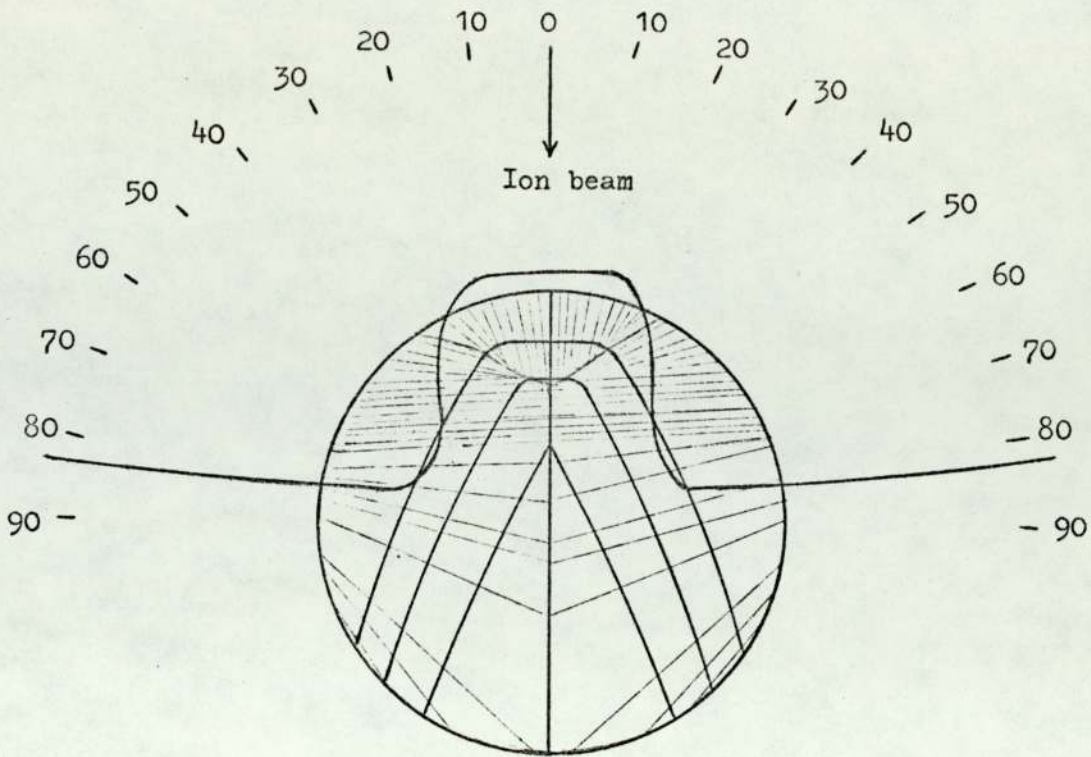


Figure 36. Polar diagram of the erosion slowness curve for silica and the dissolution trajectories and derived profiles for the sputtering of a silica glass sphere. (After Barber et al 1973).

theorems and these will be parallel to the direction of the normals to the slowness curve at corresponding orientations.

The last step is to derive resultant topographies at any given time during bombardment, from the trajectory array constructed. A point is chosen on one of the trajectories, corresponding to a chosen bombardment time, by drawing a line parallel to the tangent to the initial profile, until this line meets the next trajectory and then the same operation is repeated starting from the new point. The resulting shapes are shown in figure 36, the first corresponding to a short bombardment time and the second and third after longer

periods. The shapes depicted agree very well with the experimental observations of Wehner (1959), on the ion bombardment of metal spheres. Barber et al then apply the above treatment to a hemispherical trough and a sinusoidal surface. They show that a deep trough will be turned into a shaft-like depression with vertical walls and a flat bottom, whereas a shallower trough will result in the widening of the trough and a decrease of the slope. The sinusoidal surface is shown to progress towards flatness. The technique is further applied to rotating surfaces and metal single crystals and in all cases, the derived results are shown to be in good agreement with experimental observations.

The cone apex angle  $\alpha_c$  has been shown by Stewart and Thompson (1969) to be given by the relationship;

$$\alpha_c = 180^\circ - 2\hat{\theta}$$

where  $\hat{\theta}$  is the angle of incidence of the incoming ion with the target surface for which the sputter yield curve gives a maximum value. The angle  $\hat{\theta}$  is generally believed to be that critical angle beyond which the bombarding ion has a probability of being reflected from the potential barrier presented by the surface plane of target atoms. Lindhard (1965) shows theoretically that the critical angle for such reflection is given by;

$$\frac{\pi}{2} - \hat{\theta} = \left( \frac{5\pi a_0^2 n^{\frac{2}{3}} Z_1 Z_2 E_R}{(Z_1^{\frac{2}{3}} + Z_2^{\frac{2}{3}}) E_1} \right)^{\frac{1}{2}} \dots\dots (6.1)$$

where  $Z_1$  and  $Z_2$  are the atomic number of ion and atom,  $a_0$  is the Bohr radius (0.53 Å),  $n$  the density of atoms per unit volume,  $E_1$  the energy of the ion and  $E_R$  is the Rydberg energy (13.6 eV). Thus when  $\theta > \hat{\theta}$ , penetration is not possible. Equation 6.1 implies that  $\hat{\theta}$

increases with ion energy, which is reasonable, since the ion can more easily penetrate the surface potential barrier at high energies. The effect of increasing  $Z_1$  or  $Z_2$  is to decrease  $\hat{\theta}$ , since both parameters increase the surface potential. Wilson and Kidd (1971) bombarded gold surfaces with argon and xenon ions of energy up to 20 keV in order to measure cone apex angles and found good agreement between their measured and calculated values using equation 6.1. This has been confirmed by the work of Shimizu (1974), using a field emission scanning electron microscope, with a resolution of 40 Å, to study ion bombarded specimens of copper and gold at high magnification. Witcomb (1974), using different noble gas ions in the energy range 0.2 to 27 keV to study stainless steel and other crystalline materials, showed the dependence of the cone apex angle on the ion bombarding energy, as predicted from equation 6.1.

### 6.3 In-Situ Observation of Cones in the Scanning Electron Microscope

#### 6.3.1 The Growth of a Cone with Bombardment Time

There has been little detailed study showing the actual growth of cones. This is not surprising as in most instances, the cone itself will have grown to a considerable extent before it was observed. However, preliminary experiments during the earlier part of this investigation had shown that cone formation was observed on Araldite, an epoxy resin. Thus this material was used in an attempt to observe the growth of cones. However, these earlier observations also showed that this material is liable to produce artefacts due to temperature degradation. A specimen of araldite was therefore prepared which was in good contact with a sample of OFHC copper and which acted as a heat sink. Observation of cones was restricted to the region of the araldite close to the junction and the observed structure was assumed not to be due to temperature effects.

A 20 mm diameter, 8 mm thick aluminium disc was machined to a depth of 3 mm, but a border of 2 mm width was left on the circumference of the disc. On the underside, the disc was machined so as to have a 3 mm diameter and 3 mm long stub in the centre, so that it would fit directly into the specimen stud holder of the microscope. A piece of copper, 3 mm in thickness was prepared in the shape of a semicircle to fit tightly into the inside of the aluminium stud, as constructed above. To avoid it becoming dislodged during subsequent polishing procedures, Durofix and silver dag were used to adhere the semicircular piece into the stud. The remaining semicircular region was filled with the Araldite resin to a depth of 3 mm, this being heated to make it flow, so that good contact with the copper was obtained at the junction region. After allowing to cure in the oven overnight at 40°C, the sample was polished, the final polish being with 0.25  $\mu\text{m}$  diamond paste. The specimen was ultrasonically cleaned in isopropyl alcohol, coated with gold/palladium alloy by evaporation and then examined in the microscope. No structure of any type was discernible on the specimen, at this stage.

This specimen was then etched with the spherical source using the normal settings ( $V_t = 6\text{kV}$ ,  $I_t = 2\text{ mA}$ ,  $I_b = 40\ \mu\text{A}$ ) and the specimen was observed in the SEM every 2 hours. During the initial period of etching, no cones could be found near the junction at an early stage of formation. However, after 14 hours of etching a cone like structure with a particle on its apex was seen to have been produced, 0.1 mm away from the junction, on the araldite, near the outer border of the etched region, where the very low energy ions were impinging. A study of the growth of this structure with bombardment time and also the change of shape that takes place was carried out, in order

to substantiate whether the shielding principle for cone formation is valid and also to see if the cone is an equilibrium structure. The fact that the cone type structure was in a region of the surface where low energy ions were impinging, was an advantage for this particular study, since the changes taking place could be followed more closely.

A selection of eight micrographs at various stages of growth are given in plate 7. They are all taken at a magnification of 650X and with an angle of  $45^{\circ}$  between the specimen surface and the electron beam. At every stage of the examination, in order to take micrographs, the surface of the specimens was coated with gold/palladium alloy, making sure that the specimen was replaced in the microscope in exactly the same position. The bombardment times for the micrographs a, b, c, d, e, f, g and h of plate 7 were 14, 32, 44, 72, 80, 108, 124 and 130 hours respectively.

It is clearly shown that while the shielding particle is being eroded, the structure grows in height, reaching a maximum height of 50  $\mu\text{m}$  in micrograph (C). Once the shielding particle has been removed, a change of shape to a true cone like structure takes place and on subsequent bombardment, the cone starts to decrease in height, until on the last micrograph, 7(h), it has nearly disappeared. Further bombardment past this stage was carried out in which it was found that nothing at all remained to show that a cone had existed at the particular place. It should be noted that the surrounding area of the cone changes with etching time. Due to the fact that great care was taken in the initial preparation and cleaning of the specimen and that no particles were observed on the unetched specimen, it is concluded that the particle responsible for the formation of the cone was a small inclusion near the surface of the Araldite.

After etching for 14 hours with the spherical source. The initiating particle can be clearly seen at the top.

(a)

30  $\mu$ m

After etching for a total of 32 hours. The structure has grown in height and the particle has diminished in size.

(b)

30  $\mu$ m

After etching for a total of 44 hours. The particle has very nearly disappeared and the structure becomes more conical.

(c)

30  $\mu$ m

After etching for a total of 72 hours. The initiating particle has completely disappeared and the structure has been fashioned into a cone and is getting smaller.

(d)

30  $\mu$ m

After etching for a total of 80 hours. The cone is slightly smaller, keeping the same shape.

(e)

30  $\mu$ m

After etching for a total of 108 hours. The cone has diminished in size even more.

(f)

30  $\mu$ m

After etching for a total of 124 hours. The cone is very small.

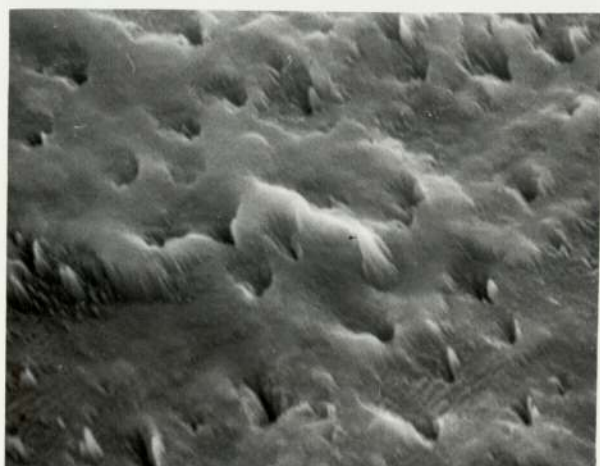
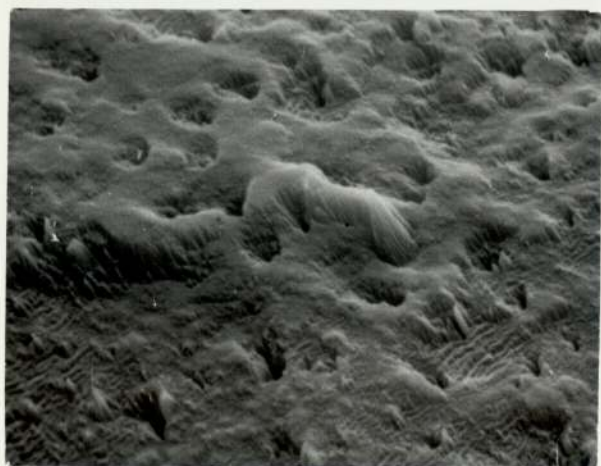
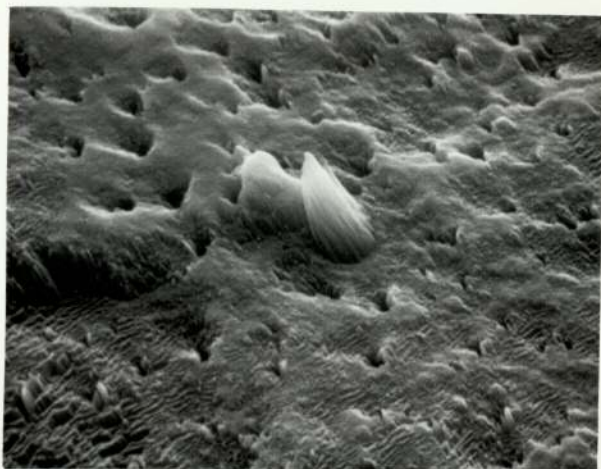
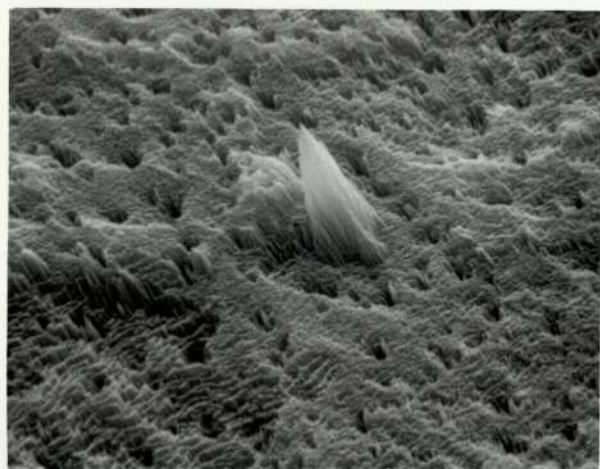
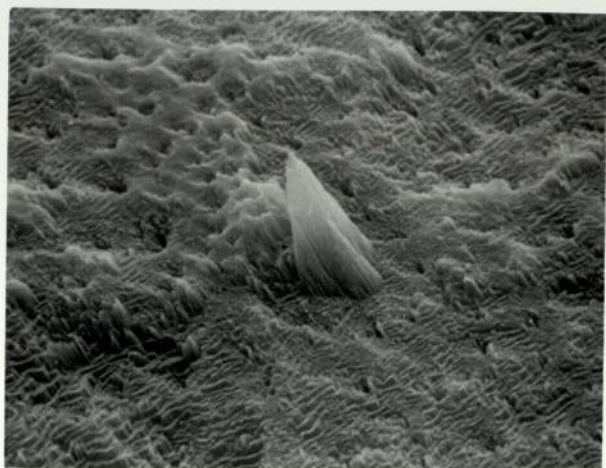
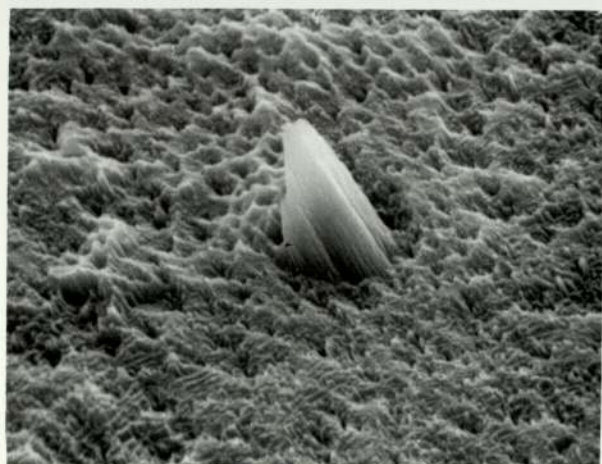
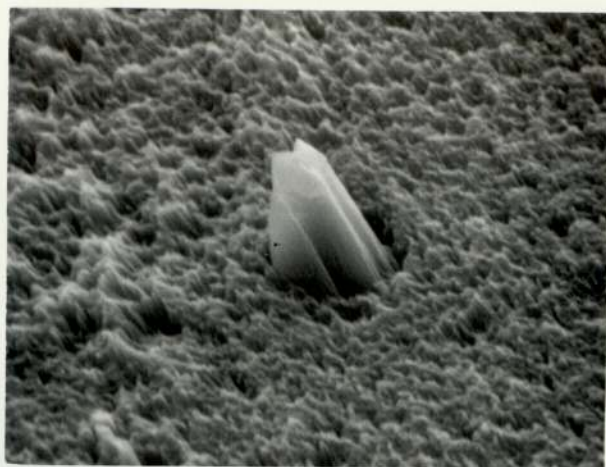
(g)

30  $\mu$ m

After etching for a total of 130 hours. The cone has nearly disappeared in this micrograph.

(h)

30  $\mu$ m



### 6.3.2 Study of Cones on Different Materials

During the course of the work, remarkable cone like structures were observed on many different materials. Plate 8, shows 4 micrographs in which cone like structures are evident. Plate 8(a), (650X), shows a perfectly symmetrical cone observed on the copper part of the specimen described in the previous section. This was observed after 14 hours etching and the height is about 60  $\mu\text{m}$ . A circumferential ditch at the base of the cone can be seen and the surrounding copper crystals are also observed to be deeply etched.

The micrographs of plate 8(b), (c) and (d) are of cones formed on sectioned, polished and ultrasonically cleaned dental tissues, after etching with the cylindrical source and these have been taken with an angle of  $30^\circ$  between the specimen surface and electron beam. Plate 8(b) is of a cone, (approximate height 25  $\mu\text{m}$ ), formed on the enamel after etching for 12 hours and is taken at a magnification of 1300X. Again the circumferential ditch at the base of the cone is clearly evident. The prismatic structure of the enamel has also been revealed in the surrounding etched region. Plate 8(c), (2000X), is of the lining material of the tooth, which is zinc oxyphosphate and this is taken after 8 hours etching. A large cone, (approximate height 30  $\mu\text{m}$ ), is seen but a smaller cone can also be seen, which presumably has been almost eroded away. Plate 8(d), (1300X), illustrates cone formation on the surface of dental amalgam after 8 hours etching. These cones are quite unlike those formed on the other specimens, in that the whole surface structure appears to comprise of a mass of cones of varying height, ranging from about 10 to 30  $\mu\text{m}$ . The most remarkable feature is the central large cone-like structure, in which a particle can be clearly seen at its tip.

In addition to the cone like structures illustrated in plates 7

Cone formed on copper after etching for 14 hours with the spherical source.

(a)

30  $\mu\text{m}$

Cone formed on dental enamel after etching for 12 hours with the cylindrical source.

(b)

15  $\mu\text{m}$

Cone formed on the lining material of a tooth after etching for 8 hours with the cylindrical source.

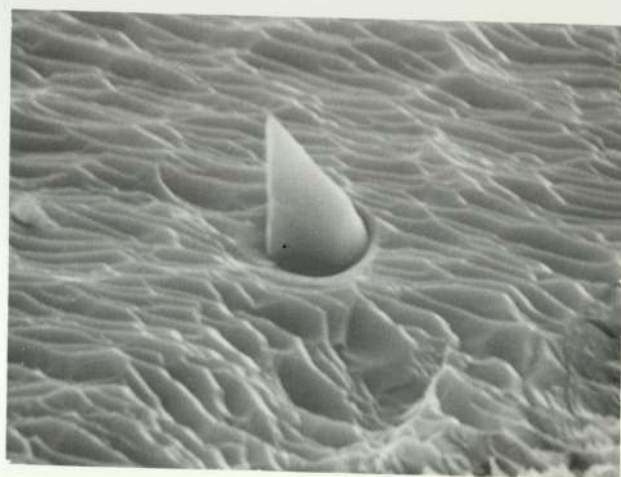
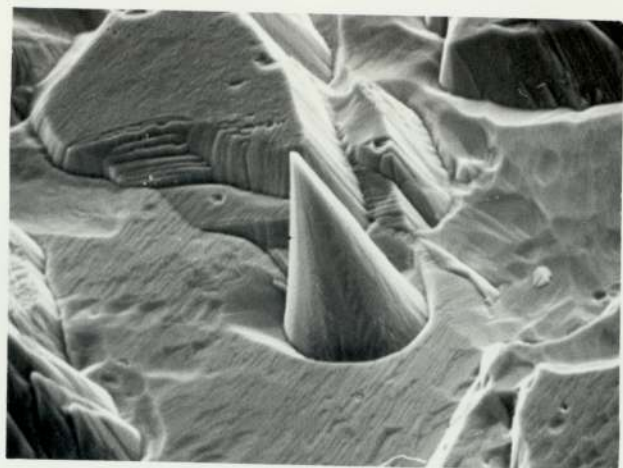
(c)

10  $\mu\text{m}$

Cone type structures formed on dental amalgam after etching for 8 hours with the cylindrical source.

(d)

15  $\mu\text{m}$



and 8, some other remarkable features were also observed on the surface of Araldite, with both the spherical and cylindrical sources. These are shown in the three micrographs of plate 9 in which the angle between the specimen surface and electron beam was  $45^{\circ}$ . The micrograph in plate 9(a) is taken at a magnification of 650X after etching for 84 hours. The pillar like structure seen in the centre is about  $85 \mu\text{m}$  high and is similar to those observed by Witcomb<sup>1</sup> (1974) on stainless steel. Plates 9(b) and (c) show clusters of cones, some of which have whisker like growths, of length several times the height of the cone, extending from the tip of the cone. It also appears that some of these whiskers have already fallen off the cones. Micrograph (b) is again 650X, whereas micrograph (c) is 1300X. These micrographs are of the same Araldite specimen but after repolishing and cleaning and then etching for a further period of 16 hours. The features were again away from the intense central region on the araldite, just inside the border of the etched region, at typically 0.3 to 0.5 mm away from the junction. With continued etching, these cones were rapidly observed to diminish in size, with the whiskers dropping off, before finally disappearing as a result of further etching.

#### 6.4 Discussion of Results

Most of the results presented in section 6.3 can be explained with current models of cone formation. However, results presented in plate 9 are more difficult to understand and possible explanations will be given as to the formation of these artefactual structures.

The micrographs of plates 7 and 8, substantiate the view that cones formed on the surface of a material during ion etching are due to some foreign particle on the surface, or from an inclusion in the matrix, which has a lower sputtering yield than the matrix itself.

Pillar like structure after  
etching for 84 hours with  
the spherical source.

(a)

30  $\mu\text{m}$

Cones with whisker like growths  
at the tip after etching for 16  
hours with the spherical  
source.

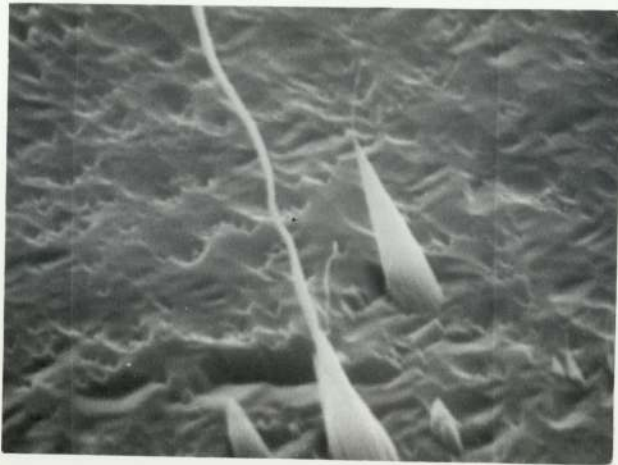
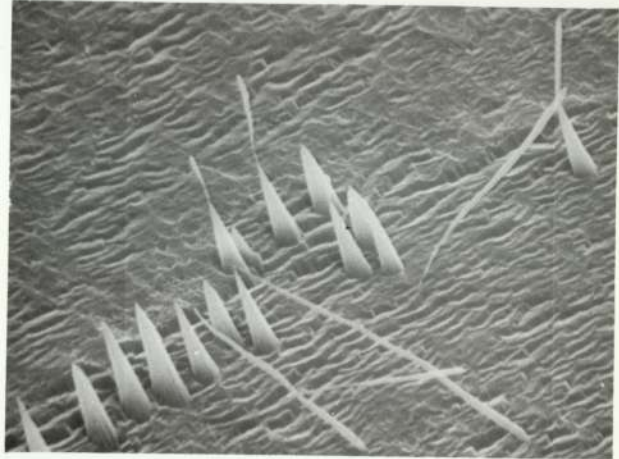
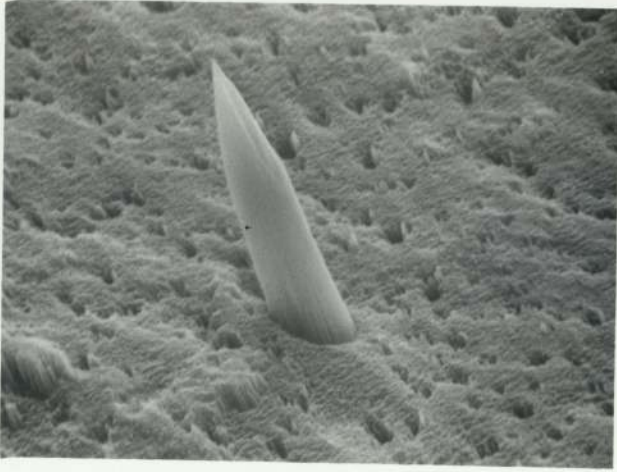
(b)

30  $\mu\text{m}$

Cone with a whisker like growth  
at the tip at high magnification.

(c)

15  $\mu\text{m}$



As the sample is being etched, the particle shields a small region of the specimen and causes a protrusion to form on the surface. The edges of the particle are slowly etched away to produce sloping sides, which eventually become inclined at an angle to the incident ion beam corresponding to the maximum sputtering yield. This process continues resulting in the growth of the cone. Ultimately the shielding particle is completely eroded away, leaving a cone comprising entirely of the matrix. X-ray analysis of the cone on the enamel in plate 8(b), using a Kevex ray X-ray attachment to the Cambridge Stereoscan, showed that the cone had the same composition as the matrix. With further ion bombardment, the cone itself will be fairly rapidly eroded away. This effect is clearly demonstrated by the sequence of micrographs in plate 7. The moat or ditch observed at the base of the cones, such as those on the copper and the enamel plates 8(a) and 8(b), conceivably results from an increase in the ion flux in this region, due to ion reflection from the sides of the cone (Wilson 1973). The large number of cones observed on the surface of the amalgam in plate 8(d), undoubtedly occurs due to the nature of the material, which contains many elements all having different sputtering rates.

All these cones were observed with the specimen stationary during etching. As expected from the model discussed above, about the formation of these cones, none were observed when the specimen was continuously rotated during etching. It would thus appear that to avoid these artefacts, it would be advantageous to rotate the specimen. However, in general this advantage is offset by the fact that the structural features of any material revealed during ion etching are less clear and in some instances hardly seen at all. Furthermore provided that one is able to recognise these cone like artefacts,

the presence of one, or a small number of cones, could be advantageous, as this gives immediate and permanent information concerning the direction of the incident ion beam used during etching, since the cone will always grow in this direction. On the other hand, where there are a large number of cones, as in the amalgam plate 8(d), it is very unlikely that this ion etching technique can be of much value for structural information.

The unusual artefactual features shown in plate 9 cannot be explained on the basis of the theory for cones. In this present study, although a relatively large number of materials have been used for ion etching, these effects have only been observed on *Araldite*. However, it is suggested that the pillar like structure of plate 9(a) may be due to a fibrous inclusion in the material, similar to those reported by Witcomb<sup>1</sup> (1974) in stainless steel. The fibrous inclusion must undoubtedly have a low sputtering yield and this accounts for the greater resistance in shaping the whole fibre into a cone. In the case of the whisker like growths shown in plates 9(b) and (c), no explanation at this stage can be offered for the precise nature of their formation, but the observations suggest that these again may be due to fibrous inclusions which contain a central core which has an extremely low sputtering yield. Another explanation for these is that they may be due to a growth phenomenon, resulting from temperature degradation of the *Araldite*. Some more results are presented in Chapter 7 on the etching of *Araldite*, where this possible degradation effect will be considered in greater detail. Evidently, further work requires to be carried out to establish the formation of these whisker like growths.

## CHAPTER 7

### ION ETCHING OF VARIOUS MATERIALS

#### 7.1 Introduction

During the early part of this investigation it was considered essential to use the ion etching facility with a large variety of materials, in order to evaluate the feasibility of the in-situ technique which has been developed. This has been by and large achieved, but by choosing real problems of importance in industrial and research laboratories. It was felt that a broad classification into conducting and insulating sections was really not sufficient, since the etching of biological tissues was a particularly important contribution and this should receive due credit in a separate section. A further sub division into hard and soft biological tissues has also been made, since very little work has been carried out on the etching of soft tissues, presumably because of their high sensitivity to thermal effects.

During these experiments, samples have been etched when stationary and also when rotating at about 9 to 10 revolutions per minute by means of an electric motor which could be used to continuously drive the specimen rotation control, via a simple gearing mechanism. Plate 5 shows a close view of this, in which the top of the motor can just be seen behind the goniometer stage, while plate 4 shows the motor actually in position for rotation of the sample. However, unless otherwise stated, it should be assumed that the specimen was stationary during etching. Furthermore, both the cylindrical and spherical source have been used for etching and in all

cases the normal settings have been used, that is for the cylindrical source,  $V_t = 8$  kV,  $I_t = 6$  mA and  $I_b = 160$   $\mu$ A at a pressure of  $2 \times 10^{-5}$  torr and for the spherical source  $V_t = 6$  kV,  $I_t = 2$  mA and  $I_b = 40$   $\mu$ A at a pressure of  $1.5 \times 10^{-5}$  torr. It should also be noted that unless stated, the angle between the specimen surface and electron beam was  $45^\circ$  when the electron micrographs were taken.

In this Chapter, the successes and partial failures of etching metallic, ceramic, plastic and biological samples will be discussed and illustrated with the appropriate micrographs. In all of these studies, observations of the surfaces were made at regular intervals, but the micrographs shown in all instances are after a period of etching which gave satisfactory information. The final etching time varied from about 1 hour to 26 hours.

## 7.2 Conducting Materials

### 7.2.1 Annealed-Extended Copper

Problems are frequently encountered when trying to study the texture and properties of commercial copper using chemical methods after extending and annealing the copper at different temperatures. For example, it is often found that the contamination of the specimens arising from grease marks and polishing with carborundum papers and diamond paste, can not be removed by chemical etching or ultrasonic cleaning. Also the process is very messy and difficult to control. As a result the micrographs of these specimens are of poor quality and rarely free from black patches. Ion beam etching was used in an attempt to overcome these problems.

The specimens were initially in the form of 12.7 mm diameter copper rods and these were annealed at  $700^\circ\text{C}$  for  $1\frac{1}{2}$  hours. They were then divided into two groups, after allowing to cool naturally to

room temperature in the furnace. The specimens from group one were then cold rolled to 5% of the initial diameter, while those from group two were rolled to 1.5% of the initial diameter. The specimens were further divided for subsequent annealing at 400°C and 700°C for 1 hour, after which they were quenched to preserve the microstructure. After polishing - in the final stage with 0.25  $\mu$ m diamond paste - they were ion etched in the SEM for 3 hours using the spherical source. Micrographs were then taken to show the structure.

Plate 10 shows four micrographs, all of which are at a magnification of 320X. The specimens for micrographs (a) and (c) were cold rolled to 5% while (b) and (d) were cold rolled to 1.5% of the initial diameter. Subsequently, (a) and (b) were annealed for 1 hour at 400°C while (c) and (d) were annealed for the same time at 700°C. Clearly the effect of annealing at the higher temperature is evident from micrographs (c) and (d) in that the crystals have grown to a much larger size. As expected, the crystal size in micrographs (b) and (d) is smaller than that in (a) and (c) respectively, because of the greater extension of the former two. Thus if one goes from micrographs (a) to (b) or (c) to (d), the difference in crystal size is purely due to a different amount of cold rolling. However, when going from (a) to (c) or (b) to (d), the difference in the crystal size is caused by the fact that (a) and (b) were annealed at 400°C, whereas (c) and (d) were annealed at 700°C. The annealing temperature is shown to be the most critical factor in determining the size of the crystals, and hence for controlling important properties, such as the strength of the material. The ion etching has been shown to be very successful compared to chemical etching in revealing the required structure.

Cold rolled to 5% of the initial diameter, annealed at 400°C for 1 hour and then quenched. Etched with the spherical source for 3 hours.

(a)

60  $\mu\text{m}$

Cold rolled to 1.5% of the initial diameter, annealed at 400°C for 1 hour and then quenched. Etched with the spherical source for 3 hours.

(b)

60  $\mu\text{m}$

Cold rolled to 5% of the initial diameter, annealed at 700°C for 1 hour and then quenched. Etched with the spherical source for 3 hours.

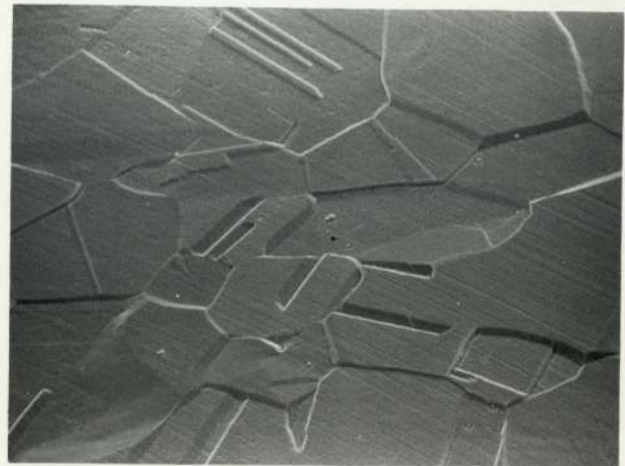
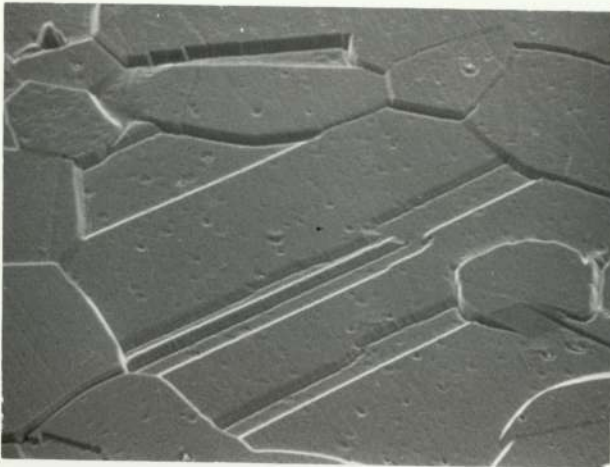
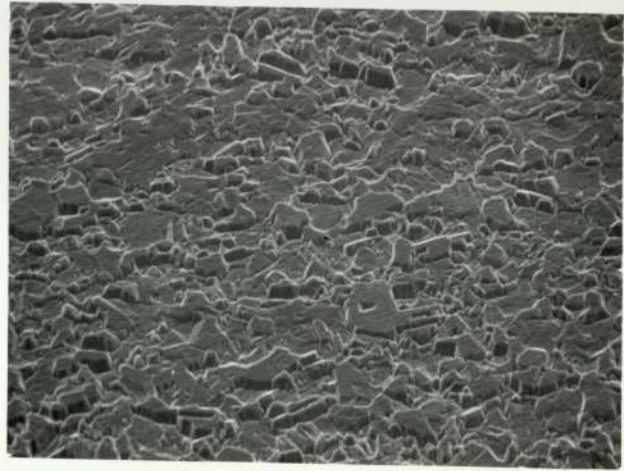
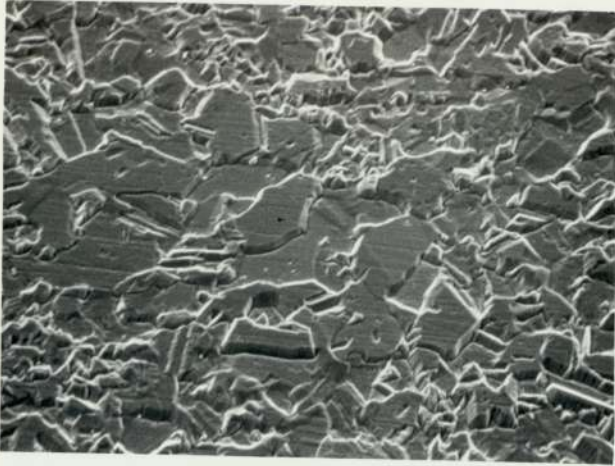
(c)

60  $\mu\text{m}$

Cold rolled to 1.5% of the initial diameter, annealed at 700°C for 1 hour and then quenched. Etched with the spherical source for 3 hours.

(d)

60  $\mu\text{m}$



### 7.2.2 Copper-Iron Sinter

The material in this case is a copper-iron sinter, the composition being 10% copper in iron together with 0.2% carbon. This material can be chemically etched with ferric chloride but not very successfully, since the structure obtained is not very clear in that the grain boundaries are hardly seen. It was decided to ion etch this material with the specimen stationary and also rotating to see if any differences were observed.

The polished specimens were etched in the microscope for 2 hours using the cylindrical source, operating at the normal settings. Plate 11 shows four micrographs in which (a) and (b) are for a rotating specimen and (c) and (d) are of a stationary specimen. Micrograph (a), (300X), shows the grain boundaries and the porosity of the material in that regions can be seen where voids have been exposed. Micrographs (b), (c) and (d) are all at a magnification of 3000X. Micrograph (b) shows grains at high magnification and it can be seen that these have been rounded, since the sample was rotated during etching. Micrograph (c) again shows some grains but here one of the grains shows striations and this is believed to be pearlite, which is a particular structure of iron consisting of alternate laminations of ferrite and cementite. The micrograph (d) is an X-ray image of (c) using copper X-rays and clearly shows the distribution of the copper at the grain boundaries. This effect is the inverse of that obtained with chemical etching, where the copper is left behind. A conclusion to be made is that for this particular example, stationary etching yields slightly more information than rotating etching, since the pearlitic structure is hardly obtained in the rotating case. Thus it has been shown that the technique is extremely useful to study these type of samples.

Specimen etched rotating for 2 hours with the cylindrical source showing the grain boundaries and porosity of the material.

(a)

60  $\mu\text{m}$

The rotating etched specimen at higher magnification showing rounded grains.

(b)

10  $\mu\text{m}$

Specimen etched for 2 hours, showing grains, with one grain showing striations which is probably pearlite.

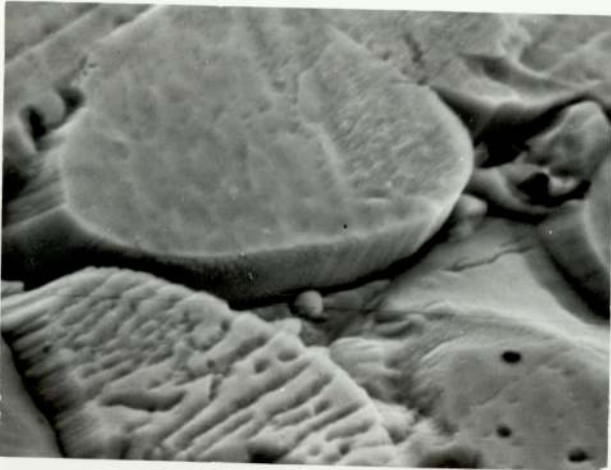
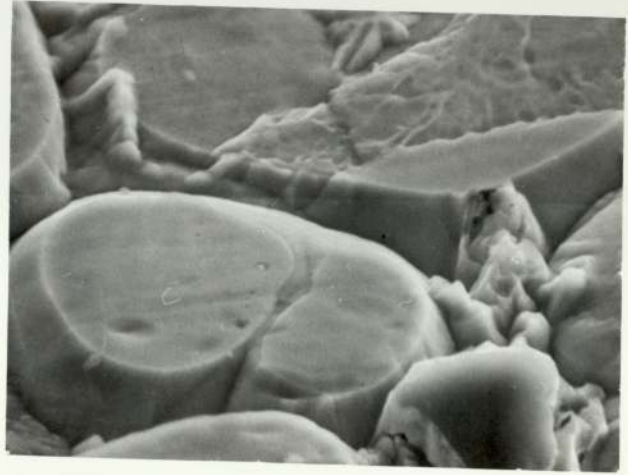
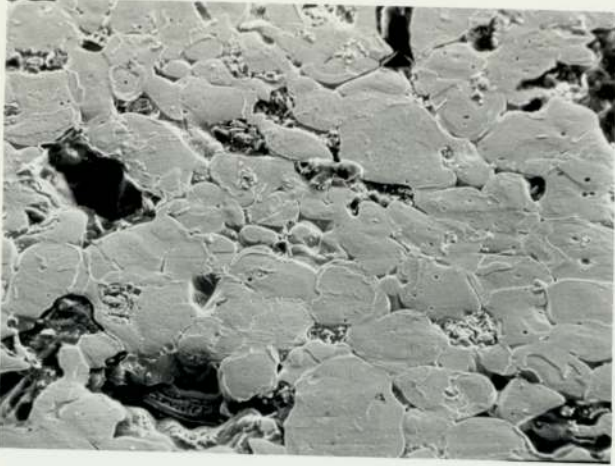
(c)

10  $\mu\text{m}$

An X-ray image of (c) showing the distribution of copper at the grain boundaries.

(d)

10  $\mu\text{m}$



### 7.2.3 Fractured Piston Steel

This specimen is an example of a 'high speed' hardened piston steel, being mainly composed of ferrous, but with small amounts of chromium, molybdenum, vanadium, tungsten and carbon. This material can be etched chemically with nitol (2% concentrated nitric acid in alcohol) but the structure is not brought out in the desired manner. Two specimens of this material were ion etched, one specimen stationary and the other rotating.

Plate 12 shows four micrographs after etching for 2 hours with the cylindrical source, where (a) and (c) are at a magnification of 3000X, while (b) and (d) are 2500X. In the cases (a), (b) and (d) the specimen was rotating. In all the micrographs various size particles can be seen to have been exposed, distributed fairly uniformly in the matrix. X-ray scans in micrographs (b) and (d) for molybdenum and vanadium show that these elements are present in the particles and a similar analysis for tungsten, indicated that it was also present. It is evident that the stationary etched specimen, micrograph (c), has been etched much more than the rotating specimen. The reason for this was found to be due to a slight difference in the treatment received by the two specimens. This being that the stationary etched specimen had been annealed twice, whereas the other specimen was only annealed once. This difference has been brought out in the ion beam etching, but no difference at all can be observed with chemical etching, since this cannot be controlled in such a satisfactory manner. It can be concluded that the annealing time is also an important factor for determining the properties of a material, as well as the annealing temperature, which has been shown to be extremely important from section 7.2.1. Furthermore, the particles seen in all the micrographs are undoubtedly, carbides of

Specimen etched rotating for 2 hours with the cylindrical source, showing a distribution of various size particles.

(a)

10  $\mu\text{m}$

X-ray line scan on the same specimen as (a), showing that the particles are rich in molybdenum.

(b)

12  $\mu\text{m}$

Specimen etched for 2 hours with the cylindrical source, showing that the particles and matrix have been etched intensely.

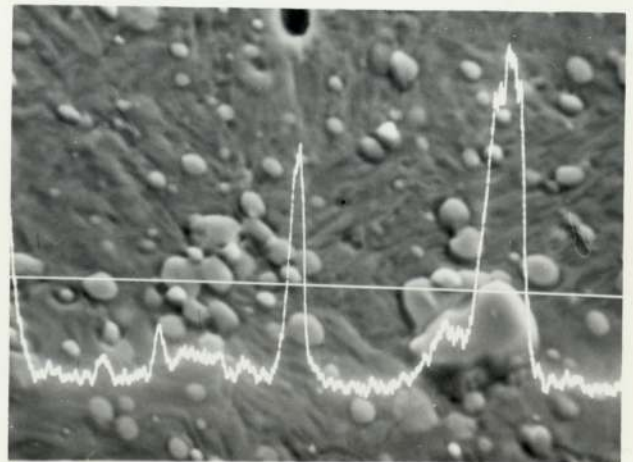
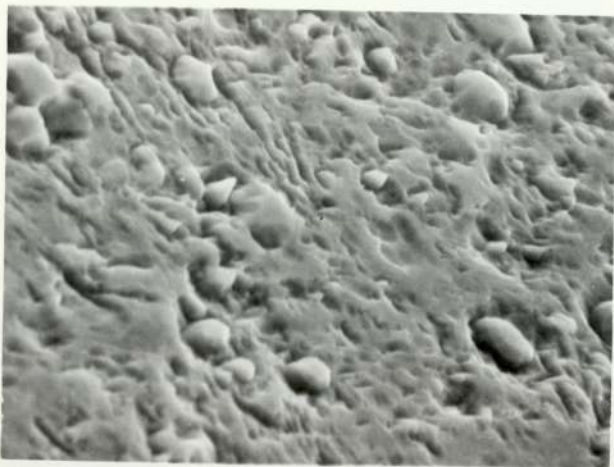
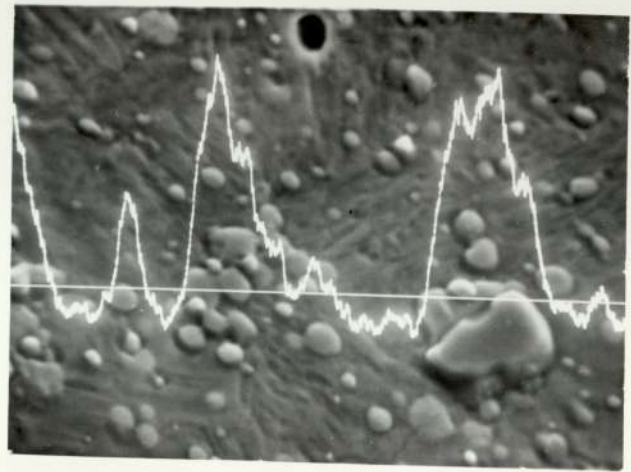
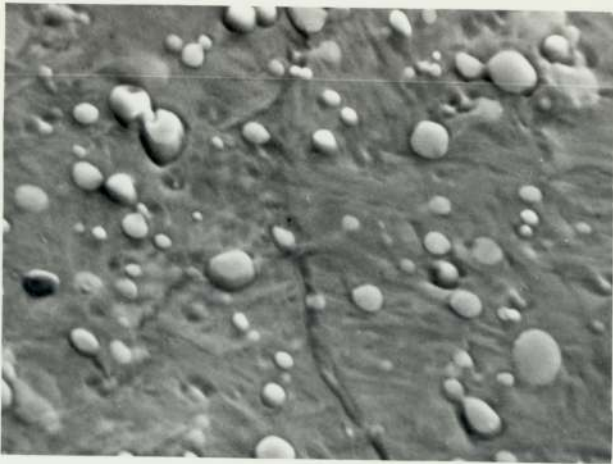
(c)

10  $\mu\text{m}$

X-ray line scan of the same region as in (b), showing that the particles are also rich in vanadium.

(d)

12  $\mu\text{m}$



the additive elements. The technique can be used as a quality control for this type of investigation, since the amount of etching and the distribution of particles can be related to important properties of the material.

### 7.3 Insulating Materials

#### 7.3.1 Silicon Nitride Ceramic

The first of the insulating materials investigated is a newly developed one having a very high strength, for use in such purposes as the manufacture of turbine blades. The structure is not fully known and two samples were prepared for ion etching with the spherical source. One of these was etched stationary and the other rotating for 3 hours.

Plate 13 shows three micrographs, where (c), (3000X), refers to the rotating specimen and (a) and (b) to the stationary specimen, at a magnification of 300X. Micrograph (a) is taken in an intensely etched region and shows a large number of small craters on the surface, whilst in (b) taken away from the intensely etched region, the density of craters is much less. Micrograph (c) shows a particle on the surface at high magnification and an X-ray scan shows that this is rich in silicon. A large number of these particles of varying sizes were observed, most of them embedded into the surface of the matrix and it is possible that the craters are formed as a result of eroding these completely.

#### 7.3.2 Soda Glass

A glass specimen (5 mm x 5 mm x 1 mm) was examined in the microscope and no structure of any type could be seen, except for a few contamination particles. Half of the specimen was covered with aluminium foil and then etched in the microscope for a total of 10

Specimen etched for 3 hours with the spherical source showing a high density of small craters.

(a)

60  $\mu\text{m}$

Same specimen as in (a) but in a less intensely etched region where the distribution of craters is lower.

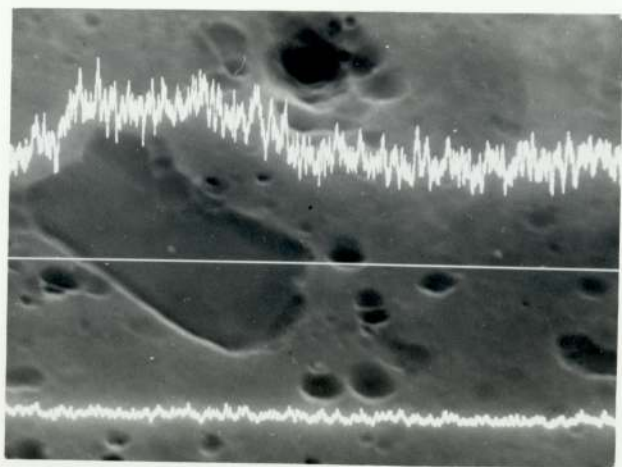
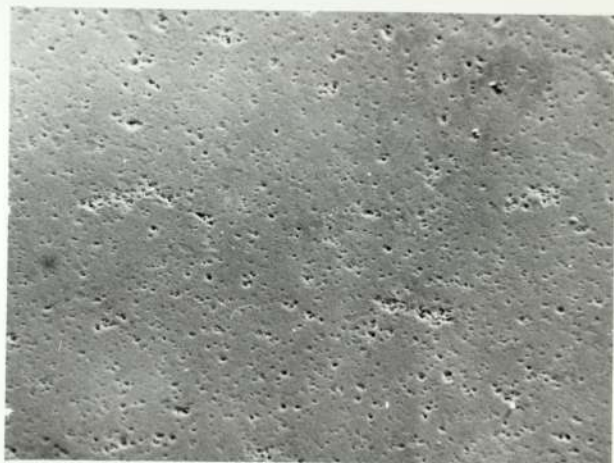
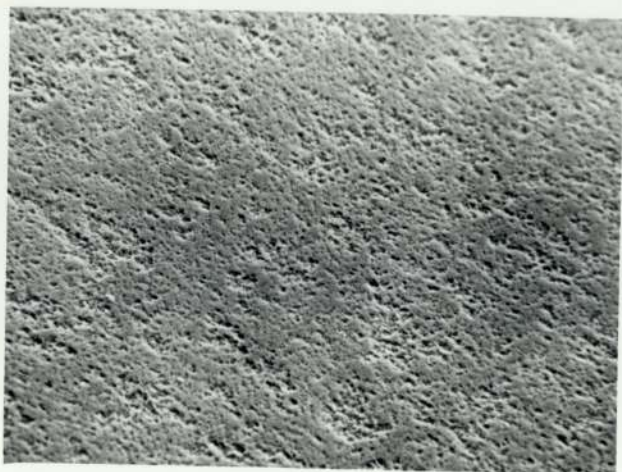
(b)

60  $\mu\text{m}$

This is a high magnification micrograph of a specimen etched rotating for 3 hours with the spherical source and shows a large particle. An X-ray line scan of this particle shows it to be rich in silicon.

(c)

10  $\mu\text{m}$



hours. The shielding foil was then removed but no clear etched step could be observed as was the case for the copper in section 5.3.1, plate 6. Plate 14(a), (650X) is taken in a region away from this boundary and very little structure can be seen. However, at a comparatively low magnification, (150X), in the region of the boundary, plate 14(b), shows a series of elongated rises extending from the boundary. It is believed that this is due to the imperfect nature of the edge of the aluminium foil which has deflected the incident ion beam.

It was then decided to etch the specimen, without any shielding foil, for a further period of 16 hours. After examination, a definite grooved type of structure was obtained and this is shown in micrographs (c) and (d) of plate 14, both at a magnification of (650X). Micrograph (c) is taken in a less intensely etched region and also shows a single cone like structure. Since the cone indicates the direction of the incident ion beam, the grooves are seen to be formed almost normally to this direction. Micrograph (d) is taken in the intensely etched part of the specimen after rotation through  $90^{\circ}$ .

Navez et al (1962) carried out an extensive study on the etching of glass under different conditions of bombardment and concluded that the morphology obtained is a function essentially of the geometry of the bombardment. They showed that principally three types of structure was obtained, depending upon the angle of incidence of the ion beam, (measured with respect to the normal to the sample surface). At angles greater than about  $75^{\circ}$ , striations parallel to the beam were obtained. At angles between about  $30^{\circ}$  and  $70^{\circ}$ , a system of parallel ridges oriented perpendicular to the ion beam was obtained. If the bombardment was carried out with the

The surface of the specimen after etching for 10 hours with the spherical source.

(a)

30  $\mu\text{m}$

Shielded with aluminium foil.

Showing the elongated rises extending from the boundary, in the same specimen as in (a).

(b)

130  $\mu\text{m}$

After etching for a further 16 hours, without the shielding foil, showing a grooved structure and also a cone.

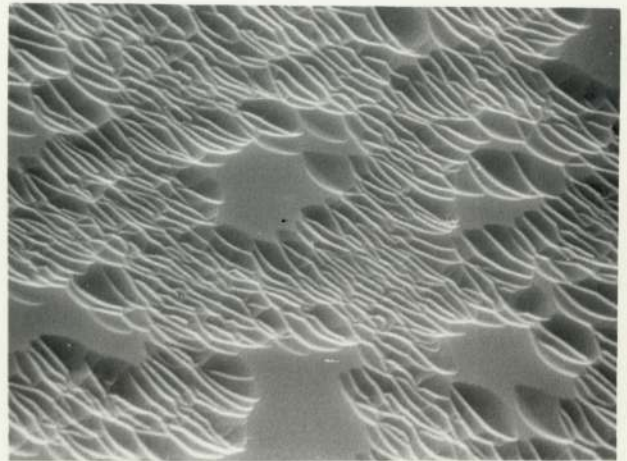
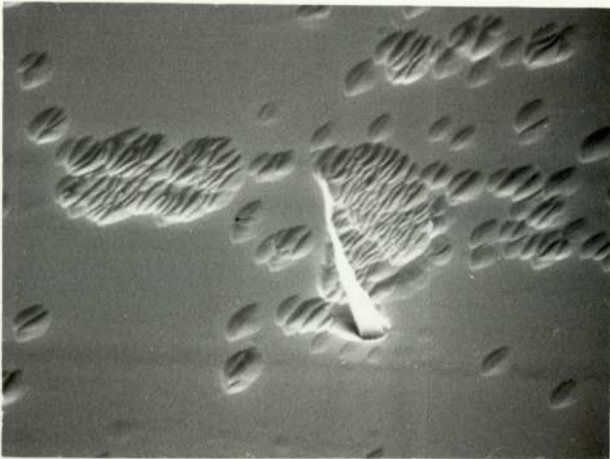
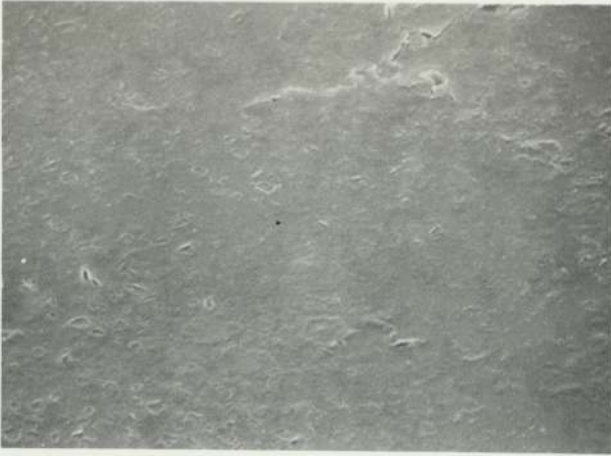
(c)

30  $\mu\text{m}$

In an intensely etched region, after rotating the specimen through  $90^\circ$ .

(d)

30  $\mu\text{m}$



specimen normal to the ion beam, then a regular globular structure was obtained. The results presented in micrographs (c) and (d) of plate 14 are consistent with Navez et al's observations of parallel ridges oriented perpendicular to the ion beam. There is little information of structural value that has been revealed using this technique and effects seen in micrographs (c) and (d) are undoubtedly artefacts.

### 7.3.3 Acrylic Plastic

Two samples of this material were examined, one being etched stationary and the other rotating for 1 hour using the spherical source. Plate 15 shows two micrographs of this material at a magnification of 5000X in which micrograph (a) is of the stationary specimen, while (b) is of the rotating specimen. Micrograph (a) shows a grass like structure, while (b) indicates a chain linked type of structure. Also on this micrograph a region towards the lower half shows damage induced due to heating by the electron beam when viewing at high magnification. Clearly there is very little variation of etching rate of the specimen so that the surface appears relatively uninteresting. The 'grass like' structure on the stationary specimen is probably due to the very small crystalline regions known to exist in this material and greater etching has occurred at these points. On the rotating specimen, an aligned structure is not produced and the circular regions are probably where the crystalline regions have been preferentially etched.

### 7.3.4 D.M.C. Plastic

This is a high strength plastic containing many fillers and is termed, "dow moulded compound". Basically it is a polyester with additives such as glass fibres, alumina, calcium carbonate and small

A specimen after etching for 1 hour with the spherical source, showing a grass like structure.

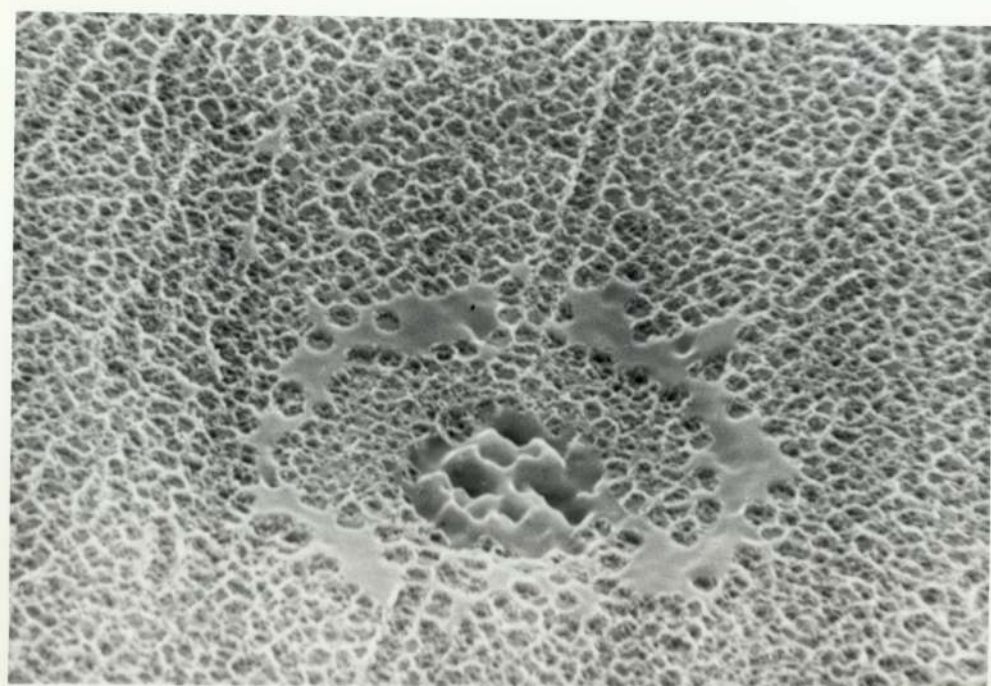
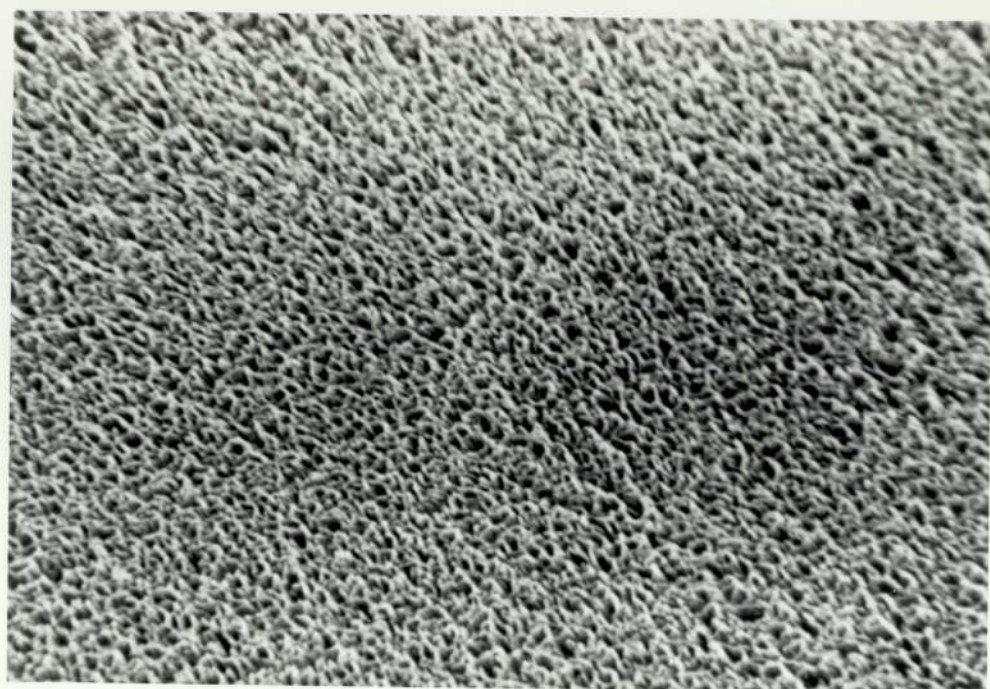
(a)

5  $\mu$ m

A second specimen after etching rotating for 1 hour with the spherical source, showing a chain-linked type of structure. Also showing damage caused due to heating by the electron beam.

(b)

5  $\mu$ m



amounts of other materials. Two samples were again prepared for etching with the specimen stationary and also rotating and they were etched for 1 hour with the spherical source.

Plate 16 shows three micrographs, in which micrograph (a), (3000X), is of the stationary specimen, while (b) and (c), (1500X) are of the rotating specimen. In all three micrographs, large and small particles can be seen and in micrograph (a), part of a glass fibre has been revealed by eroding the surrounding material. X-ray analysis in micrograph (b) shows that the large particles are rich in aluminium, while analysis in (c) shows that the smaller particles of the matrix are rich in calcium. It is believed that the large particles are mainly aluminium oxide and the small ones of the matrix contain a large proportion of calcium carbonate. The ion beam etching technique can be usefully applied to this type of material, since the distribution of the various compounds, controls the properties and ion etching combined with X-ray analysis yields valuable information.

#### 7.3.5 Acetal Plastic

Two samples of this material were again prepared and etched for 1 hour using the spherical source, with one sample stationary and the other rotating. Plate 17 shows two micrographs of this material, both at a magnification of 2000X. The micrographs show a fibrous type of structure, which is aligned in the stationary etched specimen, (micrograph (a)). This structure is again thought to be produced by crystalline regions in the specimen and most simple plastics demonstrate this phenomenon. This example has shown that it is unlikely that any real valuable information can be obtained for this type of material using the ion etching technique.

A specimen etched for 1 hour with the spherical source in which a glass fibre has been revealed.

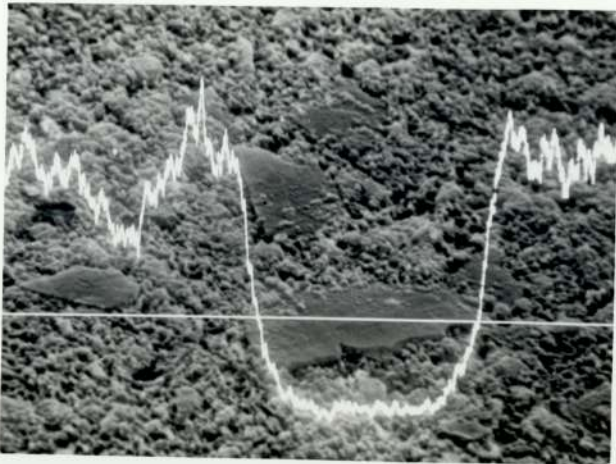
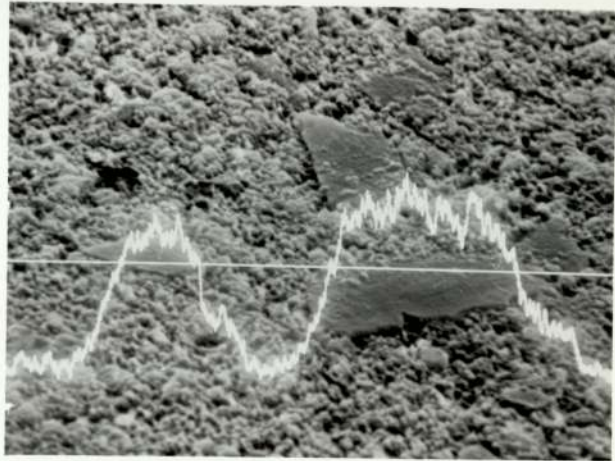
10  $\mu\text{m}$

A second specimen etched rotating for 1 hour with the spherical source in which large and small particles can be seen. An X-ray line scan shows the large particles are rich in aluminium.

20  $\mu\text{m}$

The same region as that in (b). An X-ray line scan shows that the smaller particles of the matrix are rich in calcium.

20  $\mu\text{m}$



A specimen etched for 1 hour with the spherical source, showing an aligned fibrous type of structure.

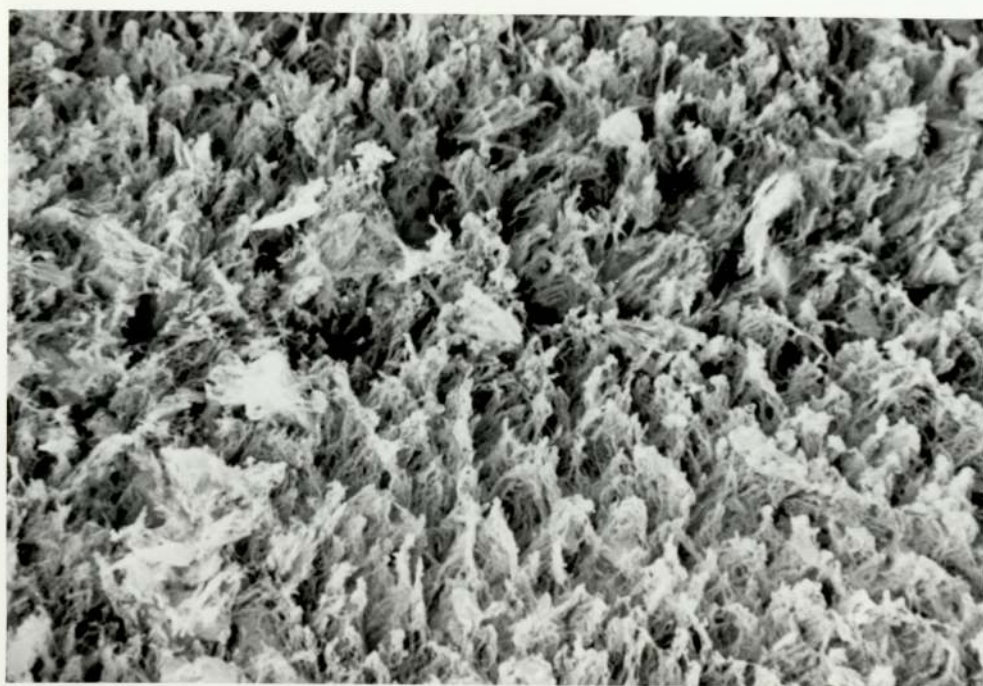
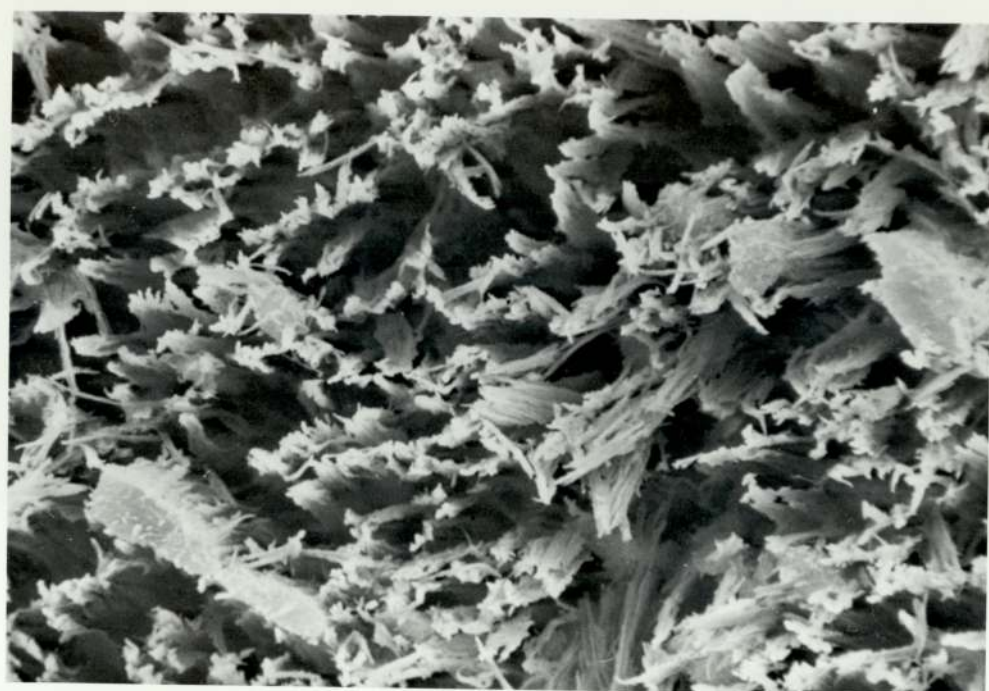
(a)

10  $\mu$ m

A second specimen etched rotating for 1 hour with the spherical source, again demonstrating a fibrous structure, which in this case is random.

(b)

10  $\mu$ m



### 7.3.6 Araldite Epoxy Resin

This is a widely used material having applications in many fields. This particular specimen has been already referred to when discussing the artefacts in section 6.3.2. Plate 18 shows three micrographs after etching for 16 hours with the spherical source and micrograph (a), (320X), shows the junction between the Araldite and copper in which it is demonstrated that a good contact between the two materials was obtained. Micrograph (b), (1300X), which was taken on the Araldite very close to the junction indicates a definite crystallographic type of structure, with possibly crystal planes being observed. The nature of the material would not be expected to give such a regular type of structure. It was further observed that this structure was evident down the whole length of the junction, although it was more intense in the middle. However, traversing out from the junction, this structure was found to rapidly diminish within about 200  $\mu\text{m}$ . Further away at a distance of more than about 500  $\mu\text{m}$ , this structure could not be observed at all. The micrograph (c), (1300X), is taken at a distance of 1 mm away from the junction and shows an entirely different type of structure. At this stage, it could not be conclusively said if this effect was due to thermal degradation of the Araldite or due to strain built up near the junction, when the material cures after preparation, or a combination of the two effects.

In order to eliminate the possible effect due to strain, a cast of Araldite was prepared separately, polished and then butted up against a polished piece of copper. However, after many attempts, it was found that even at the best, a gap of some 20  $\mu\text{m}$  existed between the copper and the Araldite, which was an order of magnitude larger than the worst case, when the Araldite was allowed to set naturally

Araldite

Copper

Showing the junction after  
etching for 16 hours with the  
spherical source.

(a)

60  $\mu\text{m}$

In a region close to the  
junction on the araldite.

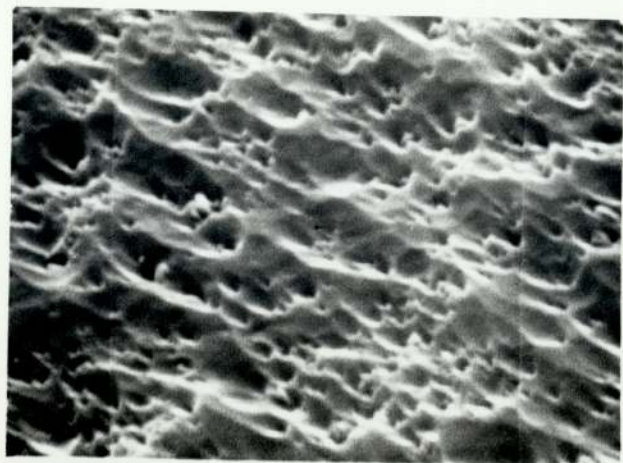
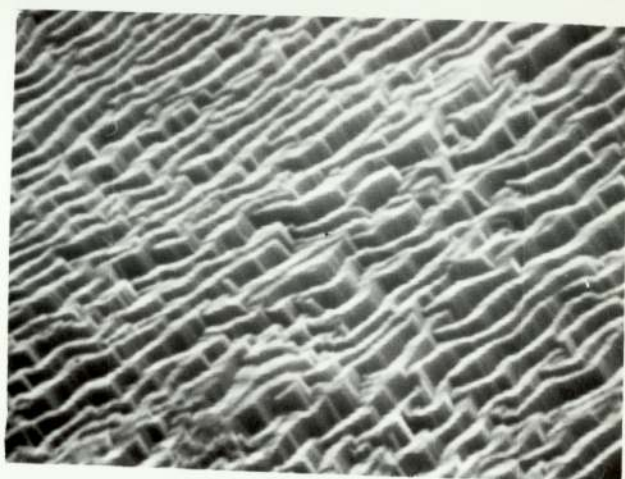
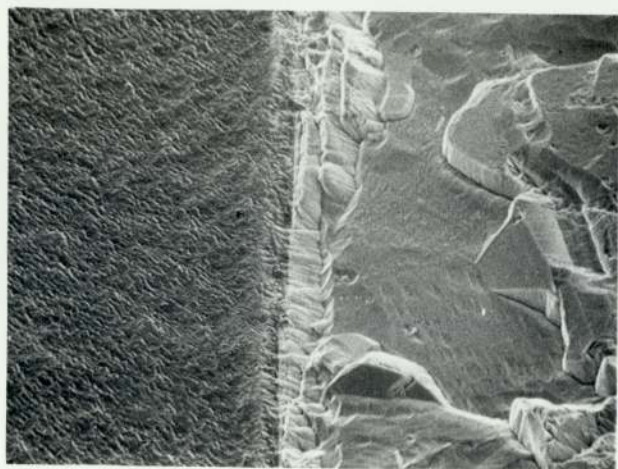
(b)

15  $\mu\text{m}$

At a distance of 1 mm away from  
the junction on the araldite.

(c)

15  $\mu\text{m}$



against the copper. On polishing a specimen thus prepared, it was found that a structure similar to that in plate 18(c) was obtained. Hence it appears that the structure obtained near the junction, (plate 18(b)), is characteristic of the araldite, whereas the structure obtained in 18(c) is due to thermal degradation. The nature of the material does not warrant a periodic type of structure as observed in this case and clearly further work requires to be carried out with this material to substantiate these results.

#### 7.4 Soft Biological Material (Rat Duodenum)

There has been very little work done using ion etching on soft biological material. Stuart et al (1969) used radio frequency ion etching to study the internal structure of normal and abnormal human blood cells and concluded that the technique yielded valuable information. Ambrose et al (1970) used the same type of technique to study human brain tumours and here again they found that valuable information could be obtained. Frisch et al (1974) carried out an extensive study of normal and hematological diseased blood cells using both an rf ion source and a cylindrical ion source, of the type described in this investigation. They demonstrated that structural differences were obtained between the normal and abnormal cells. Also they found rf etching to be more suitable for the particular examples investigated. However, in contrast to these workers, Hodges et al (1972) carried out an extensive study of mammalian and avian cells using an rf source and concluded that the ion-etching technique was of no significant value for the examination of subsurface structures of soft biological tissues. It must be emphasised that rather lengthy preparation procedures have to be employed before soft biological material samples can be ion etched. These involve fixation processes in chemicals such as methanol, osmium tetroxide,

glutaraldehyde etc. for various times.

In the present instance it was desired to ion etch specimens of rat duodenum which had been prepared for examination in the transmission electron microscope. The specimens were fixed in glutaraldehyde and osmium tetroxide, dehydrated, embedded in epon resin and cured in an oven at 60°C for 24 hours. After ultra-microtoming the face of the 2 mm x 2 mm block, the sample was coated with gold/palladium and examined in the SEM. No structure of any type was visible at this stage. Specimens were then etched stationary and rotating using the spherical source. Examination in the SEM showed structural features of the gut and these are shown in the three micrographs of plate 19.

Micrograph (a), (320X), and (b), (650X), are of a stationary specimen which was etched for 2 hours. Micrograph (c), (650X), is of a rotating specimen which was etched for 4 hours. Micrograph (a) shows part of the general structure of the relatively large villi cells, contained within the gut. At the borders of this are the very much smaller micro-villi cells which can just be seen and cells connected with these are also visible. The micrograph (b), as well as showing the cellular structure also shows a duct extending upwards from just below the bottom left hand corner of this micrograph. It has been suggested that this is a passageway for the excretory materials such as the hormones and blood vessels. The last micrograph of plate 19, (c), shows a group of cell nuclei which are made visible due to the fact that the nucleus is preferentially stained by the osmium, which has a lower sputtering yield than the unstained surrounding tissue.

Clearly the technique of ion etching has been shown to provide valuable information about the microstructure of the rat duodenum,

A specimen etched for 2 hours with the spherical source, showing part of the structure of a villi cell.

(a)

60  $\mu\text{m}$

The same specimen as that in (a), again demonstrating the cellular structure, but in addition showing a duct.

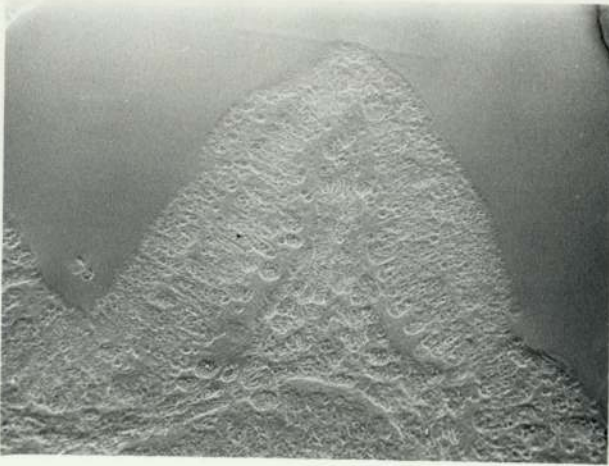
(b)

30  $\mu\text{m}$

A second specimen etched rotating for 4 hours with the spherical source, showing a group of cell nuclei.

(c)

30  $\mu\text{m}$

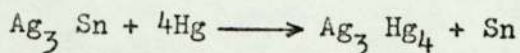


since a large variation of sputtering rate is provided by the staining elements. The technique can be used to study many other different types of tissues and also the effect of staining with different chemicals can be investigated, since these are preferentially absorbed to different extents by the various parts of the tissue.

## 7.5 Hard Biological Material (Mammalian Dental Tissues and Restorative Materials)

### 7.5.1 Form of a Restored Tooth

The application of the ion etching technique to human teeth formed a major part of this investigation and included not only structural information about dental tissues and restorative materials, but also included specific problems which arose during the earlier part of this work. The tooth basically consists of an outer surface of enamel which is highly mineralised and which extends to about half way down the sides of the tooth. The composition of the enamel is approximately 98 per cent inorganic and 2 per cent organic material, (Bevelander 1963). The inorganic salts of enamel are present in the form of calcium triphosphate (hydroxyapatite). Below the enamel is the dentine and this is composed of approximately 70 per cent inorganic and 30 per cent organic material. The inorganic component again consists of mainly calcium triphosphate, plus small amounts of sodium and magnesium and other calcium salts. The restorative material commonly used in fillings is commercial amalgam, formed from a metallic powder, the composition of which is, silver 68%, tin 26%, copper 5%, zinc 1% and some other trace elements. This powder is then mixed with mercury and the amalgamation reaction is;



In this study whole teeth as well as sections were examined and plate 20 shows two micrographs of whole teeth (a and b) and two micrographs of tooth sections (c and d). These micrographs clearly demonstrate the versatility of this scanning electron microscope, since whole teeth can be easily examined. Micrograph (a), (8X), shows a premolar tooth into which a cavity has been made, ready for restoration. Micrograph (b), (8X), shows the top of a whole molar tooth which has been restored with an amalgam filling. Micrograph (c) is taken of a polished transverse section of a tooth and polishing marks can be seen on the amalgam which is on the right hand side of the gap. The area to the left of the gap includes both enamel and dentine but they cannot be distinguished in this unetched specimen. However, after etching the specimen for 4 hours using the spherical source, micrograph (d), taken of the same area, reveals the dentine in the top left hand corner of the micrograph. The gap between the enamel and amalgam demonstrates that in this example, there is not a very good seal between these two materials. This aspect will be considered more fully in section 7.5.3. In the next section, the structure of various dental and restorative materials which have been examined by ion etching will be discussed.

## 7.5.2 Structure of Dental Tissues and Restorative Materials

### (a) The Enamel

This is the hard and mainly mineral outer covering of a tooth and the structure is prismatic in nature as mentioned previously in section 6.3.2. The two micrographs of plate 21 show this structure on polished longitudinal sections. Micrograph (a), (1000X), is taken after etching for 4 hours using the spherical source and is taken in

A premolar tooth with a prepared cavity, ready for restoration.

(a)

2 mm

A molar tooth which has been restored with an amalgam filling.

(b)

2 mm

Enamel

Amalgam

A transverse section of a tooth after polishing, showing the junction between the enamel and amalgam.

(c)

60  $\mu$ m

Dentine

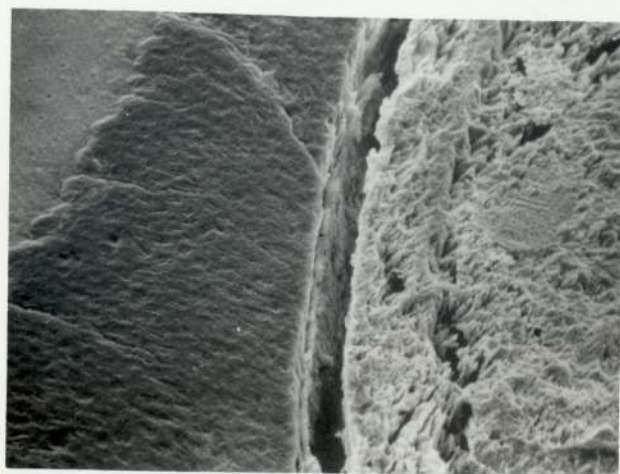
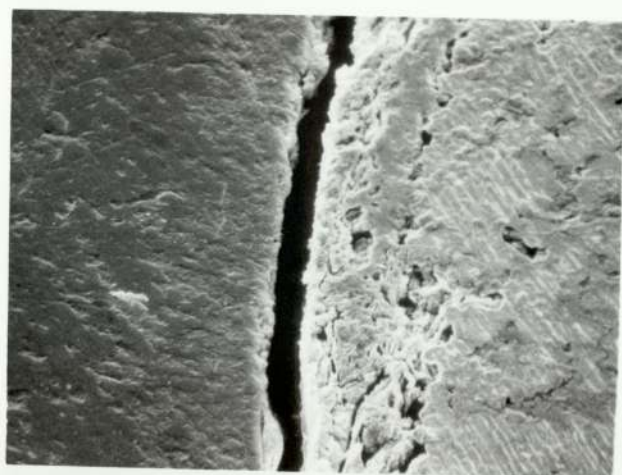
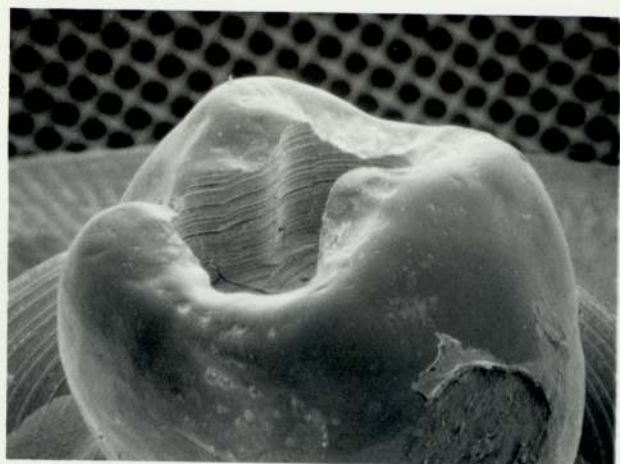
Enamel

Amalgam

Same area as in (c), but after etching for 4 hours with the spherical source, revealing dentine in the top left hand corner.

(d)

60  $\mu$ m



Longitudinal tooth section after etching for 4 hours with the spherical source, showing an intensely etched region of the enamel.

(a)

20  $\mu$ m

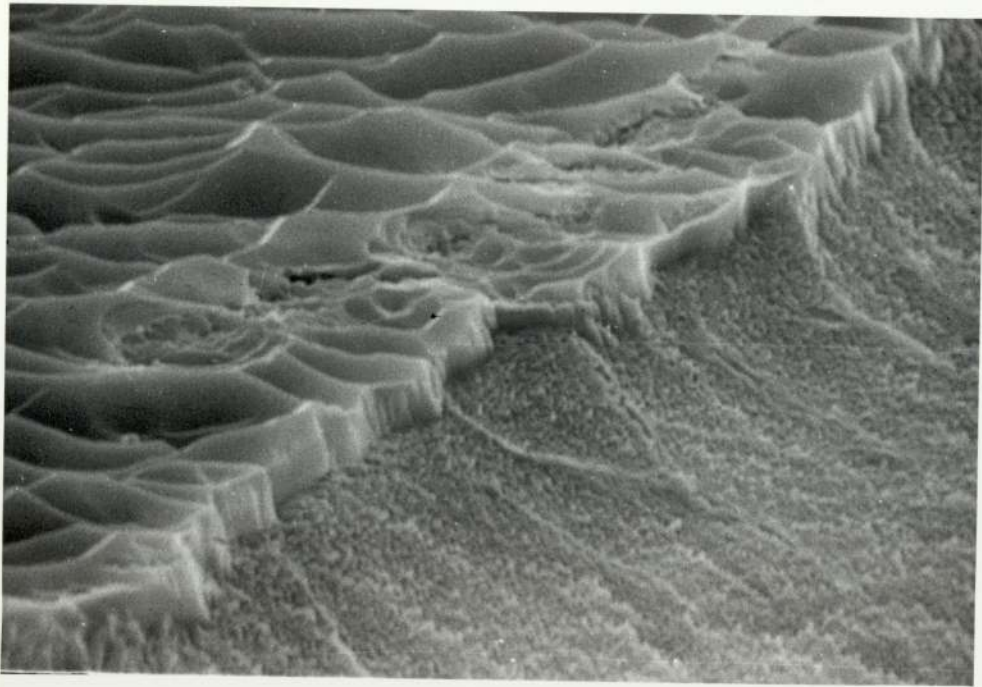
Enamel

Longitudinal tooth section, after etching for 12 hours with the cylindrical source, showing the amelo dentinal junction.

Dentine

(b)

10  $\mu$ m



an intensely etched region of the enamel and demonstrates the stepped prism like structure. Stewart and Boyde (1962) ion etched specimens of human and rodent teeth and showed that the technique yielded valuable information about the structure. Micrograph (b), (2000X), shows the junction between the enamel and dentine which is normally referred to as the "amelo-dentinal junction". This is taken after etching for 12 hours with the cylindrical source, using an angle of  $30^{\circ}$  between the specimen surface and the electron beam. The dentine has been etched more than the enamel, since it is the softer material and the step produced is about  $5\mu\text{m}$  high. Some dentinal tubules extending from the junction that have been exposed by the ion etching can also be seen and these will be discussed in the next section.

(b) The Dentine

The dentine contains the dentinal tubules which are hollow with a diameter of 1 to  $3\mu\text{m}$  and contain within them, the nerve fibres and tissue fluid. There are 25,000 tubules per  $\text{mm}^2$  and they run from the pulp in the roots of the tooth, to the edge of the enamel. When a tooth decays and the decay reaches the edge of the dentine through the enamel, the pain is transmitted through the sensory nerves in the dentinal tubules to the root of the tooth. These dentinal tubules can be exposed by ion etching in different planes, depending upon how the section is cut.

Plate 22 shows four micrographs of sections of teeth in which the tubules are shown. Micrograph (a), 1300X, shows a longitudinal section of a tooth which has been etched for 4 hours with the spherical source. The tubules are seen to be running almost parallel to the surface of the specimen, whereas in micrograph (b), (1300X), they have been exposed obliquely. Some cones are also seen in this micrograph which has been etched for only 2 hours using the

Longitudinal tooth section etched for 4 hours with the spherical source, showing the dentinal tubules running almost parallel to the surface.

(a)

15  $\mu$ m

Longitudinal tooth section etched for 2 hours with the cylindrical source, giving an oblique view of the tubules. Some cones can also be seen.

(b)

15  $\mu$ m

Transverse tooth section, etched for 4 hours with the spherical source, giving an end on view of the tubules.

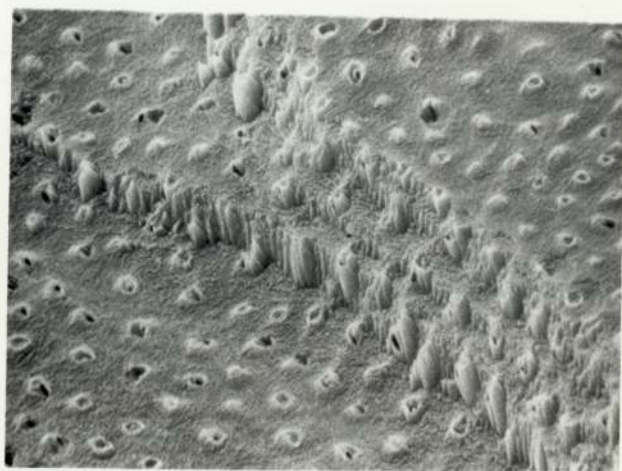
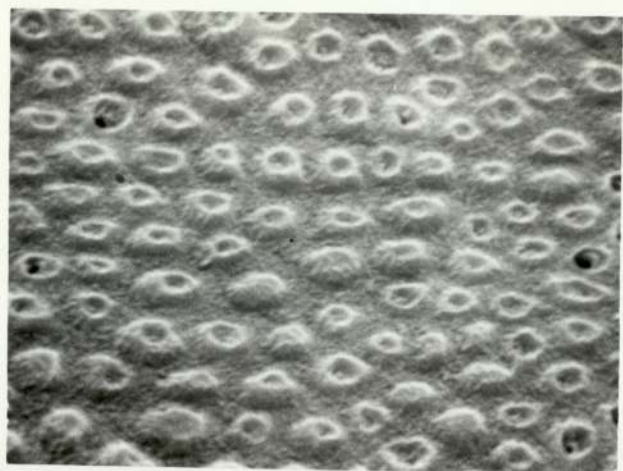
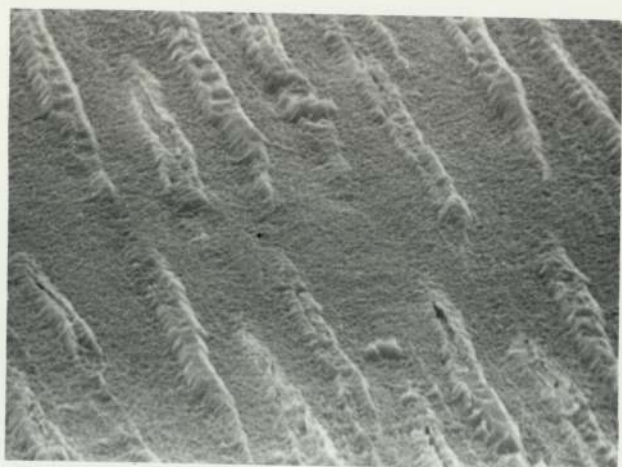
(c)

15  $\mu$ m

At the base of a cavity after etching for 8 hours with the spherical source. A dramatic effect produced due to the drill marks.

(d)

30  $\mu$ m



cylindrical source. Micrographs (c) and (d) are transverse sections and in (c), (1300X), which has been etched for 4 hours with the spherical source, an end on view of the tubules can be seen. Micrograph (d), (650X), is at the base of a cavity, similar to the one shown in plate 20(a), after etching for 8 hours with the spherical source. The tubules are again end on, but in addition, steps can also be seen which have been produced by the drill used for the cavity preparation. A dramatic effect has been produced which helps to demonstrate the true tubular nature of the tubules.

(c) The Amalgam

In order to examine the structure of commercial amalgam, a block of the material was prepared, which was then polished. Micrographs (a) and (b), (650X), of plate 23 shows the structure before etching. Micrograph (a) demonstrates the particulate nature of the material and is taken in a large void on the polished specimen, since the amalgam was found to be full of both large and small voids. Micrograph (b) shows a smaller void and the polished surrounding surface containing even smaller ones. Micrograph (c), (650X) was taken after etching the specimen while rotating for 2 hours using the spherical source. The structure is relatively uninteresting but it should be noted that the whole surface does not produce a cone type structure, since the specimen was rotated during etching. The voids are again clearly demonstrated, even on this etched specimen. Micrograph (d) is also of the amalgam but this is on a section of an extracted tooth. This has also been etched for 2 hours with the specimen rotating and using the spherical source. The interesting feature to note here is that the surface appears to have melted, presumably due to heating by the ion beam and has erupted into bubbles. The surrounding region again shows the same structure as that of plate 23(c), which

Polished amalgam surface in a large void and also showing much smaller voids.

(a)

30  $\mu\text{m}$

Showing a smaller void than in (a) and also the polished surrounding surface.

(b)

30  $\mu\text{m}$

Surface after etching rotating for 2 hours with the spherical source.

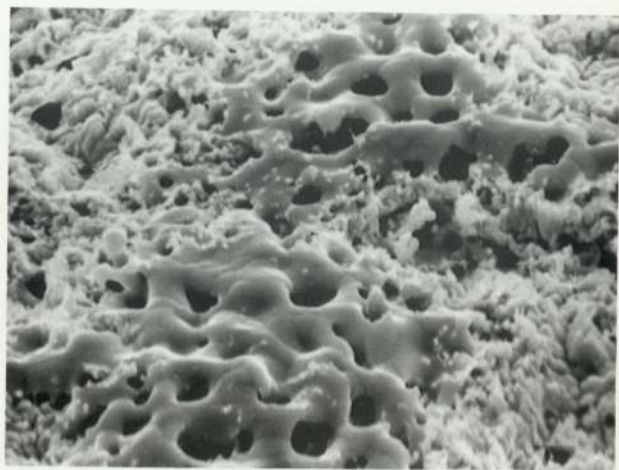
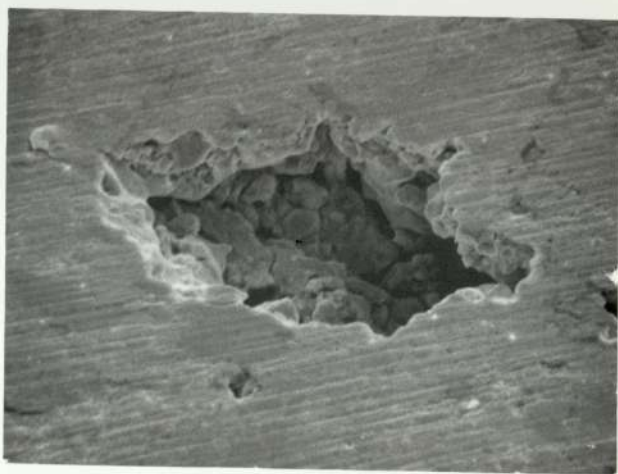
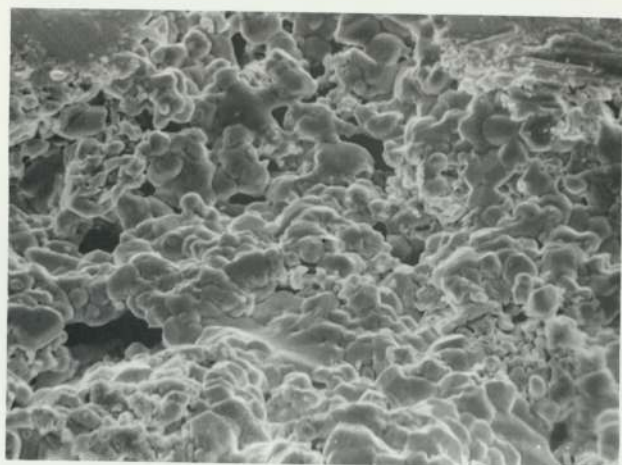
(c)

30  $\mu\text{m}$

Amalgam surface on a sectioned tooth after etching while rotating for 2 hours with the spherical source. Surface appears to have melted, presumably due to heating by the ion beam.

(d)

30  $\mu\text{m}$



is expected, since both specimens were etched rotating for the same time. Amalgam is known to melt over a wide range of temperature on account of its composite nature. Thus this effect could be expected in very localised areas.

A new type of amalgam that has been recently developed is spherical amalgam. Not very much is known about this material since it is not, as yet, widely used. Plate 24 shows two micrographs of the powder used in this material, before amalgamation with the mercury. Both are taken at the same magnification of 1000X and with an angle of  $30^{\circ}$  between the specimen surface and the electron beam. In micrograph (a), it can be seen that the spherical particles vary in diameter from about 2 to 50  $\mu\text{m}$ . Micrograph (b) is taken after etching for 4 hours using the cylindrical source and is covered with a cone type of structure which has been produced over the whole area and some of the larger spherical particles have been reduced in size by about a half. A point to note is that most of the tops of the spheres have cracked and the reason for this is not known at this stage.

### 7.5.3 Cavity Margin Amalgam Interface

In fundamental dental research, there has been a great deal of work carried out in order to ascertain why amalgam restorations fail. A number of methods have been used to study microleakage around amalgam restorations, including resistance to air pressure, (Pickard and Gayford (1965)) and radioactive isotopes, (Going et al (1960)). These various techniques have shown qualitatively that a gap exists between the cavity wall and restoration. It was decided to examine newly bench filled teeth which excluded any effects of the oral environment and also to examine normal restored teeth after extraction. The existence of the gap between the cavity margin and

Spherical amalgam powder showing particles of varying sizes.

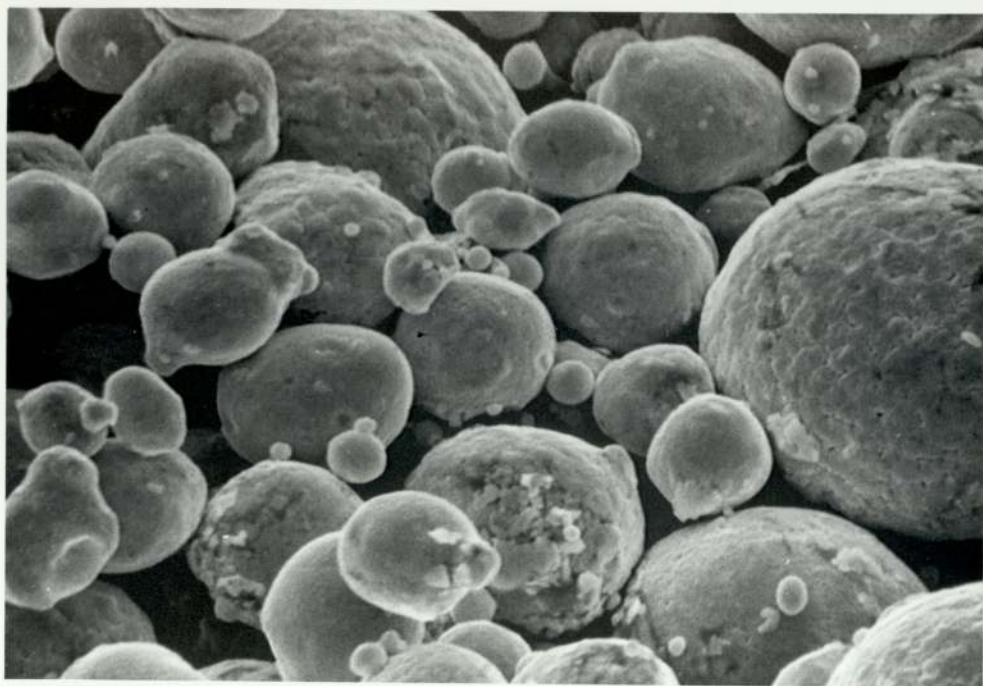
(a)

20  $\mu$ m

After etching for 4 hours with the cylindrical source, showing the surface deeply etched and the larger spheres can be seen to have cracked at the top.

(b)

20  $\mu$ m



the amalgam can be easily demonstrated using the SEM as was shown in plates 20(c) and (d). However, this type of investigation can be criticised on the grounds that the tooth has been sectioned prior to examination and the gap may have been produced during the sectioning process. In order to overcome this objection, whole teeth were examined. Ion etching was employed in order to remove the adherent surface contamination and the pulverised damaged layers of the teeth. This revealed the true characteristic structures of the materials. In particular the cavity-restoration interface can be most clearly brought out. Bench filled and restored extracted teeth were examined, before and after ion etching using the spherical source.

Plate 25 shows four micrographs of the amalgam-cavity interface, all at a magnification of (320X), in which (a) and (b) are of a bench filled tooth. Micrograph (a) has been taken before etching and (b) is of the same area after etching for 4 hours. It can be seen that the gap has been apparently widened from about 5  $\mu\text{m}$  to at least 30  $\mu\text{m}$ . Even if we assume an etching rate of 10  $\mu\text{m}/\text{hr}$  for the amalgam, which is a highly optimistic figure, then in 4 hours a maximum of about 40  $\mu\text{m}$  of amalgam could have been removed. Clearly this would indicate that although on the unetched specimen a reasonable seal between the amalgam and cavity wall is indicated, this is in fact not the case, since the thickness of this amalgam in the vicinity of the cavity wall is less than about 40  $\mu\text{m}$ .

Thus it is reasonable to suppose that a normal filling which contains this burnished layer can be similarly eroded away in the oral environment to reveal a relatively large gap. With a gap of this order of magnitude, it is possible that liquids and bacteria could penetrate this enlarged gap to produce caries which enhance the decay of the tooth. Experiments in this laboratory, (Singh (1975)), have confirmed that this is possible by showing that water can relatively

Amalgam

Enamel

Amalgam cavity interface on a  
newly bench filled tooth.

(a)

60  $\mu$ m

The same area as in (a), but  
after etching for 4 hours with  
the spherical source.

(b)

60  $\mu$ m

Enamel

Amalgam

Cavity amalgam interface on a  
tooth extracted surgically after  
restoration after 3 months.

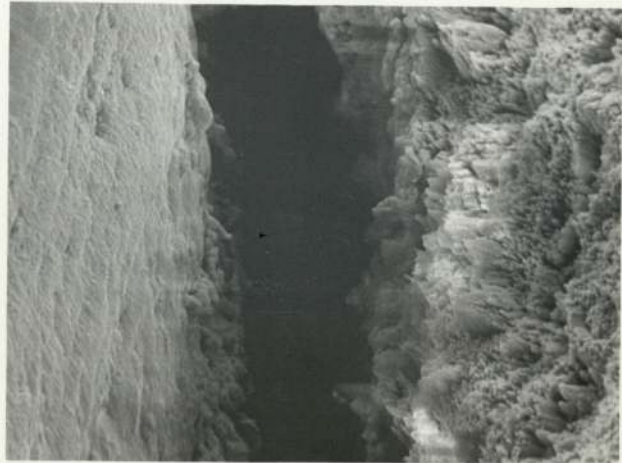
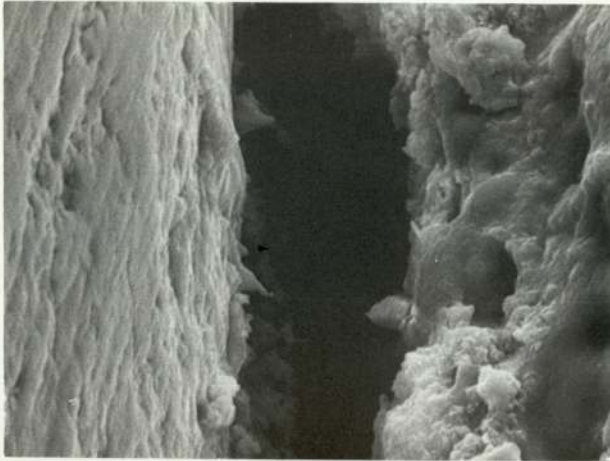
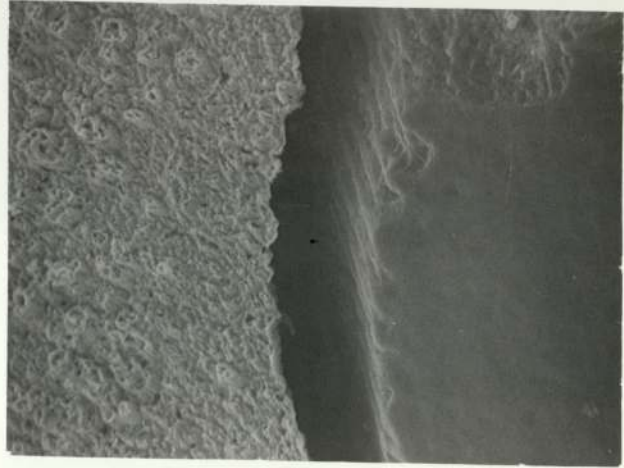
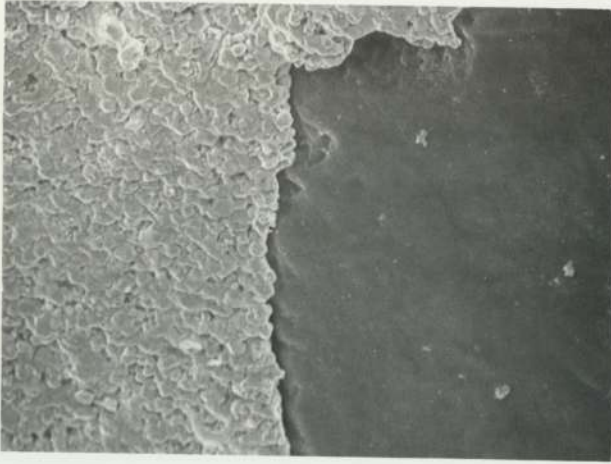
(c)

60  $\mu$ m

Same area as in (c), but after  
etching for 4 hours with the  
spherical source.

(d)

60  $\mu$ m



easily penetrate the gap and reach the pulp, via the dentine. Micrographs (c) and (d) of plate 25 are of a tooth which was restored in the usual way and then extracted surgically after 3 months. Micrograph (c) shows the cavity to be about 55  $\mu\text{m}$  in width, while micrograph (d) shows the same cavity after etching for 4 hours. It can be seen that the etching has not significantly increased the gap.

Further examination of teeth which had been extracted after 6, 9 and 12 months indicated that the gap gradually increased with the time the tooth has been in the oral environment. The above results have shown that the normal technique for dental restorations is not entirely satisfactory and the resulting cavity may in part be responsible for the frequent failures of restorations.

#### 7.5.4 The Reprecipitation of Secondary Calcium Phosphate during Demineralisation

A study by Browne and Rowles (1975) using X-ray microradiography and X-ray diffraction on partially demineralised teeth in 10% formic acid, showed that calcium phosphate was reprecipitated in the lumens of the tubules. In a further study, Rowles and Browne (1975) present many more results and also give a hypothesis as to how this reprecipitation process occurs. However, the resolution of the method employed was not sufficient to demonstrate conclusively that the reprecipitated material occurred within the tubules. The technique of scanning electron microscopy combined with ion etching was used to extend this work to show where the calcium phosphate was reprecipitated.

Sections of incompletely demineralised teeth were taken, 200  $\mu\text{m}$  in thickness and plate 26(a), (4X), shows a microradiograph of one of these. The outer radiolucent area, w, is where it has completely demineralised but "plumes", x, can be seen to be extending into this region. This sample was then fractured in the middle in a near

Micrograph of  
an incompletely  
demineralised  
section of a  
tooth.

2 mm

The sample in (a), fractured and  
then etched for 2 hours with the  
cylindrical source. This  
micrograph taken in the  
circumpulpal dentine, region y of  
(a) and shows empty tubules.

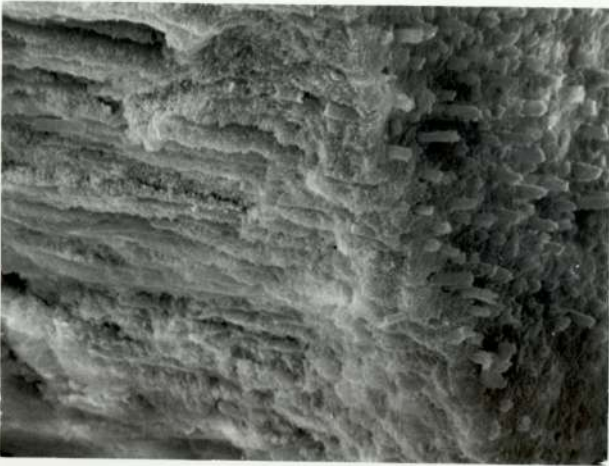
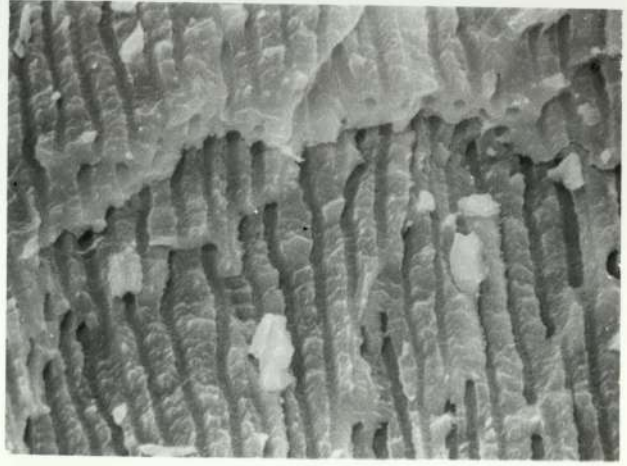
10  $\mu$ m

This is taken in the plume like  
radiopaque area, region x of (a)  
and shows an intratubular deposit of  
brushite.

10  $\mu$ m

This is taken on the pulpal wall,  
region z of (a) and shows crystals  
of hydroxyapatite.

10  $\mu$ m



parallel direction to that of the dentinal tubules and the lower half was examined in the microscope. No clearly defined structure on the specimen was visible. The specimen was etched for 2 hours using the cylindrical source. Micrograph (b), (2000X), shows the circumpulpal dentine - this is the region y of micrograph (a) - in which it is seen that the tubules are free of any type of deposit. Micrograph (c), (2000X), which is taken in the region of the "plume like" radiopacity shows an intratubular deposit of brushite - a crystalline form of calcium phosphate - which was deduced from an X-ray diffraction pattern. This deposit was very resistant to ion etching as was shown by other micrographs in the same region in which the tops of some tubules had been ion etched, exposing the deposit inside. The micrograph (d), (1000X), which was taken on the pulpal wall - region z in micrograph (a) - shows a mass of crystals which were found by X-ray diffraction to be mainly hydroxyapatite, which is another crystalline form of calcium phosphate. The dimensions of these crystals were much greater than those of the dentinal tubules, showing that these were not due to an intratubular deposit. Also the tubules in this region were found to be empty. The ion etching combined with electron microscopy and X-ray diffraction has clearly demonstrated the intratubular location of the reprecipitated calcium phosphate, in the form of brushite crystals.

## CHAPTER 8

### CONCLUSIONS AND SUGGESTIONS FOR FURTHER WORK

The object of this work was to look at the feasibility, practicality and usefulness of saddle field ion sources, for in situ ion etching in a scanning electron microscope of a wide variety of materials. As well as looking at the microstructural aspects of materials, some specific problems were also undertaken in which the ion etching technique was found to be invaluable in providing solutions to these problems.

From a discussion of the requirements of ion sources for this type of study and from a consideration of the main types of sources that are at present available, it has been shown that the saddle field ion sources are particularly suitable. The major advantages of these sources are their simplicity and freedom from a magnetic field or thermionic filament. Furthermore, the source operates at low pressures and therefore relatively low speed pumps are adequate. It is also advantageous that they produce ions with a broad energy spectrum and this ensures that differential etching can be studied on the same specimen. However, perhaps the most attractive feature of the source arises from the fact that the emergent ion beam contains a significant proportion of energetic neutral particles and thus relatively high etching rates can be obtained on insulating surfaces, without the need for charge neutralisation.

The deterioration in performance observed with the cylindrical source in normal operation, has been shown to be due to the uneven deposition of carbon on the hot anodes resulting in a perturbation

of the electric field. However, if necessary, this effect can be eliminated by using water cooled anodes. Experiments on the field disturbance due to the ion exit aperture, have shown that this can be corrected to a large extent by constructing the ion exit aperture in the form of a round chimney.

Comparisons between the sources have been made and it has been shown that under the normal operating conditions, the maximum etching rate for the spherical source is about twice that for the cylindrical source, being typically 10 and 5  $\mu\text{m/hr}$  on bulk copper specimens. It has also been shown that if uniform etching is required over a reasonably large area, then the cylindrical source is more suitable, but if the requirement is for differential etching in a relatively short region, then the spherical source should be used.

Measurement of maximum temperature attained by the specimen during ion bombardment has shown that this is unlikely to be a serious problem for most materials. Furthermore, analysis of bombarded specimens has shown that the possibility of contamination of the specimen by material ejected from the inside of the source should also not be a serious problem.

The in situ ion etching technique that has been developed, has been successfully used to investigate artefacts produced on surfaces during ion bombardment. One such artefact is conical in shape and is known to be produced by inclusions or surface impurities. In one investigation the detailed growth of a cone on an *Fraldite* surface has been followed and in the early stages, the initiating particle has been observed. Cone formation can be avoided by rotating the specimen during etching, but then in many instances this can result in a loss of the desired structural features. It is

suggested that the presence of a few cones is advantageous for providing a permanent record on the micrograph of the direction of the incident ion beam, as this coincides with the axis of the cone. Observations of cone type structures with whisker like growths at the tips, which have not been reported elsewhere, are given. These may be due to thermal degradation of the specimen, or to the presence of extremely hard fibrous inclusions.

The in situ ion etching technique has been shown to give valuable structural information for a study of metals and alloys, such as, copper, sinters and steels. The technique has been shown to be superior to chemical etching, is generally much simpler and also one which can give a greater control of the etching.

Insulating materials, such as plastics, ceramics, glass and Araldite have also been etched. However, indications are given as to where problems may occur and the structure obtained on the surface of Araldite, for example, has been shown to be due to thermal degradation. Furthermore, with plastics, such as acetal, it is concluded that although these can be successfully etched, the resulting topography does not provide very much useful information about its structure. This arises from the fact that there is only a small variation in the sputtering yield of the constituent elements. Microstructures obtained on the surface of glass have been shown to be in agreement with results presented by previous workers, who showed that it was artefactual and a function only of the geometry of the bombardment.

In contradiction to conclusions reached by earlier workers on the etching of soft biological tissues, it has been shown that structural information of extreme value can be obtained for tissues, such as the rat duodenum. It is suggested that this is

undoubtedly due to the selective intake of the heavy fixation elements by different parts of the tissue and thus to provide a large variation in the sputtering yield to reveal features such as cells and nuclei.

The more detailed study of the hard biological materials, (mammalian dental tissues and restorative materials), also showed that the technique is entirely suitable to yield structural information. For instance, the observed prismatic structure of the enamel and the distribution and form of the dentinal tubules has not been demonstrated in such a clear way previously. However, the application to the restorative materials commonly in use was found to be of less value on account of the highly composite nature of these materials. Indeed, micrographs are presented in which the surface of amalgam appears to have fused during etching and this highlights that care must be taken with materials which contain low melting point constituents. Further applications to whole teeth on specific problems, such as the study of the gap between the amalgam cavity interface and the reprecipitation of calcium phosphate during the demineralisation process, have clearly demonstrated the extreme usefulness of ion etching, even when structural information is not the major interest.

The fact that simultaneous etching and viewing was not possible, did not place any undue restrictions on the value of the technique since an image could be obtained within about 30 seconds from switching off the ion source. Simultaneous etching and viewing was attempted but more serious problems than anticipated were encountered. An extremely high signal to the display cathode ray tube was obtained and even when this was reduced to a low level, the image quality was very poor. The reason for this is that the secondary electrons produced by the ion beam from the specimen are also

collected by the scintillator - photomultiplier system. These are sufficient in number to completely overwhelm the true signal from the electron beam. This was overcome to some extent by negatively biasing the secondary electron collector grid at 100 volts, which thus repelled all the secondary electrons produced by both the ion beam and the electron beam and only collected the reflected (or backscattered) high energy electrons. This was found to produce an improvement in the image but the quality was still rather poor. A further problem arose due to the continual deposition of conducting material on the scintillator-photomultiplier, producing a short circuit after only a few hours of etching. This necessitated the dismantling of this unit for a thorough clean out, a process which took many hours.

Clearly simultaneous etching and viewing is possible and should be investigated further. The problems indicated could be overcome, firstly by adequately shielding the vulnerable areas of the scintillator and secondly by pulsing the electron and ion beams. Evidently the microscope display apparatus would have to incorporate pulsing so that this is only on when the ion beam is off. This could probably be fairly easily achieved, but pulsing the ion beam may be a more serious problem and will require further investigation concerning the rate of growth of the discharge in the source.

The limitation at present on the angle of incidence during etching to a minimum of  $27^{\circ}$  does not enable a complete study of etching rates with the angle of incidence to be performed. However this could be overcome by relatively simple changes in the design of the specimen chamber.

From the materials studied in this investigation, Araldite has been shown to be the only one that produces the whisker like cones.

Further work should be undertaken in an attempt to substantiate and explain this phenomenon. The experiments with the rat duodenum and the dental tissues has been very promising and indicate that this should be of considerable value in structural studies of biological materials.

LIST OF FIGURES

	<u>Page</u>
1. Interatomic potential functions evaluated for a copper lattice.	6
2. Illustration of the Auger neutralisation of an ion at a metal surface.	9
3. The variation of        under conditions of kinetic and potential ejection for Ar and K ions on tungsten.	10
4. Variation of sputtering yield with ion energy for polycrystalline copper.	19
5. Variation of sputtering yield with angle of incidence for silica glass.	20
6. Yield-energy curves near the threshold for various metals for argon ion bombardment.	21
7. Geometry of sputtering calculation.	23
8. Diagram for calculating the potential distribution within the oscillator.	34
9. Schematic diagram of the first cylindrical ion source.	36
10. Schematic diagram of the water cooled ion source.	39
11. Illustration of the three different positions of the aperture.	43
12. Graph of $R_n$ and $R_d$ as a function of pressure	45
13. Illustration of the step due to the thickness of the cathode.	47

	<u>Page</u>
14. Stainless steel plug with a 5 mm aperture.	47
15. Illustration of the five different positions of the apertures.	48
16. Graph of $R_n$ against pressure.	49
17. Geometry of the earlier and more recent spherical ion sources.	51
18. Schematic diagram of the new cylindrical ion source.	54
19. Schematic diagram of a Sintox insulator.	55
20. Schematic diagram of the spherical ion source.	56
21. Electrical circuit for the ion sources.	57
22. Variation of tube current, $I_t$ , with tube voltage, $V_t$ , for the cylindrical ion source.	62
23. Variation of ion beam current, $I_b$ , with tube current, $V_t$ , for the cylindrical ion source.	63
24. The three modes of operation for the cylindrical ion source.	64
25. Variation of tube current with tube voltage for the spherical ion source.	65
26. Variation of ion beam current with tube current for the spherical ion source.	66
27. The three modes of operation for the spherical ion source.	67
28. Copper coated specimen studs etched with the cylindrical and spherical sources.	71
29. A plot of the minimum etching rate against distance from the centre of the etched region.	72

	<u>Page</u>
30. Rate of rise of temperature for cerrobend and cerro 117 alloys using the spherical ion source.	76
31. Rate of rise of temperature for cerrobend and cerro 117 alloys with the cylindrical and spherical ion sources respectively.	78
32. Rate of rise of temperature of OFHC copper with both the cylindrical and spherical ion sources.	80
33. Temperature measurements of a tooth using the cylindrical and spherical ion sources.	81
34. ESCA analysis spectrum of an ion bombarded specimen using the spherical ion source.	84
35. ESCA analysis spectrum after removing adsorbed layers.	85
36. Polar diagram of the erosion slowness curve for silica glass and the dissolution trajectories and derived profiles for the sputtering of a silica glass sphere.	93

LIST OF PLATES

<u>Plate Number</u>		<u>Preceding page number</u>
1	Illustrations of the black deposit formed on the anodes.	41
2	Cylindrical source mounted on a flange.	55
3	Spherical source mounted on a flange.	56
4	A view of the V.G. scanning electron microscope.	58
5	Close view of the specimen chamber and goniometer stage.	58
6	Micrographs of the steps produced after etching with the cylindrical and spherical sources.	69
7	The growth of a cone with bombardment time on araldite.	98
8	Cones on copper and dental tissues.	99
9	Cone-like structures on araldite.	100
10	Structure of copper with extension and annealing temperature.	105
11	Structure of a copper-iron sinter.	106
12	Structure of a hard piston steel.	107
13	Structure of a silicon nitride ceramic.	108
14	Structure obtained on soda glass.	109
15	Structure of acrylic plastic.	110

<u>Plate Number</u>		<u>Preceding page number</u>
16	Structure of D.M.C. plastic.	111
17	Structure of acetal plastic.	111
18	Structure of araldite epoxy resin.	112
19	Structure of the rat duodenum.	114
20	Micrographs of whole teeth and tooth sections.	116
21	Structure of dental enamel.	116
22	Structure of dentine.	117
23	Structure of commercial amalgam.	118
24	Structure of spherical amalgam.	119
25	The cavity margin amalgam interface.	120
26	The reprecipitation of secondary calcium phosphate during demineralisation.	121

REFERENCES

- Ambrose, E.J., Batzdorf, U., Osborn, J.S. and Stuart, P.R., (1970),  
Nature, 227, 397.
- Barber, D.J., (1970), J.Mater. Sci., 5, 1.
- Barber, D.J., Frank, F.C., Moss, M., Steeds, J.W. and Tsong, I.S.T.,  
(1973), J. Mater. Sci., 8, 1030.
- Bayly, A.R. and Townsend, P.D., (1972), J.Phys.D, App.Phys., 5, L103.
- Bevelander, G., (1963), Outline of Histology, Fifth Edition,  
St. Louis, The C.V. Mosby Company.
- Bohr, N., (1948), Matt.Fys.Medd., 18, 97.
- Born, M. and Mayer, J.E., (1932), Z.Physik., 75, 96.
- Brandt, W. and Laubert, R., (1967), Nucl.Instr.Meth., 47, 201.
- Brown, F. and Davies, J.A., (1963), Canadian J.Phys., 41, 844.
- Browne, R.M. and Bowles, S.L., (1975), Stain Technology, 50, 179.
- Burger, F. and Maier, J.P., (1975), J.Phys.E, 8, 420.
- Carter, G. and Colligan, J.S., (1968), Ion Bombardment of Solids,  
Heinemann.
- Carter, G. Colligan, J.S. and Nobes, M.J., (1971), J.Mater.Sci,  
6, 115.
- Carter, G., Colligan, J.S. and Nobes, M.J., (1973), J.Mater Sci.,  
8, 1973.

Catana, C., Colligon, J.S. and Carter, G., (1972), J.Mater Sci.

7, 467.

Cleaver, J.S. and Fiveash, P.N., (1970), Vacuum, 20, 49.

Dearnley, G., (1969), Reports on Progress in Physics, 32, 405.

Dhariwal, R.S., Fitch, R.K., Lavelle, C.L.B. and Johnson, G.A.,

Accepted for publication in J. of Anatomy, (1975).

Dhariwal, R.S., Johnson, G.A., Browne, R.M. and Rowles, S.L.,

Submitted to J. of Stain Technology, (1976).

Fetz, H., (1942), Zeits.F.Phys., 119, 590.

Fitch, R.K., Mulvey, T., Thatcher, W.J. and McIlraith, A.H., (1970),

J.Phys.D,App.Phys., 3, 1399.

Fitch, R.K., Mulvey, T., Thatcher, W.J. and McIlraith, A.H., (1971),

J.Phys.E, 4, 553.

Fitch, R.K. and Rushton, G.J., (1972), J.Vac.Sci. and Technol.,

9, 379.

Fitch, R.K., Ghander, A.M., Rushton, G.J. and Singh, R., (1974), Proc.

Sixth Int. Vacuum Congress, Japan J.App.Phys., Supplement 2,

Part 1, 411.

Franks, J., (1972), British Patent Application No. 54627/72

Franks, J., (1973), British Patent Application No. 44718/73.

Franks, J. and Ghander, A.M., (1974), Vacuum, 24, 489.

Frisch, B., Lewis, S.M., Sherman, D., Stuart, P.R. and Osborn, J.S.,

(1974), Scanning Electron Microscopy, Part 3, Proceedings of

the Workshop on Advances in Biomedical Applications in the

SEM, Chicago, Illinois, 655.

- Garcia, J.D. Fortner, R.J. and Kavanagh, T.M., (1973), Reviews of Modern Physics, 45, 111.
- Ghander, A.M., (1974), Ph.D. thesis, Univ. of Aston in Birmingham.
- Ghander, A.M. and Fitch, R.K., (1974), Vacuum, 24, 483.
- Gillam, E., (1959), J.Phys.Chem.Solids, 11, 55.
- Gloersen, P.G., (1975), J.Vac.Sci. and Technol., 12, 28.
- Going, R.E., Massler, M. and Dute, H.L., (1960), J.Dental Research, 39, 273.
- Gombas, P., (1956), Handbook of Physics, 36, 109.
- Goodhew, P.J. and Hepburn, M.J., (1972), Proc.Fifth European Congress on Electron Microscopy, 300.
- Grove, W.R., (1852), Trans.Royal Soc., 142, 87.
- Guntherschulze, V.A. and Tollmein, W., (1942), Zeits.F.Phys., 119, 685.
- Hagstrum, H.D., (1954), Phys.Rev., 96, 336.
- Hagstrum, H.D., (1961), Phys.Rev., 123, 758.
- Hansel, V.H., Casperson, G. and Hoffman, G., (1972), Z.Phys.Chemie, 251, 241.
- Hippel, A.V., (1926, Ann.Physik, 81, 1043.
- Hodges, G.M., Muir, M.D., Sella, C. and Carteaude, A.J.P., (1972), J. Of Microscopy, 95, 445.
- Holland, L. and Laurenson, L., (1964), Vacuum, 14, 325.
- Holland, L. and Priestland, C.R.D., (1972), Vacuum, 22, 133.
- Kaminsky, M., (1965), Atomic and Ionic Impact Phenomena on Metal Surfaces, Springer-Verlag.
- Keywell, F., (1955), Phys.Rev., 97, 1611.

- Khorassany, M., (1976), Private communication, Univ. of Aston in Birmingham.
- Lindhard, J., (1965), *Matt.Fys.Medd.*, 34, 14.
- Mattox, D.M., (1974), *Proc.6th Int.Vac.Congr.*, Japan, *J.App.Phys.*, Suppl.2, Part 1, 443.
- Mayer, J.W., Eriksson, L. and Davies, J.A., (1970), *Ion Implantation in Semiconductors*, Academic Press.
- McCracken, G.M., (1975), *Reports on Progress in Physics*, 38, 241.
- McCutcheon, D.M., (1949), *J.App.Phys.*, 20, 414.
- McIlraith, A.H., (1966), *Nature*, 212, 1422.
- McIlraith, A.H., (1967), Unpublished work.
- Morgan, D.V., (1975), *Contemp.Phys.*, 16, 221.
- Navez, M., Sella, C. and Chaperot, D., (1962), *Int.Symp., Ionic Bombardment, Theory and Applications*, Gordon and Breach, 339.
- Nelson, R.S., (1965), *Phil.Mag.*, 11, 291.
- Nobes, M.J., Colligon, J.S. and Carter, G., (1969), *J.Mater.Sci.*, 4, 730.
- Norgate, P. and Hammond, V.J., (1974), *Phys.in Technol.*, 5, 186.
- Parilis, E.S. and Kishinevskii, L.M., (1960), *Sov.Phys. Solid State*, 3, 885.
- Parilis, E.S., (1968), *Atomic Collision Phenomena in Solids*, North Holland.
- Pearson, A.D. and Harsell, W.B., (1972), *Mater.Res.Bull.*, 7, 567.
- Peggs, G.N. and McIlraith, A.H., (1973), *J.Phys.E*, 6, 1137.

- Penning, F.M. and Moubis, J.H.A., (1940), Koninkl.Ned.Akad.  
Wetenschap. Proc., 43, 41.
- Petrov, N.N., (1962), Bull.Acad.Sci. U.S.S.R. Phys.Ser., 26, 1350.
- Pickard, H.M. and Gayford, J.J., (1965), Brit.Dental J., 119, 69.
- Plucker, M., (1851), Comptes Rendus Des Sciences, 33, 301.
- Rehal, A.S., (1976), Private communication.
- Rosenburg, D. and Wehner, G.K., (1962), J.App.Phys., 33, 1842.
- Rowles, S.L. and Browne, R.M., (1975), Stain Technology, 50, 187.
- Rushton, G.J., O'Shea, K.R. and Fitch, R.K., (1973), J.Phys.D,  
6, 1167.
- Shimizu, R., (1974), Japan. J.App.Phys., 13, 228.
- Sigmund, P., (1969), Phys.Rev., 184, 383.
- Sigmund, P., (1974), App.Phys.Letters, 25, 169.
- Silsbee, R.H., (1957), J.App.Phys., 28, 1246.
- Singh, A.P., (1975), M.Sc. report, Univ. of Aston in Birmingham.
- Southern, A.L., Willis, W.R. and Robinson, M.T. (1963),  
J.App.Phys., 34, 153.
- Spencer, E.G. and Schmidt, P.H., (1972), J.App.Phys., 7, 2956.
- Stewart, A.D.G., (1962), Fifth Int.Congr.Electron Microscopy,  
Philadelphia, paper D12.
- Stewart, A.D.G. and Boyde, A., (1962), Nature, 196, 81.
- Stewart, A.D.G. and Thompson, M.W., (1969), J.Mater.Sci., 4, 56.
- Stuart, P.R., Osborn, J.S. and Lewis, S.M. (1969), Scanning  
Electron Microscopy, Proceedings of the Second Annual SEM  
Symp., I.T.T. Research Institute, Chicago, Illinois.

Swaminathan, S. and Venkatasubramanian, V.S., (1974), Private communication.

Timoschenko, G., (1941), J.App.Phys., 12, 69.

Thatcher, W.J., (1970), Ph.D. thesis, Univ.of Aston in Birmingham.

Thompson, M.W. and Nelson, R.S., (1962), Phil.Mag., 7, 2015.

Thompson, M.W., (1968), Phil.Mag., 18, 377.

Thompson, M.W., (1969), Defects and Radiation Damage in Metals, Cambridge Univ.Press.

Tsong, I.S.T. and Barber, D.J., (1972), J.Mater.Sci., 7, 687.

Tsong, I.S.T. and Barber, D.J., (1973), J.Mater.Sci., 8, 123.

Walters, D.L. and Bhalla, C.P., (1971), Phys.Rev.A, 4, 2164.

Warner, S.B., Uhlmann, D.R. and Peebles, L.H., (1975), J.Mater.Sci., 10, 758.

Wehner, G.K., (1955), Advances in Electronics and Electron Phys., 7, 239.

Wehner, G.K., (1955), J.App.Phys., 26, 1056.

Wehner, G.K., (1956), Phys.Rev., 102, 690.

Wehner, G.K., (1957), Phys.Rev., 108, 35.

Wehner, G.K., (1958), Phys.Rev., 112, 1120.

Wehner, G.K., (1959), J.App.Phys., 30, 1762.

Wehner, G.K. and Hajicek, D.J., (1971), J.App.Phys., 42, 1145.

Werner, H.W., (1974), Vacuum, 24, 493.

Wilson, I.H. and Kidd, M.W., (1971), J.Mater.Sci, 6, 1362.

Wilson, I.H., (1973), Radiation Effects, 18, 95.

Witcomb, M.J., (1974), J.Mater.Sci., 2, 551.

Witcomb, M.J., (1974), J.Mater.Sci., 2, 1227.

Yasuda, H., (1974), J.App.Phys., 45, 484.